UNIVERSITY OF CALIFORNIA,
IRVINE

Nonlinear Magnetic Damping and Parametric Excitation of Magnetization in Nanomagnets

DISSERTATION

submitted in partial satisfaction of the requirements
for the degree of

DOCTOR OF PHILOSOPHY

in Physics

by

Han Kyu Lee

Dissertation Committee:
Professor Ilya N. Krivorotov, Chair
Professor Wilson Ho
Professor Ruqian Wu

2017

TABLE OF CONTENTS

LIST OF FIGURES

ACKNOWLEDGMENTS

I would like to express my gratitude to my research advisor, Professor Ilya Krivorotov. I learned to appreciate physics research through his intuitions, breadth of knowledge, and his generous supports. I want to equally thank Dr. Igor Barsukov for showing me how to do experiments, sharing his perspectives, and teaching everything that I know about ferromagnetic resonance. I would like to thank Yu-Jin Chen, my coworker, and a patient teacher. He spent many hours me with clarifying my confusions, discussing projects, physics, and shared his knowledge on microwave measurements and programming. It has been a great privilege to research with both Igor and Yu-Jin and the work in dissertation would have been impossible without their supports.

It is my fortune to join the Krivorotov group surrounded by supportive colleagues: Brian Youngblood, Liu Yang, Andrew Smith, Jieyi Zhang, Chris Safranski, Alejandro Jara, Jenru Chen, Chengcen Sha, Tobias Schneider, Dr. Eric Montoya, and Amanatullah Khan. I would like to also thank our theory collaborators including Professor Roman Verba, Professor Vasil Tiberkevich, Professor Andrei N. Slavin, Professor Boris A. Ivanov, Professor Rodrigo E. Arias. I am very grateful to Dr. Adrian G. Swartz, Dr. Bongju Kim, and Professor Harold Y. Hwang for providing high-quality LSMO thin films. I would like to thank Dr. Jordan Katine, Dr. Patrick Braganca, Dr. Hsin-wei Tseng, and Dr. Andrei Garcia, for their kind encouragements during my summer internship.

I am also grateful to Professor Wilson Ho and Professor Ruqian Wu for serving the dissertation committee. I want to thank talented Wilson Ho group members especially to Chi-lun Jiang, Dr. Haigang Zhang, Shaowei Li, Calvin Patel, Greg Czap, Freddy Toledo, Weicai Cao, Dr. Hikari Kimura, and Dr. Ungdon Ham, for their humor and teaching me designing, machining, and building mechanical components.

Finally, I want to express my deepest gratitude to my parents Hyung Hwan and Myung Soon for all their unconditional supports, and to my wife Gyo Sun for her everlasting encouragements and cheerfulness.

I acknowledge AIP Publishing for allowing the use of "Magnetic anisotropy, damping, and interfacial spin transport in Pt/LSMO bilayers" for Chapter 3 of this dissertation.
I acknowledge ACS Publications for allowing the use of "Parametric resonance of magnetization excited by electric field" for Chapter 5 of this dissertation.

CURRICULUM VITAE

Han Kyu Lee

EDUCATION

Doctor of Philosophy in Chemical and Materials Physics **2017**
University of California, Irvine *Irvine, CA*

Master of Science in Chemical and Materials Physics **2017**
University of California, Irvine *Irvine, CA*

Bachelor of Science in Physics **2005**
University of California, Los Angeles *Los Angeles, CA*

RESEARCH AND TEACHING EXPERIENCE

Graduate Research Assistant **2010–2017**
University of California, Irvine *Irvine, CA*

Graduate Teaching Assistant **2009–2012**
University of California, Irvine *Irvine, CA*

REFEREED JOURNAL PUBLICATIONS

Parametric resonance of magnetization excited by electric field
Yu-Jin Chen*, *Han Kyu Lee**, Roman Verba*, Jordan A. Katine, Igor Barsukov, Vasil Tiberkevich, John Q. Xiao, Andrei N. Slavin, and Ilya N. Krivorotov
Nano Lett., 17(1), 572-577 (2017)
∗ Equal contribution authors

Spin caloritronic nano-oscillator
Chris Safranski*, Igor Barsukov*, *Han Kyu Lee*, Tobias Schneider, Alejandro Jara, Andrew Smith, Houchen Chang, Kilian Lenz, Juergen Lindner, Yaroslav Tserkovnyak, Mingzhong Wu, and Ilya N. Krivorotov
Nat Commun. 8, 117 (2017)

Magnetic anisotropy, damping, and interfacial spin transport in Pt/LSMO bilayers
Han Kyu Lee, Igor Barsukov, Adrian G. Swartz, Bongju Kim, Liu Yang, Harold Y. Hwang, and Ilya N. Krivorotov
AIP Advances, 6, 055212 (2016)

PRESENTATIONS AND CONFERENCES

Magnetization dynamics in LSMO/Pt nanowires in the presence of spin orbit torques — **Mar. 2016**
APS March Meeting, Baltimore, MD, USA, Oral presentation

Magnetization dynamics in LSMO/Pt nanowires in the presence of spin Hall torques — **Jan. 2016**
MMM-Intermag, San Diego, CA, USA, Oral presentation

Magnetic anisotropy and anisotropic damping in LSMO/STO(001) — **Mar. 2015**
APS March Meeting, San Antonio, TX, USA, Oral presentation

Magnetic anisotropy and anisotropic damping in LSMO/STO thin films — **Nov. 2014**
MMM, Honolulu, HI, USA, Poster presentation

INVITED TALKS

Magnetization dynamics in LSMO/Pt nanowires in the presence of spin orbit torques — **Mar. 2016**
APS March Meeting, Baltimore, MD, USA, a joint AKPA-KPS session

AWARDS

GMAG Student Travel Award, APS March Meeting, Baltimore, MD — 2016
UCI Regents Fellowship, University of California, Irvine (UCI) — 2009

PROFESSIONAL MEMBERSHIPS

American Physical Society (APS)

ABSTRACT OF THE DISSERTATION

Nonlinear Magnetic Damping and Parametric Excitation of Magnetization in Nanomagnets

By

Han Kyu Lee

Doctor of Philosophy in Physics

University of California, Irvine, 2017

Professor Ilya N. Krivorotov, Chair

This dissertation explores the study of magnetization dynamics in a ferromagnetic thin film and nanoscale ferromagnets. In bulk ferromagnets, nonlinear interactions generally couple each spin wave eigenmode to a continuum of other available modes through multi-magnon scattering. The multi-magnon scattering can potentially limit an achievable amplitude of spin wave modes by pumping energy into other energy-degenerate modes. For example, two-magnon scattering process in the presence of impurities and defects is known to act as a channel of magnetic damping in ferromagnetic thin films. I present an observation of the two-magnon scattering in epitaxial $La_{0.7}Sr_{0.3}MnO_3$ (LSMO) and LSMO/Pt thin films, investigate its impact on the evaluation of low magnetic damping in LSMO, and properties of spin transport through the LSMO/Pt interface for potential nanodevice applications.

Magnetic damping is a critical parameter that determines the speed and energy efficiency of the magnetic nanodevice such as spin-torque memory and oscillators. In a nanomagnet, the geometric confinement breaks translational invariance of the system and discretizes the spin wave spectrum, which helps to suppress the kinematically allowed multi-magnon scattering. The suppression of multi-magnon scattering enables an unusual type of nonlinear interactions and excitation processes in nanoscale ferromagnets that are qualitatively different from that in bulk ferromagnets. In this regard, I report an observation of nonlinear resonant three-

magnon scattering and its effect in the damping of nanoscale magnetic tunneling junctions (MTJs). The spectral lineshape of a spin wave resonance undergoing three-magnon scattering exhibits a minimum at the resonance frequency in sharp contrast to the amplitude maximum seen in the linear resonance regime. This unusual behavior arises because the damping parameter of a spin wave ceases to be frequency-independent and itself becomes a resonant function of the excitation frequency. Also, such resonant nonlinear damping dramatically alters the response of a nanomagnet to antidamping spin-torque in a counterintuitive way - the antidamping torque can increase the damping of a spin wave mode that undergoes the nonlinear resonant scattering.

Lastly, I present an experimental demonstration of electric-field driven parametric excitation of a spin wave eigenmode in nanoscale MTJ. This work shows that the microwave electric field applied across the MTJ electrode efficiently couples to the out-of-plane component of oscillating magnetization via voltage-controlled magnetic anisotropy (VCMA) in the system. The threshold voltage of parametric excitation is found to be well below 1 Volt, which makes it attractive for magnonic nanodevices such as spin wave logic. The electric-field driven parametric excitation of magnetization is a versatile method for generating short-wavelength spin wave and thus results in this work pave the way towards energy-efficient excitation of magnetization dynamics in thin films of metallic ferromagnets and nanodevices based on magnetic multilayers.

Chapter 1

Introduction and Background Material

Magnetic systems studied in this dissertation are a thin film of single layer ferromagnet, a thin film of bilayer ferromagnet/nonmagnetic metal, and nanoscale magnetic tunnel junctions (MTJs) that consist of ferromagnet/insulator/ferromagnet trilayer at its core structure. In the trilayer structure of MTJs, one of the ferromagnetic layer called free layer is sufficiently decoupled from rest of magnetic multilayer that it can be considered as an isolated magnetic volume. Therefore, all aforementioned magnetic systems can be understood by physics describing properties of a single magnetic volume. In the rest of this Chapter, I describe background materials starting with a short introduction about MTJs followed by magnetization, magnetic anisotropy and magnetization dynamics in an isolated ferromagnet. Next, I discuss the magnetic dynamics in the presence of spin-transfer torque and outline contributions in magnetic damping that are relevant to the work in this dissertation.

In Chapter 2, I describe experimental methods employed in this dissertation. First, I introduce ferromagnetic resonance (FMR) spectrometer setup based on coplanar waveguide

(CPW) for characterizing magnetic thin films. I then discuss variants of CPW-FMR setup for performing angular dependent FMR measurements and inverse spin Hall effect measurements. Next, I introduce spin-torque FMR (ST-FMR) technique, which I employed for characterizing MTJs. I describe an experimental setup for ultrahigh sensitive field-modulated ST-FMR that allowed measurements of magnetic damping in a highly symmetric magnetic configuration in MTJs.

In Chapter 3, I introduce a brief background about $La_{0.7}Sr_{0.3}MnO_3$ (LSMO) followed by a presentation of experimental results from FMR measurements on a single layer LSMO thin film and Pt/LSMO bilayer. First, I discuss an observation of large negative perpendicular magnetic anisotropy and a weaker uniaxial in-plane anisotropy in the system. Magnetic damping shows the low Gilbert damping and significant contribution of two-magnon scattering in this system. I present an enhancement of the damping due to spin pumping in the Pt/LSMO bilayer and detection of inverse spin Hall effect.

In Chapter 4, I present an observation of nonlinear magnetic damping due to resonant three-magnon scattering in MTJs. First, I present ST-FMR measurements of a spin wave mode resonance that exhibit a minimum at the resonance frequency instead of the maximum observed in the linear regime. Next, I show substantial damping enhancement of the spin wave mode, in which undergoing resonant three-magnon scattering, under the presence of anti-damping spin torque. I present a theory developed by theoretician colleagues that explain these counterintuitive phenomena.

In Chapter 5, I present an experimental demonstration that shows parametric excitation of magnetization dynamics in a nanomagnet driven by microwave electric field. I discuss results that show resonance character of parametric excitation and a threshold of parametric resonance on the drive voltage, which is compared to a theory predicting this phenomenon.

1.1 Magnetic Tunnel Junctions (MTJs) and Tunneling Magnetoresistance

The nanomagnets that appear in this dissertation are a ferromagnetic layer of nanoscale magnetic tunnel junctions (MTJs). An MTJ consists of two layers of metallic ferromagnets (FM), such as cobalt-iron alloys, separated by an ultrathin layer of an insulator as shown in Fig. 1.1(a). The thickness of FMR layers is typically in the range of a few nanometers down to less than one nanometer. The insulating layer is typically MgO or aluminum oxide, and it serves as a tunnel barrier for electron transport and decreases interlayer coupling between two FM layers. One of FM layer called free layer has its magnetization sufficiently decoupled from the rest of magnetic layers, and external magnetic field can manipulate the free layer magnetization. The magnetization of the other FM layer is made to be fixed or hard manipulate by the external magnetic field. This layer is called a reference (ref) layer, but it is also known as a polarizing layer or pinned (fixed) layer. One simple way to pin the magnetization is to increase the layer thickness because, then, it will require more magnetic energy to manipulate. A more effective method for strongly pinning the magnetization is to deposit an antiferromagnet adjacent to the FM layer. The exchange bias at the interface between the antiferromagnet and the FM layer results strongly pin the magnetization of the FM layer [1].

The MTJ devices are typically patterned into a nanopillar structure with various cross sectional shapes, e.g., circle, ellipses, etc., having lateral dimensions in the range 300 nm or smaller. The MTJ devices studied in this dissertation have an elliptical cross section, as shown in Fig. 1.2. The elliptical shape gives rise to an in-plane magnetic anisotropy (uniaxial anisotropy) in the plane of the layer because magnetization directed along the short axis vs long axis of ellipse experiences different demagnetizing field (shape anisotropy), see Fig. 1.2, and Section 1.2. As a result, the magnetization favors (unfavors) to align along the

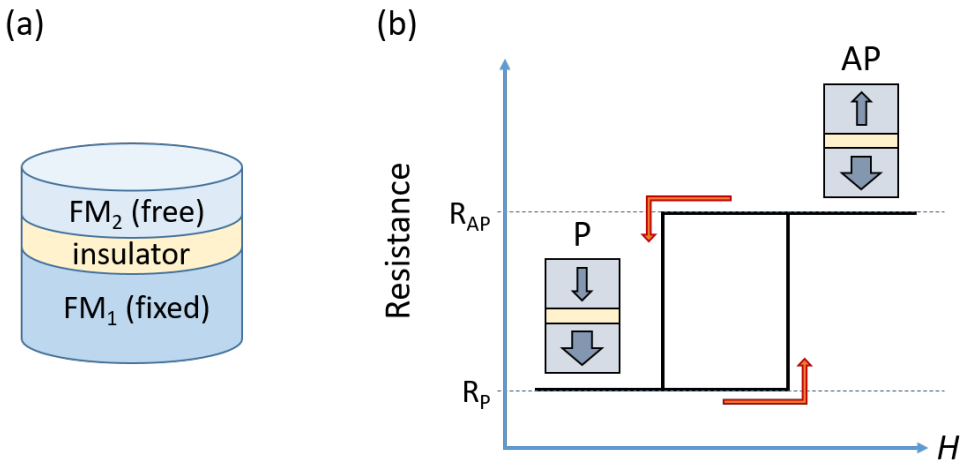

Figure 1.1: **Magnetic tunnel junction (MTJ).** (a) Schematic of an MTJ nanopillar that consists of two ferromagnets separated by an ultrathin insulator acting the tunnel barrier. (b) A sketch of a perpendicularly magnetized MTJ's resistance vs external magnetic field H hysteresis loop. Tunneling magnetoresistance (TMR) results in the higher resistance in the anti-parallel state (AP) than the resistance of the MTJ in the parallel state (P) of two magnetizations. A thicker (narrow) arrow represents the magnetization of reference (free) layer, respectively. The red arrow represents the sweep direction of the magnetic field. The magnetic anisotropy, e.g., uniaxial anisotropy, of free layer determines the width of the hysteresis loop - rectangular loop formed by different switching field for a given field sweep direction.

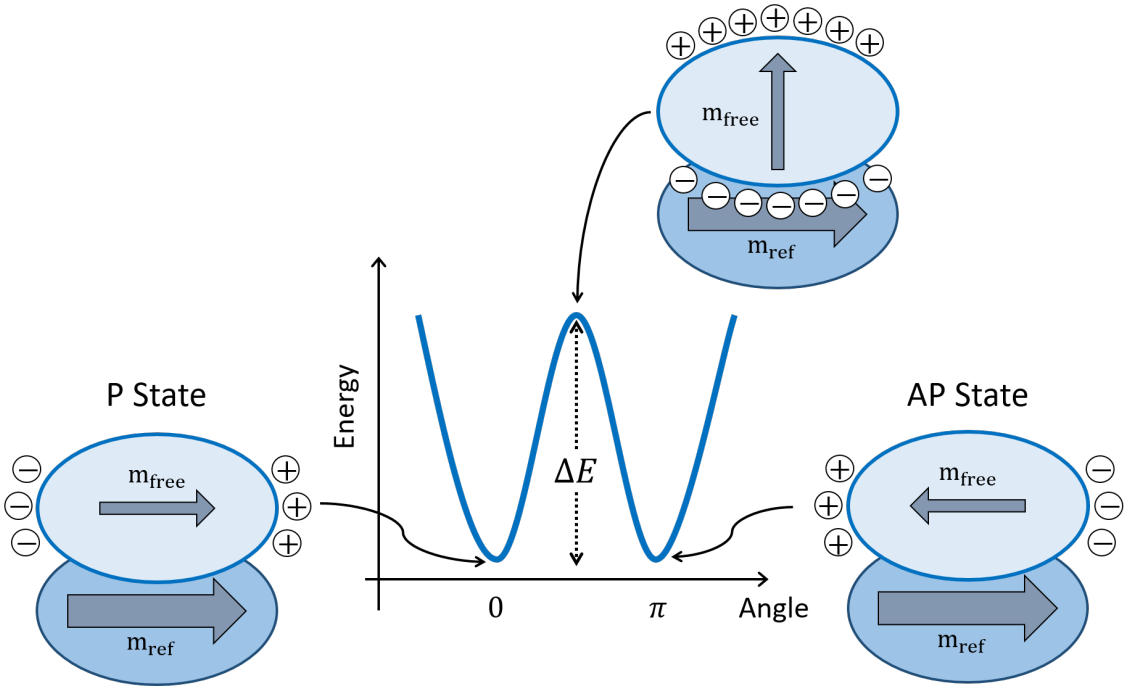

Figure 1.2: **Uniaxial magnetic anisotropy (uniaxial anisotropy) in MTJ due to shape anisotropy.** The shape of magnetic volume gives rise demagnetizing field that depends on the magnetization direction, which is called shape anisotropy, see section. 1.2. An MTJ patterned into elliptical shape exhibit shape anisotropy within the plane of layers: the magnetization favors (unfavors) to align along the long (short) axis of the ellipse. This character is modeled by the uniaxial anisotropy of having an easy (hard) axis of the uniaxial symmetry along the long (short) axis of the ellipse, respectively. For in-plane magnetized MTJ with elliptical shape, the parallel and antiparallel states of the free and fixed layers typically set along the easy axis of the uniaxial anisotropy (long axis of ellipse), and the energy barrier ΔE between P and AP state comes from strength of the uniaxial anisotropy in the free layer.

long (short) axis of the ellipse which makes this direction an easy (hard) axis of the uniaxial anisotropy, respectively. The energy barrier between easy axis and the hard axis come from the strength of uniaxial anisotropy. In our in-plane magnetized MTJ devices, the parallel and anti-parallel alignments of the free and reference layers are set along the easy axis of the uniaxial anisotropy (along with the long axis of the ellipse). For MTJs where all layers are perpendicularly magnetized (pMTJs), the dominant uniaxial anisotropy comes from perpendicular magnetic anisotropy (PMA) that has symmetric axis along the out-of-plane direction, see Section 1.2.

Tunneling magnetoresistance (TMR) is quite important property of MTJ because this effect allows reading the relative state between free and reference layer magnetizations by measuring electrical resistance of the MTJ. TMR ratio describes the difference in the resistance between high resistance anti-parallel (R_{AP}) and low resistance parallel (R_{P}) orientations between the two magnetizations, see Fig. 1.1(b).

$$\mathrm{TMR} = \frac{R_{\mathrm{AP}} - R_{\mathrm{P}}}{R_{\mathrm{P}}} = \frac{R_{\mathrm{AP}}}{R_{\mathrm{P}}} - 1, \tag{1.1}$$

The conductance $G(\theta)$ of an MTJ as function of the relative angle θ between two magnetizations is modeled as [2]

$$G(\theta) = \frac{G_{\mathrm{AP}} + G_{\mathrm{P}}}{2} \left(1 + P_1 P_2 \cos\theta\right), \tag{1.2}$$

where P_1 and P_2 are the spin polarizations of each FM layers. $G_{\mathrm{AP}} = R_{\mathrm{AP}}^{-1}$ and $G_{\mathrm{P}} = R_{\mathrm{P}}^{-1}$ are the conductance of the MTJ for AP and P state, respectively. When the magnetization of a layer in MTJ precess, e.g. the free layer that is resonantly excited, $\theta = \theta(t)$ oscillates in time. This results in time-dependent resistance of the MTJ having components at the precession frequency f_0 and its higher harmonic components [3]:

$$R_{\mathrm{MTJ}}(t) = \Delta R_0 + \Delta R(t) = \Delta R_0 + \mathrm{Re}\left(\sum_n \Delta R_{n\,f_0}\, e^{i\,n\,(2\pi f_0)\,t}\right), \tag{1.3}$$

where ΔR_{nf_0} can be complex with phase δ_{nf_0}. This AC resistance oscillation $R_{\mathrm{MTJ}}(t)$ is utilized for electrical detection of the magnetization excitations in MTJ via spin-torque ferromagnetic resonance technique, which is outlined in Section 2.2.

1.2 An Overview of Magnetic Anisotropy

At a temperature below the Curie temperature T_{C}, ferromagnetic materials exhibit spontaneous ordering that all its magnetic moments $\vec{\mu}$ align in the same direction by the exchange interaction [1, 4]. These moments arises from spin and orbital angular momentum of electrons and the total magnetic moments over the volume V is called magnetization $\vec{M} = \left(\sum \vec{\mu}_i\right)/V$ of a sample [1, 4]. The orientation of magnetization $\vec{M}$ within a sample has directional dependence called magnetic anisotropy and described by magnetic anisotropy energy (MAE). The magnetization tends to align in the direction, called easy axis, that minimizes the energy and hinders to align in the direction, called hard axis, which maximizes the energy. Among several contributions of magnetic anisotropy, Zeeman energy, magnetocrystalline anisotropy, and uniaxial magnetic anisotropy are the most important contributions in this dissertation. I omit discussions of magnetoelastic (induced by stress) and exchange anisotropy (induced from a neighboring antiferromagnet) that have no contributions to this work.

The spherical coordinate system is used throughout the dissertation. The azimuthal angles ϕ and polar angles θ for magnetization are referenced to the [100] direction in the plane of the magnetic thin film and the [001] direction, out-of-plane of the film, respectively. When the magnitude of external magnetic field H (or sometimes denoted as H_{ext}) is above saturation field H_{sat} ($H > H_{\mathrm{sat}}$, or called a saturated regime), the equilibrium direction of the magnetization is aligned parallel to the external field direction. Throughout the dissertation, the saturated regime is assumed, and the polar and azimuthal angles are used to represent both the magnetization and the external magnetic field interchangeably otherwise noted.

Zeeman Energy

Zeeman energy is a potential energy density of magnetization under the external magnetic field $\vec{H}$ and the energy minimum occurs when the magnetization is parallel to the external

field.

$$F_{\text{Zeeman}} = -\vec{M} \cdot \vec{H} \tag{1.4}$$

Magnetocrystalline Anisotropy

Magnetocrystalline anisotropy (MCA) arises from spin-orbit interaction that couples the magnetic moment of the electron with the crystal lattice [1, 4, 5]. As a consequence the magnetization prefers to align along well-defined crystallographic axes. In practice, the free energy density of magnetocrystalline anisotropy F_{mc} is phenomenologically derived based on power series expansion of direction cosines α_i of the magnetization $\vec{M} = M_s(\alpha_x, \alpha_y, \alpha_z)$ with respect to the crystallographic axes [1, 4, 5]. M_s is the saturation magnetization. The crystal system detemines the nonzero terms in the expansion and only even powers of the cosines are allowed when symmetry requires that $F_{\text{mc}}(\alpha_i) = F_{\text{mc}}(-\alpha_i)$, i.e. if 180° rotation is identical in the α_i direction.

In a cubic crystal, the lowest order term in the energy density is [5]:

$$\begin{aligned} F_{\text{mc}} &= K_{mc}\left(\alpha_x^2\alpha_y^2 + \alpha_y^2\alpha_z^2 + \alpha_z^2\alpha_x^2\right) \\ &= K_{\text{mc}}\sin^2\theta - \frac{1}{8}K_{\text{mc}}\left(7 + \cos 4\phi\right)\sin^4\theta \\ &= \frac{1}{2}M_{\text{s}}\left(\frac{2K_{\text{mc}}}{M_{\text{s}}}\right)\sin^2\theta - \frac{1}{16}M_{\text{s}}\left(\frac{2K_{\text{mc}}}{M_{\text{s}}}\right)\left(7 + \cos\ 4\phi\right)\sin^4\theta \\ &= \frac{1}{2}M_{\text{s}}H_{\text{mc}}\sin^2\theta - \frac{1}{16}M_{\text{s}}H_{\text{mc}}(7 + \cos\ 4\phi)\sin^4\theta, \end{aligned} \tag{1.5}$$

where K_{mc} is first order anisotropy constant which has *four-fold* symmetry. The corresponding anisotropy field is $H_{\text{mc}} = 2K_{\text{mc}}/M_{\text{s}}$, which is a useful quantity for comparing the strength of magnetic anisotropies in the system. A positive $K_{\text{mc}} > 0$ results easy axes and hard axes along the $\langle 100\rangle$ and $\langle 111\rangle$ directions, respectively. The projection of hard axes $\langle 111\rangle$ on to

the plane of the film results $\langle 110 \rangle$ as hard axes within the plane. A contribution from second order anisotropy could be considered but not shown here.

Lastly, the first term in the last line of Eqn. (1.5) can be expanded as $\frac{1}{2}M_s H_{\rm mc} - \frac{1}{2}M_s H_{\rm mc}\cos^2\theta$ but the first term of the expanded expression can be neglected because $\frac{1}{2}M_s H_{\rm mc}$ has no angular dependence. The final expression of the energy density is

$$F_{\rm mc} = -\frac{1}{2}M_{\rm s}H_{\rm mc}\cos^2\theta - \frac{1}{16}M_{\rm s}H_{\rm mc}(7+\cos\,4\phi)\sin^4\theta, \tag{1.6}$$

Shape Anisotropy: Demagnetization Field

A finite volume of magnetic material produces magnetic charges at the surface as a solution to the boundary problem in magnetostatics [1]. The magnetic surface charges or surface poles is a source of a physically observable magnetic field called demagnetizing field $H_{\rm demag}$. The demagnetizing field, as the name suggests, acts in opposition to the magnetization $\vec{M}$ at inside the volume and continues as a dipolar stray field at the outside. The demagnetizing field depends upon the shape of the volume because the surface poles distribution varies as the magnetization orientation changes and give rise to the shape anisotropy.

In general, calculation of demagnetizing field is quite challenging and often requires numerical computation except for few highly symmetric geometries, e.g., uniformly magnetized sphere and ellipsoids [4, 6]. In thin films, edges of the plane can be approximated as semi-infinitely separated and corresponding surface poles can be assumed to be vanishingly small. The surface charges occur only in the direction normal to the film plane, and the shape anisotropy is described by [1, 4, 5]

$$F_{\rm shape} = \frac{1}{2}\,4\pi M_s^2\cos^2\theta, \tag{1.7}$$

where M_s is the saturation magnetization, and θ is the polar angle. The shape anisotropy always favors the magnetization to lie within the plane of the film, i.e., the energy minimum occurs at $\theta = 90°$.

Perpendicular Magnetic Anisotropy

As thickness of thin films becomes smaller, the role of surface becomes significant and the preferential direction of the magnetization can change from the commonly observed in-plane orientation (due to shape anisotropy) to the out-of-plane direction. This originates from considerably different magnetic anisotropy at the surface or interface compared to the bulk of the film due to having lowered symmetry and surface oxidation at the surface/interface [1, 7]. The free energy density of perpendicular magnetic anisotropy (PMA) $F_\perp$ is described by [1, 5, 7],

$$\begin{aligned} F_\perp &= -\frac{2K_\mathrm{s}}{t_\mathrm{film}}\cos^2\theta \\ &= -K_\perp \cos^2\theta \\ &= -\frac{1}{2}M_s\left(\frac{2K_\perp}{M_s}\right)\cos^2\theta, \end{aligned} \tag{1.8}$$

where $K_\perp$ is the PMA constant which has *two-fold* symmetry with respect to out-of-plane direction. The $K_\perp$ can be both positive or negative depending on the thickness of the film t_film. For $K_\perp > 0$, the easy-axis is along the out-of-plane direction, $\theta = 0°$. In the literature, e.g. Ref. [7], the PMA constant is denoted by K_s with a prefactor 2 to account contribution from both surfaces, e.g. top and bottom of the film. The accurate determination of K_s requires thickness dependent measurements, which I did not performed in this work and I lumped it as $K_\perp = 2K_\mathrm{s}/t_\mathrm{film}$.

Lastly, the anisotropic constants K_i or anisotropic fields H_i are often grouped together by the symmetry of the magnetic anisotropy. For example, the shape anisotropy and PMA

have *two-fold* symmetry with respect to the out-of-plane direction. These contributions are often reported in the literature as the effective out-of-plane magnetic anisotropy with the corresponding anisotropy field $H_{\perp,\text{eff}}$,

$$H_{\perp,\text{eff}} = 4\pi M_\text{s} - 2K_\perp/M_\text{s} \tag{1.9}$$

Uniaxial Magnetic Anisotropy

Additional uniaxial anisotropy could be presented within the plane of the sample. It could arise from dipole interaction between small areas ($\sim$10 nm) of the sample and local variations of the magnetic parameters that a global magnetic anisotropy can be resulted [8]. The free energy density of the uniaxial anisotropy can be described by [5]

$$F_\text{uni} = -\frac{1}{2} M_\text{s} H_\text{uni} \cos^2(\phi - \phi_\text{uni}) \, \sin^2\theta, \tag{1.10}$$

where ϕ_uni is the angle between the easy axis of UMA with respect to the [100] crystallographic axis for the positive $H_\text{uni} > 0$.

1.3 Voltage-Controlled Magnetic Anisotropy

Recently, the magneto-electric (ME) effect at the interface between a ferromagnetic metal (e.g. Fe) and a non-magnetic insulator (e.g. MgO) is discovered [9, 10, 11, 12]. This interfacial ME effect called voltage-controlled magnetic anisotropy (VCMA). VCMA originates from different rates of filling surface states, *d*-like electron bands at the Fe/MgO interface, in response to an electric field applied at the out-of-plane direction. Electrons in different bands contribute differently to the uniaxial perpendicular magnetic anisotropy (PMA) at the Fe/MgO interface. Therefore, inducing electron accumulation or depletion at the interface

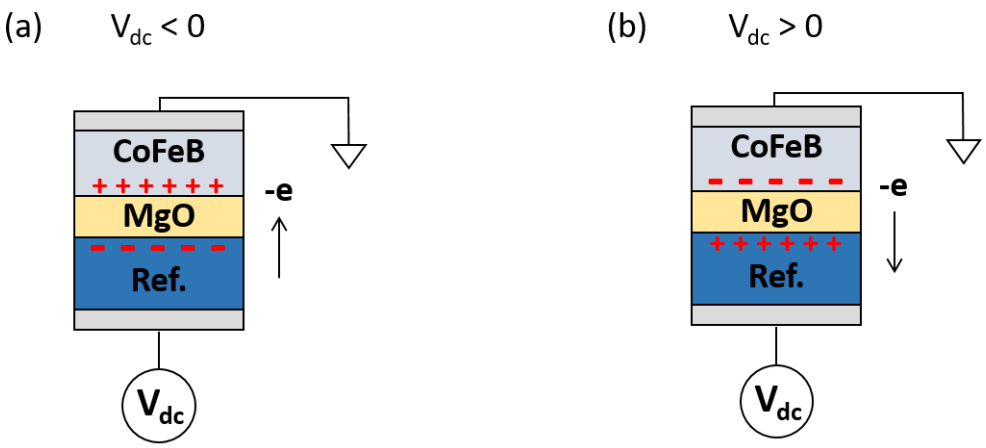

Figure 1.3: **Voltage-Controlled Magnetic Anisotropy (VCMA) at MgO/CoFeB interface.** In the schematics, the CoFeB layer is electrically grounded, and the voltage source is applied to the reference (ref) layer of an MTJ. The capping metal is assumed as Ta. (a) At negative bias ($V_{dc} < 0$) applied to an MTJ, electrons deplete at the interface between MgO and the CoFeB layer. This increases the perpendicular magnetic anisotropy (PMA) of the CoFeB layer. The electron depletion (accumulation) leaves net positive (negative) charge at the MgO/Fe interface and depicted as the red + (-) symbol, respectively. The electrons are represented as "-e" (b) At positive bias ($V_{dc} > 0$), electrons accumulate at the interface between MgO and the CoFeB layer and reduces the PMA of the CoFeB layer.

modulates the PMA via applying voltage between MgO/Fe layers [11, 12].

VCMA can be characterized by VCMA efficiency ($dH_{\perp}/dV$), a net change of PMA in response to the applied voltage across the interface. It is known that the sign of ζ_{VCMA} depends on the materials combination of insulator, ferromagnetic and non-magnetic capping layer. For example, MgO/CoFeB/Ta and MgO/CoFeB/Ru have the opposite VCMA sign, see Ref. [13] and references therein. Concerning the sign of VCMA efficiency, the direction of electron flow with respect to the interface between the ferromagnetic layer and MgO is essential - whether electron accumulates or depletes at the interface. For MgO/CoFeB/Ta system, the electron depletion at the MgO/CoFeB interface increases the PMA [13], see Fig. 1.3.

1.4 Magnetization Dynamics

The magnetic anisotropy discussed in previous sections determines the equilibrium direction of magnetization. At the equilibrium state, the magnetization aligns to a time-independent effective field $\boldsymbol{H}_{\text{eff}}$ that consists of the applied external magnetic field $\boldsymbol{H}_{\text{ext}}$ plus any existing internal magnetic fields such as shape anisotropy (demagnetization) field $\boldsymbol{H}_{\text{demag}}$, PMA field $\boldsymbol{H}_{\perp}$, magnetocrystalline anisotropy field $\boldsymbol{H}_{\text{mc}}$, uniaxial anisotropy field $\boldsymbol{H}_{\text{uni}}$. When the magnetization is driven out of its equilibrium, e.g. via ferromagnetic resonance, the magnetization starts to process around $\boldsymbol{H}_{\text{eff}}$ and its motion is described by Landau-Lifshitz-Gilbert (LLG) equation [5, 14]:

$$\frac{d\mathbf{m}}{dt} = -\gamma\, \mathbf{m} \times \boldsymbol{H}_{\text{eff}} + \alpha\, \mathbf{m} \times \frac{d\mathbf{m}}{dt}, \tag{1.11}$$

where unit vector of magnetization $\mathbf{m} = \frac{\vec{M}}{M_{\text{s}}}$, $\gamma = |g\mu_{\text{B}}/\hbar|$ is the gyromagnetic ratio with spectroscopic splitting factor g, Bohr magneton μ_{B} of electron, Planck constant $h = 2\pi\hbar$, and α is Gilbert damping constant. The magnetization $\vec{M}$ is treated as uniform (within macrospin approximation) with a constant magnitude M_{s} [5, 14]. The first term, τ_H, describes the precession of magnetization due to torque applied by the effective magnetic field $\boldsymbol{H}_{\text{eff}}$. The second term, τ_d, describes dissipation in the magnetic system or magnetic damping that is characterized by the Gilbert constant α [5, 14]. In the absence of damping, the magnetization precesses indefinitely about the effective field at a constant precession cone angle θ_{cone}. The damping causes the precession angle to decrease and returns the magnetization in direction of the effective field at its equilibrium. The general trajectory of the magnetization described by Eqn. (1.11) is a spiral towards the effective field as shown in Fig. 1.4.

Ferromagnetic Resonance

One way to drive the magnetization out-of-equilibrium is by ferromagnetic resonance (FMR). In FMR, the magnetization of the ferromagnet is resonantly excited by applied microwave

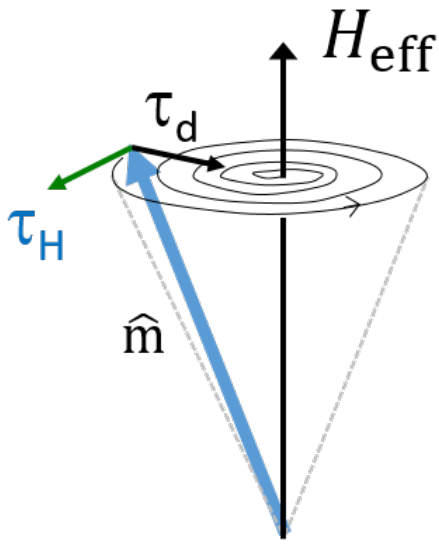

Figure 1.4: **Sketch of magnetization dynamics described by Landau-Lifshitz-Gilbert equation.** At the equilibrium, the direction of magnetization $\hat{\mathbf{m}}$ is along the effective field H_{eff}, in which the magnetic anisotropy energy is minimum. When the magnetization is forced to tilt out of this direction, the magnetization precesses about H_{eff} due to the field torque τ_{H} acting in the tangential direction. The phenomenological damping torque τ_{d} acts to damp out the precession motion of the magnetization through energy relaxation processes and causes the net spiral trajectory of the magnetization towards the H_{eff}.

(RF) magnetic field H_{RF}, which oscillates its amplitude at RF frequency f_{drive} in a given direction. Consider the magnetization in the saturation regime where the magnetization is aligned along the external magnetic field H_{ext}. The RF magnetic field should be applied in the direction transverse to the external magnetic field H_{ext} to effectively tilt the magnetization away from the H_{ext}. In this geometry, the torque induced by RF magnetic field τ_{RF} work against the Gilbert damping torque at the resonance condition, in which the drive frequency f_{drive} coincides with the resonance frequency f_{r} of the magnetization at a given H_{ext}. At the resonance frequency, the sample absorbs the maximum RF power, and a dynamic equilibrium state is achieved. In the dynamic equilibrium state, the magnetization precesses about the H_{ext} at a precession cone angle θ_{cone}, an angle that τ_{RF} balances the damping torque τ_d.

Parametric Excitation

Parametric resonance is another way of excitation of magnetization dynamics, in analogous to parametric excitation in classical mechanics. A well-known example is a mechanics of a child on a swing. In an attempt to generate large swing motion, we learn as a child to bend legs back and forth in a periodic fashion. This reaction modulates the center of mass and, thereby, modulates the moment of inertia, which a parameter of the system. At the proper modulation frequency, which is at near the twice the natural frequency of oscillation of the system, the child can excite large-amplitude oscillations via the parametric resonance.

Parametric resonance is thoroughly studied in bulk and thin-film ferromagnets [15]. In these experiments, the magnetic field, which is a parameter of the magnetic system, is modulated with a drive frequency f_{drive} near twice the FMR resonance frequency f_0 of the system. The parametric drive acts as effective magnetic damping that competes against the intrinsic (Gilbert) damping, and the parametric damping exceeds the inherent damping at a threshold amplitude of the parametric drive [15]. Parametric excitation of magnetization has several advantages over direct excitation by FMR. First, parametric excitation can excite spin wave with non-zero k-vector ($k \neq 0$) in contrast to FMR, which excites the uniform precession of magnetization (spin wave with $k = 0$). Therefore, spin waves with the short wavelength can be excited by selecting the parametric drive frequency twice of the desired spin wave frequency. Also, the parametric excitation can be used as a pumping mechanism for frequency-selective amplification of spin waves [16], and phase error corrections [17]. All these results make the parametric excitation an important tool for manipulating spin wave propagation in the emerging field of nanomagnonics [18, 19]. Nevertheless, parametric excitation by RF magnetic field in metallic ferromagnets is not energy efficient because large RF current is required to generate relatively high threshold fields [20]. In Chapter 6, I address this problem by an electric field (via VCMA) driven parametric resonance and show excitation of magnetization oscillation in metallic nanomagnet at a low-power microwave

drive.

1.5 Spin-transfer Torque

Spin-transfer torque (STT), also known as spin torque (ST), describes a phenomenon that allows manipulation of magnetization by transferring spin angular momentum of injected current. This effect was theoretically predicted by Slonczewski [21] and Berger [22] in 1996, see Ref. [23] for a good review about spin torque physics.

Consider electron transport through a trilayer structure of FM1/spacer/FM2 as shown in Fig. 1.5. The incident current is unpolarized or having randomly oriented spin polarization. When the current pass through the first ferromagnetic layer FM1, the electrons becomes spin-polarized and the direction of spin moment $\hat{\mathrm{p}}$, represented by a red arrow in Fig. 1.5, is parallel to the magnetization of FM1, $\hat{\mathrm{m}}_1$. Next, the spin-polarized current transmits through the non-magnetic spacer layer conserving the polarization and enters the second ferromagnetic layer FM2. Within a distance of the order of 1 nm in the FM2 layer, the spin-polarized electrons experience the local exchange field along the magnetization of FM2 ($\hat{\mathrm{m}}_2$) and become repolarized along the $\hat{\mathrm{m}}_2$ [23]. Any change in the spin-polarization of electrons before and after passing through FM2 layer results the net change of spin moment of the current, $\Delta\hat{\mathrm{p}} = \hat{\mathrm{p}}_{\mathrm{out}} - \hat{\mathrm{p}}_{\mathrm{inc}}$. To satisfy the conservation of momentum, the net change of current moment $\Delta\hat{\mathrm{p}}$ gives rise the spin torque $\vec{\tau}_{\mathrm{st}}$ in the opposite direction ($\vec{\tau}_{\mathrm{st}} = -\Delta\hat{\mathrm{p}}$), in which the ST acts on and reorients the magnetization of FM2.

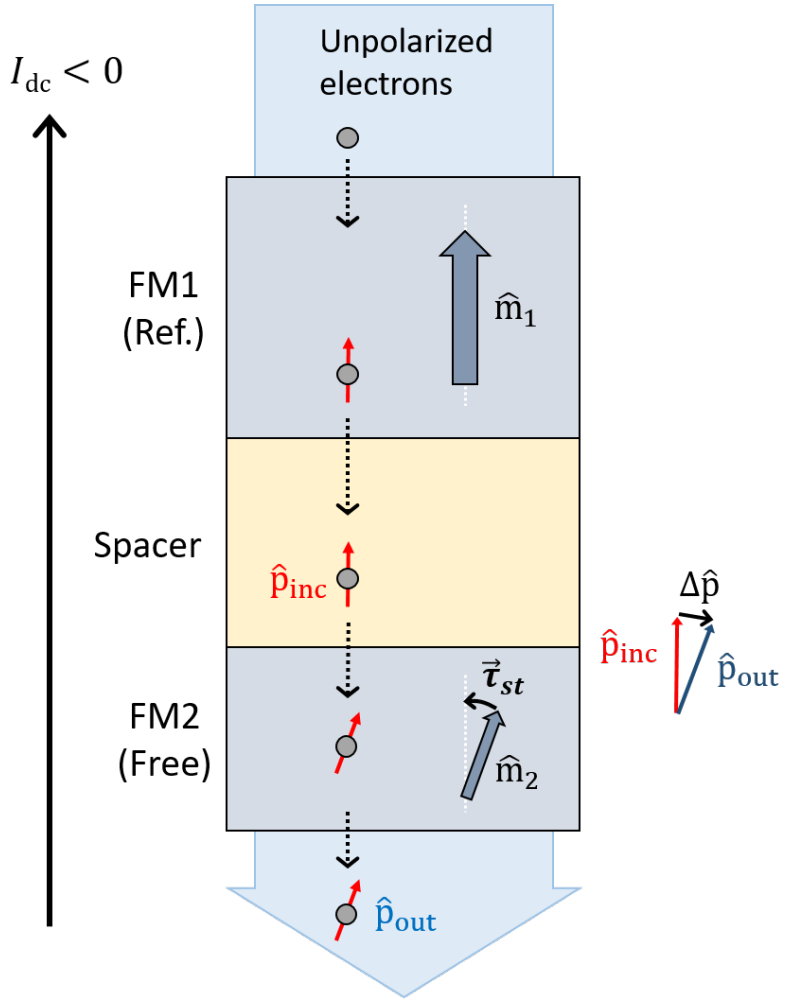

Figure 1.5: **Phenomenological description of spin transfer torque (ST) in an MTJ.** Consider a FM1/spacer/FM2 trilayer structure, where the spacer layer consist of an ultrathin insulating material acting as tunnel barrier, I_{dc} is the direction of electrical (conventional) current, gray circles represent electrons passing through the trilayer, and a large blue arrow in the background represents the net flow direction of electrons. First, electrons passing through the FM1 layer acquire spin polarization, depicted as spin moment $\hat{p}$, in the direction parallel to $\hat{m}_1$, which is the unit magnetization of FM1 layer. Next, as the tunneled electrons traverse the FM2 layer, their spin moment repolarize along the $\hat{m}_2$, the unit magnetization of FM2 layer. If $\hat{m}_2 \neq \hat{m}_1$, the spin moment of incoming and outgoing current passing through the FM2 are in different orientation and causes a net change of spin moment $\Delta\hat{p}$ of the current. Due to conservation of momentum, the difference $\Delta\hat{p}$ give arise spin transfer torque $\tau_{ST} = -\Delta\hat{p}$ acting on the magnetization of FM2. The final outcome is the reoreintation of $\hat{m}_2$ in the direction towards the spin moment $\hat{p}$ of incident current.

Magnetization Dynamics under Spin-torque (ST)

The magnetization dynamics under spin-torque is described by LLG equation, see Eqn. (1.11), with an addition of spin-torque (ST) term, $\tau_{\rm st}$ [23]:

$$\tau_{\rm st} = \gamma \left(\eta \frac{\hbar}{2e} \frac{J_c}{M_{\rm s} t_{\rm FM}} \right) \mathbf{m} \times (\mathbf{m} \times \mathbf{m_{RL}}) \,, \tag{1.12}$$

where $e = |e|$ is the electron charge, η is the spin torque efficiency, and $\mathbf{m_{RL}}$ denotes unit magnetization of reference layer, which spin polarizes the tunnel current that applies ST onto the unit magnetization $\mathbf{m}$. For example in Fig. 1.5, $\mathbf{m_{RL}} = \mathbf{m_1}$ and $\mathbf{m} = \mathbf{m_2}$. $J_c = I_{\rm dc}/A_{\rm FM}$ is the DC electrical current density which flows out-of-plane direction of a FM layer having the unit vector of magnetization $\mathbf{m}$, cross-sectional area $A_{\rm FM}$, the thickness $t_{\rm FM}$. The Eqn. (1.12) is also called damping-like torque because τ_{st} directly modifies the damping torque τ_d in the LLG equation when $\mathbf{m_{RL}}$ is collinear to the effective magnetic field $\boldsymbol{H}_{\rm eff}$. I note that field-like spin-torque term is omitted in Eqn. (1.12), see Ref. [24] for more details.

The subtle physics in the spin-torque term is well discussed in Ralph and Stiles' review paper [23]. Here, I describe an example case for determining the direction of τ_{st} using Eqn. (1.12). Following exposition is based on Ref. [3, 23]. First, $\mathbf{m}$ is the unit magnetization that ST acts on, e.g. free layer of an MTJ and depicted as $\mathbf{m_2}$ in Fig. 1.5. The direction of $\mathbf{m}$ is determined or configured in an experimental setup. For example, application of the external magnetic field along the easy axis of MTJ's unaxial anisotropy sets the $\mathbf{m}$ parallel to the magnetic field. Once $\mathbf{m}$ is known, $\mathbf{m_{RL}}$ direction can be determined with respect to the free layer $\mathbf{m}$ by measuring resistance vs magnetic field. For example, the anti-parallel resistance $R_{\rm AP}$ in Fig. 1.1(b) implies that the $\mathbf{m_{RL}}$ and $\mathbf{m}$ are in the opposite directions. Next step is to figure out the sign of the prefactor in the ST term and, here, a clear definition of J_c is quite critical because all other parameters in the prefactors are positive quantity by its definition. In Eqn. (1.12), the definition of J_c sign is not based on how the electrical voltage

applied to the MTJ electrode but defined based on the net flow of spin-polarized electrons. In Fig. 1.5, J_c is defined positive $J_c > 0$ for electrons flowing from $\mathbf{m}$ (free layer) to $\mathbf{m_{RL}}$ (reference layer) and $J_c < 0$ vice versa. In Fig. 1.5, electrons flow from ($\mathbf{m_{RL}} = \mathbf{m_1}$) to $\mathbf{m}$ and, therefore, $J_c < 0$, which is the conventional current which flows in the direction opposite to electron flow. Following these definitions yield direction of τ_{st} that agrees with Fig. 1.5.

An important outcome of spin torque physics is that spin-polarization of traversing current enables the magnetization manipulation instead of using the magnetic field. Therefore, spin-polarized RF current in an MTJ, which is induced by applying microwave voltage between the MTJ electrodes, can effectively replace the role of RF magnetic field in traditional FMR technique and can excite magnetic dynamics of MTJ layers, e.g., spin wave eigenmodes of the free layer. This technique is called spin-torque ferromagnetic resonance (ST-FMR), see section 2.2 for more details.

1.6 Spin Hall effect and Inverse Spin Hall Effect

The physics of spin torque for spin-polarized electrons can be expanded to the concept of "pure" spin current. Spin current describes flows of spin angular momentum with zero net charge flow. Recently, a generation of spin current by spin Hall effect (SHE) is experimentally discovered, see a review of this topic in Ref. [25]. Both the magnetization switching [26] and persistent magnetization oscillations [27] by the spin torque from SHE generated spin current has been demonstrated.

Spin Hall effect (SHE) is a process that converts injected charge current into a spin current in the transverse direction and originated from spin-dependent electron scattering in the presence of strong spin-orbit interaction [28, 29]. The normal metals that show strong spin-orbit interaction are consist of elements with high atomic numbers also referred as heavy

metals. In particular, Pt, Ta, and W have been shown to exhibit large spin Hall effect [25, 30]. The reciprocal process of SHE is known as inverse spin Hall effect (ISHE), which converts injected spin current into charge current. By exploiting spin to charge current conversion by ISHE or vise versa by SHE in these heavy metals, spin current can be measured or generated, respectively, using the conventional charge-based electronics.

For discussions in this section, I note that $\mathbf{I_c}$ and the subscript "c" denotes the charge current where the charge refers to an electron. Also, $\mathbf{I}_{\mathrm{e}}^{\uparrow}$ denotes the charge (electron) current with spin-up polarization. The spin-up direction denotes the polarization of spin angular momentum $\hat{\sigma}_s$ which is in the opposite direction of spin moment $\hat{\mu}_s$. I note that $\hat{\mathrm{p}}$ used to denote spin moment in the previous sections.

In below, I describe ISHE phenomenologically by starting from spin Hall effect. As presented in Fig. 1.6(a), consider an injection of a net charge current ($\mathbf{I_c} = \mathbf{I}_{\mathrm{e}}^{\uparrow} + \mathbf{I}_{\mathrm{e}}^{\downarrow}$) into the heavy metal with equal amount of spin-up ($\mathbf{I}_{\mathrm{e}}^{\uparrow}$) and spin-down charge currents ($\mathbf{I}_{\mathrm{e}}^{\downarrow}$) that travel initially at the same direction. In the presence of strong spin-orbit interactions, each $\mathbf{I}_{\mathrm{e}}^{\uparrow}$ and $\mathbf{I}_{\mathrm{e}}^{\downarrow}$ experiences spin-dependent scattering processes by mechanisms such as skew-scattering, side-jump scattering, and intrinsic interactions, see Ref. [25] and the references therein. For example in Fig. 1.6(a), $\mathbf{I}_{\mathrm{e}}^{\uparrow}$ scatter into positive y-direction while $\mathbf{I}_{\mathrm{e}}^{\downarrow}$ scatter into negative y-direction according to the orientation of the spin polarization. The outgoing $\mathbf{I}_{\mathrm{e}}^{\uparrow}$ and $\mathbf{I}_{\mathrm{e}}^{\downarrow}$ propagate in an opposite direction to each other in the y-direction, hence net charge current is zero, and results in spin current, net flow of spin angular momentum, in the outgoing direction. Therefore, spin Hall effect converts charge current into spin current.

The opposite process, which converts spin current into charge current, occurs for the inverse spin Hall effect. As shown in the Fig. 1.6(b), consider the spin current ($\mathbf{I_s} = \mathbf{I}_{\mathrm{e}}^{\uparrow} - \mathbf{I}_{\mathrm{e}}^{\downarrow}$) injected into the heavy metal in negative y direction, for example by spin pumping, and experiences the same spin-dependent scattering processes. In this case, each component of spin current $\mathbf{I}_{\mathrm{e}}^{\uparrow}$ ($\mathbf{I}_{\mathrm{e}}^{\downarrow}$) is initially propagating negative (positive) y-direction, which is the *opposite* direction

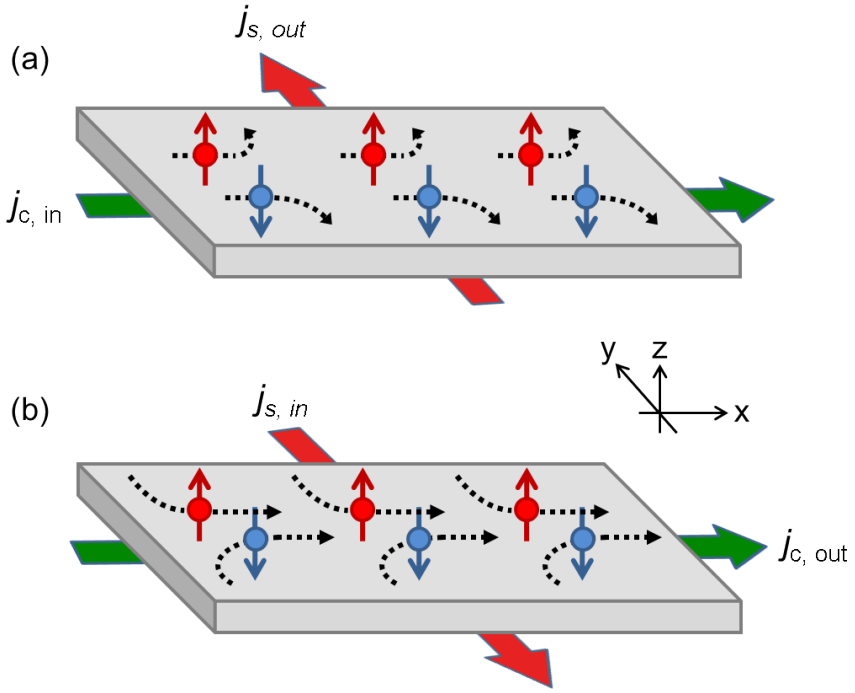

Figure 1.6: **Spin Hall Effect (SHE) and inverse spin Hall effect (ISHE).** (a) In the SHE process, the charge (electron) current density j_c injected in the $+\hat{x}$ is converted to the spin current density j_s outgoing in the $+\hat{y}$ with the polarization $\hat{\sigma}_s \parallel +\hat{z}$. (b) In the ISHE process, the spin current density j_s with the polarization $\hat{\sigma}_s \parallel +\hat{z}$ is injected into the $-\hat{y}$ and converted into the charge current density j_c outgoing in the $+\hat{x}$. Small arrows in z direction represent spin angular momentum σ_s which is in the direction opposite to the spin moment μ_s.

to each other. Therefore both components scatter into the same final direction because each component has the spin polarizations opposite to each other. The result is net charge current with zero spin currents in the outgoing direction, which is x-direction in Fig. 1.6(b). The induced current generates an electric voltage in the direction perpendicular to both the propagation direction and the polarization $\hat{\sigma}_s$ of the spin current density $j_{\mathbf{s}}$ described by [31]

$$\vec{j_c} \parallel \vec{j_s} \times \hat{\sigma}_s, \tag{1.13}$$

where $\vec{j_c}$ and $\vec{j_s}$ describe the charge current density and spin current density, respectively.

The polarization of spin current emitted into the heavy metal by spin pumping has the DC component parallel to the equilibrium direction of the magnetization. In the saturated regime, $H > H_{\text{sat}}$, the equilibrium direction of the magnetization, hence the DC polarization of the spin current is along the external magnetic field direction. Therefore the ISHE generates the DC voltage, which I call ISHE signal, in the direction perpendicular to the direction of the external magnetic field in the plane of the film. The lineshape of ISHE signal V_{sp} is purely Lorentzian [32] and the dependence of in-plane magnetic field direction leads to the reversal of the amplitude sign under the change $H_{\text{ext}} \rightarrow -H_{\text{ext}}$.

$$V_{\text{sp}}(H_{\text{ext}}) = -V_{\text{sp}}(-H_{\text{ext}}) \tag{1.14}$$

1.7 Magnetic Damping

In general, Gilbert damping is present in any magnetic volume. Gilbert damping is characterized by a constant α and phenomenologically describes the energy dissipation from magnetic system to the lattice by spin-orbit interactions [14]. Additional contributions in the damping could exist in a magnetic system of interest. Most notably two-magnon scattering, described

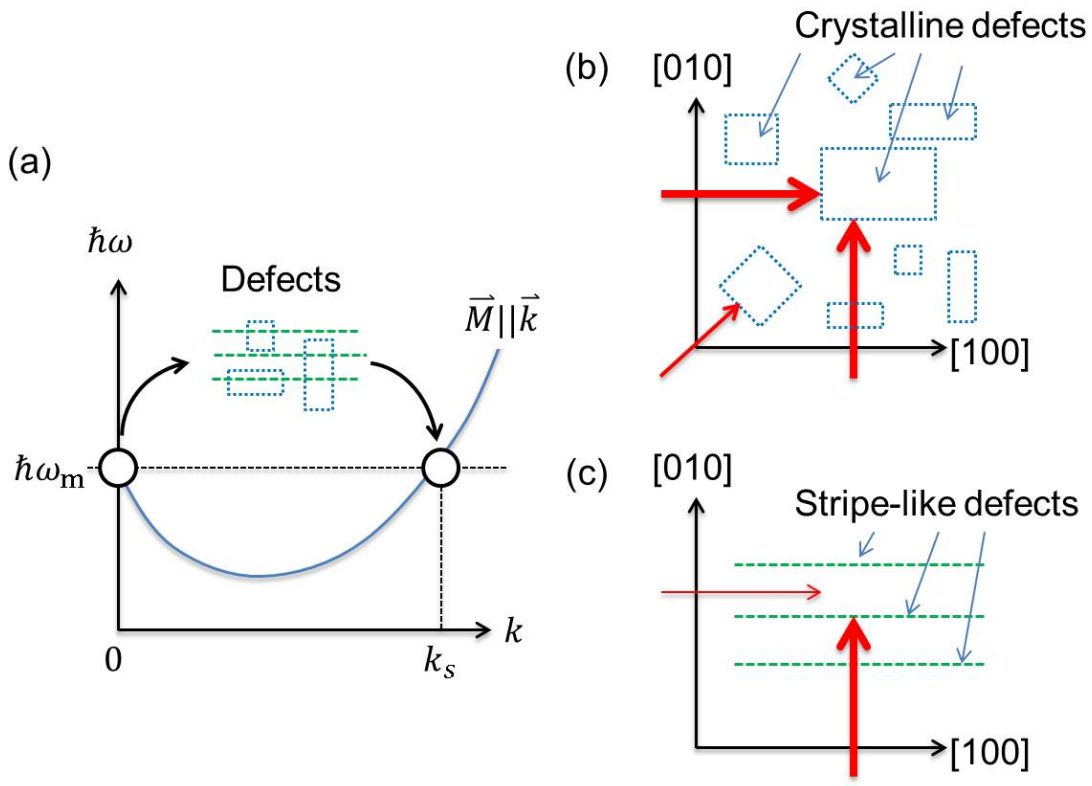

Figure 1.7: **Illustrations of two-magnon scattering.** (a) FMR excites uniform precession of magnetization, which can be described as magnons with $k = 0$ state. The $k = 0$ magnons can scatter by the defects presented in the film into magnons in a degenerate state with nonzero k-vector, $k_s \neq 0$. (b) A cartoon of defect matrices forming the rectangular geometry of various sizes and orientation that are distributed randomly in the film. The red arrows represent the direction of magnetization, and the thickness represents higher scattering rate in the arrow direction. (c) A cartoon of defects forming stripe-like geometry having an uniaxial symmetry. A maximum (minimum) scattering occurs when the magnetization is perpendicular (collinear) to the stripe axis.

in the Section 1.7.1, is an example of magnetic damping related to structural defects or sample impurities. Also, in a ferromagnet/nonmagnetic metal bilayer, spin pumping causes spin angular momentum to leak into adjacent nonmagnetic metal, described in the Section 1.7.2.

1.7.1 Two-magnon Scattering

The two-magnon scattering arises from scattering of the uniform precession of magnetization (magnons with $k = 0$ state) into magnons in a state with the same energy but a finite

k-vector, $k \neq 0$, through defects presented in a thin film, see Fig. 1.7(a). Within Douglas-Mills theory of two-magnon scattering in magnetic thin films [33], the rate of two-magnon scattering depends on the structure of defects and shows anisotropic character following the in-plane symmetry of defects in the film [8, 34]. As a consequence, the FMR linewidth manifest as anisotropic as a function of the in-plane angle ϕ.

In cubic (001)-films, two-magnon scattering exhibits a *four-fold* contribution stemming from the scattering of the crystalline defects and typically presents maxima scattering rate when the magnetization is along <100> axes [34], as illustrated in Fig. 1.7(b). When defects in a stripe-like array with uniaxial symmetry are presented in the film, the two-magnon scattering with a *two-fold* symmetry could arise, as illustrated in Fig 1.7(c). The *two-fold* contribution presents the maximum (minimum) scattering rate when the magnetization is directed perpendicular (collinear) to the uniaxial symmetry axis [8].

1.7.2 Spin Pumping

Spin pumping [35, 36, 37] is another method of generating spin current in the NM layer of FM/NM bilayer system [31, 38, 39]. I briefly outline an underlying mechanism of spin pumping based on Ref. [35, 36]. The precession of magnetization, e.g., excited by FMR in the Fig. 1.8, can dynamically polarize electrons in the NM layer near the FM/NM interface by transferring the transverse component of spin angular momentum from the FM layer. This process induces nonequilibrium spin accumulation at the FM/NM interface which then diffuses as spin current into the NM layer. When the spin current is emitted or pumped freely into the NM layer, the corresponding loss of spin angular momentum in the FM layer is necessary and act as an additional damping source of magnetization dynamics. The damping due to spin pumping α_{SP} has the same form as the Gilbert damping. The effective damping

constant of the bilayer $\alpha_{\mathrm{FM/NM}}$ is [35, 36]:

$$\alpha_{\mathrm{FM/NM}} = \alpha_{\mathrm{FM}} + \alpha_{\mathrm{SP}}, \tag{1.15}$$

where α_{FM} is the Gilbert damping of the isolated ferromagnet, which can be measured by analyzing the frequency dependence of FMR linewidth of a pristine FM film deposited under the identical growth condition of FM in the FM/NM bilayer. Therefore spin pump increases the linewidth of FM/NM bilayer ($\Delta H_{\mathrm{FM/NM}}$) compared to the value of the FM layer (ΔH_{FM}) without any contact to the normal metal.

The magnitude of damping due to the spin pumping α_{SP} depends on the quality of FM/NM interface and the efficiency of the spin current absorption in the normal metal. Platinum (Pt) is used as the normal metal in this work and assumed to have perfect absorption of spin current which is typically adopted in the literature for Pt with $t_{\mathrm{Pt}} \geq \lambda_{\mathrm{Pt}}$, where $\lambda_{\mathrm{Pt}} = 2 - 10\,\mathrm{nm}$ is the range of spin diffusion length in Pt [30, 31, 39, 40]. The quality of FM/NM interface for the spin transport can be characterized by the effective spin-mixing conductance $g_{\mathrm{eff}}^{\uparrow\downarrow}$ [31, 39]:

$$\alpha_{\mathrm{SP}} = \frac{g\mu_{\mathrm{B}}}{4\pi M_s\, t_{\mathrm{FM}}} g_{\mathrm{eff}}^{\uparrow\downarrow}, \tag{1.16}$$

where μ_{B} is the Bohr magneton, g and t_{FM} are the spectroscopic splitting factor and the thickness of the ferromagnet, respectively. Therefore $g_{\mathrm{eff}}^{\uparrow\downarrow}$ can be quantified by measuring α_{sp} from Eqn. (1.15).

DC and AC Spin Pumping

Spin current can be pictured as an equal amount of spin-up and spin-down charge currents (or electron currents) that travel in an opposite direction to each other. In this picture, charge

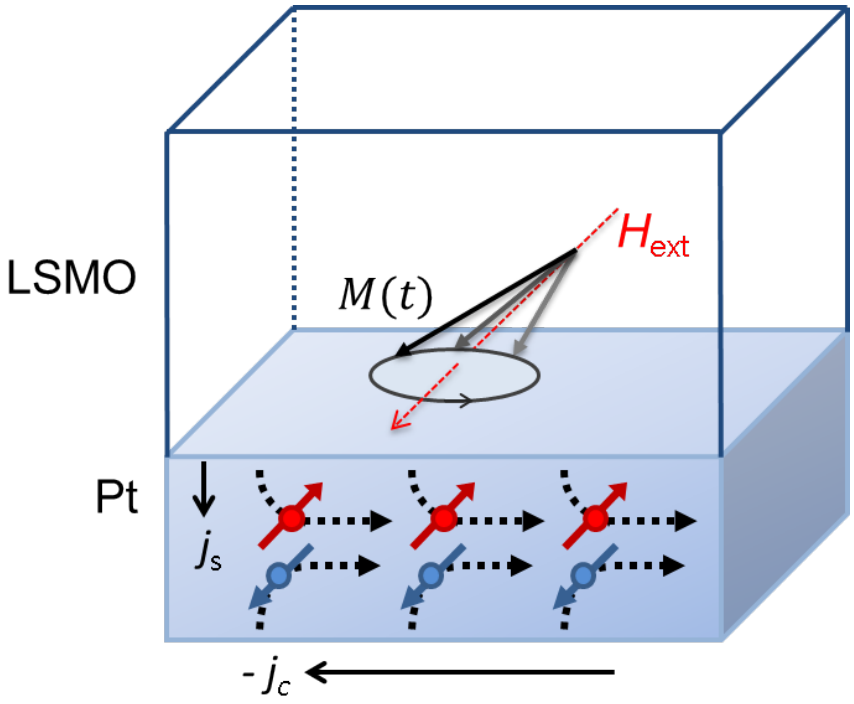

Figure 1.8: **Schematic illustration of spin pumping in Pt/LSMO.** $M(t)$ represents the precessing magnetization, and H_{ext} is directed in the plane of the film. Excitation of dynamical magnetization emits spin current into the adjacent Pt layer which then converted to charge current via inverse spin Hall effect in Pt. The j_{c} and j_{s} are charge (electron) and spin current density, respectively. The red and blue arrows represent spin moments μ_s.

currents are completely canceled but result in a nonzero flow of spin angular momentum [41]. Spin current is defined by the propagation direction and the orientation of the spin polarization [35, 36]. The spin current emitted by spin pumping propagates from FM/NM interface into the NM layer in the direction normal to the interface. The polarization direction of the spin current is transverse to the instantaneous orientation of the processing magnetization and therefore changes at the same frequency as the magnetization precession. However, the polarization direction can be divided into two parts having only the time-independent (DC) and dynamical time-dependent (AC) components. The DC polarization component of spin current, called DC spin pumping, is parallel to the equilibrium direction of the magnetization. So far the spin polarization is discussed in terms of spin angular momentum σ_s, but it may be beneficial to consider in term of spin moment μ_s, which is in the direction opposite to σ_s. Regarding the spin moment μ_s, the polarization of DC spin pumping is antiparallel to the equilibrium direction of the magnetization, see Fig 1.8. In this dissertation, only the DC spin pumping experiments were performed, and I refer it as simply the spin pumping. A more detailed discussion of AC spin pumping can be found in Ref. [42].

Chapter 2

Experimental Methods

In this chapter, I describe a short introduction to ferromagnetic resonance (FMR) and an experimental implementation based on coplanar waveguide for studying magnetic thin-films. Next, I describe an analysis of FMR spectra and interpretation that are also applicable to spin-torque FMR (ST-FMR) technique. I employed an ST-FMR setup for the study of magnetization dynamics in nanoscale magnetic tunnel junctions (MTJs). I describe an experimental setup for highly sensitive ST-FMR technique based on by lock-in amplifier using field-modulation. This configuration enabled the measurement of spin wave eigenmodes of MTJ free layer even in highly symmetric state between magnetizations of free and reference layers.

2.1 Ferromagnetic Resonance (FMR)

Ferromagnetic resonance (FMR) is a technique for probing magnetization dynamics in ferromagnetic materials. In this technique the magnetization of the ferromagnet is resonantly excited by an AC magnetic field H_{RF} oscillating at f_{drive} that are typically in microwave

frequency (RF) ranges. The RF field should be applied in the direction transverse to an external magnetic field H_{ext} to give the maximum amplitude of the excitation at a given microwave power. The ferromagnet absorbs the microwave power at the resonance when the drive frequency f_{drive} coincides with the resonance frequency f_{r} of the magnetization. The decrease in the microwave power due to the absorption by the ferromagnet is experimentally measured in various methods of the microwave circuit, for example, cavity-based setup and coplanar waveguide (CPW) based methods. In this work, CPW-based FMR setup is employed that a magnetic sample is mounted closely onto a CPW board [43]. A microwave diode and a lock-in amplifier are used as a detection unit operated under a field modulation scheme [44]. The FMR spectra, described by a sum of symmetric and antisymmetric Lorentzian functions, is recorded as a function of frequency and magnetic field, so called FMR dispersion. The magnetic anisotropy and magnetic damping in the ferromagnet are extracted from analyzing the frequency and angular dependent FMR spectra.

2.1.1 FMR Spectrometer based on Coplanar waveguide

Coplanar waveguide

A coplanar waveguide (CPW) consists of a coplanar layer of three conductors with thickness d, arranged in ground-signal-ground (GSG) configuration, on a dielectric substrate with thickness h. The microwave signal is applied to the center strip conductor, called signal line, while two outer conductors are ground planes, spaced b away from the signal line. A variant of CPW, called grounded CPW (GCPW) or conductor-backed CPW (CBCPW) is used in this work, which has an additional bottom ground plane connected to top ground planes through conducting bridges called vias, see Fig 2.1(a).

The electromagnetic (EM) wave propagation in GCPW operates in quasi-transverse electromagnetic (TEM) mode [45]. The sketch of static EM field lines in GCPW are shown in

Fig. 2.1(b). Although the direction of microwave magnetic field H_{RF} lies within the plane, it has a nonzero component in the out-of-plane direction especially near the edges of the signal line. The strength H_{RF} is the most dominant in the area above the signal line than above the ground planes. The coplanar ground conductors carry much less current density than the signal line because the ground current is separated by three ground conductors and have broader cross-sectional areas. Therefore the dominant area of FMR absorption occurs above the signal line.

I outline few notes on the design of CPW based on Ref. [45]. Any CPW variations, in general, the EM wave resides in both air, and dielectric substrate and the difference of phase velocity in each region causes unwanted longitudinal EM components, parallel to the axis of the signal line. In GCPW, this problem can be alleviated by allowing GSG coplanar layer to have stronger coupling between GSG interfaces, e.g., more E-field in the air than in the dielectric, to reduce inhomogeneity in the region of the wave propagation effectively. The vias in GCPW are employed to help proper grounding. Also, engineering the vias placements are essential for suppressing unwanted parasitic wave modes and achieving the desired impedance, usually $50\,\Omega$ for microwave devices, or loss characteristic of GCPW. For example, a properly designed GCPW can achieve a constant microwave power loss over a wide range of frequencies up to 50 GHz by minimizing frequency dependence in radiation loss [46]. In the rest of chapters in the dissertation, I will refer GCPW as simply CPW.

CPW-FMR Experimental Setup

The experimental setup for a thin film CPW-FMR measurements is schematically shown in Fig. 2.2. A continuous microwave signal is applied to the CPW and the transmitted signal, via microwave diode, is measured by a lock-in amplifier referenced at a frequency which modulates the external magnetic field. The biggest advantage of using CPW-FMR setup is the broadband capability (0.1 - 40 GHz) having access to both frequency and field-domain measurements with high resolution [43].

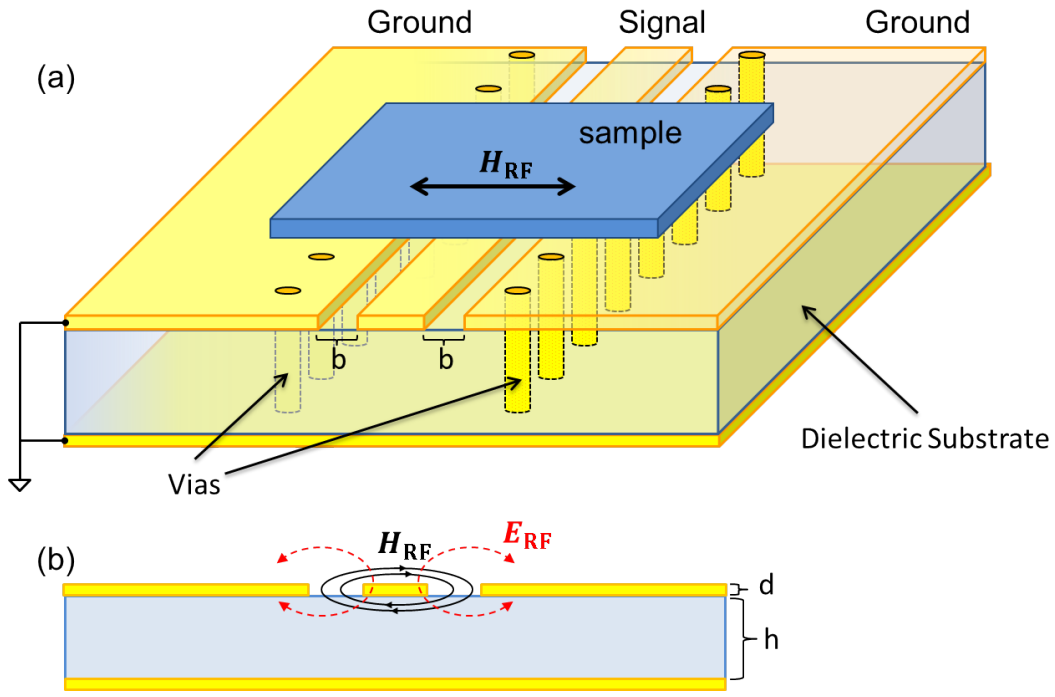

Figure 2.1: **Cross-sectional geometry of a grounded coplanar waveguide (CPW).** (a) Top coplanar layer consist of ground-signal-ground (GSG) planes separated by spacing b. The bottom ground plane is separated from the top GSG layer by a dielectric substrate with thickness h. Conducting bridges called vias electrical connect the upper and lower ground planes. In typical CPW-FMR measurements, a magnetic film is placed face downward closely onto the surface of GSG layer and driving microwave magnetic field H_{RF} is generated in the direction perpendicular to the axis of the signal line. (b) Sketch of static electric and magnetic field distributions of quasi-TEM modes in the CPW.

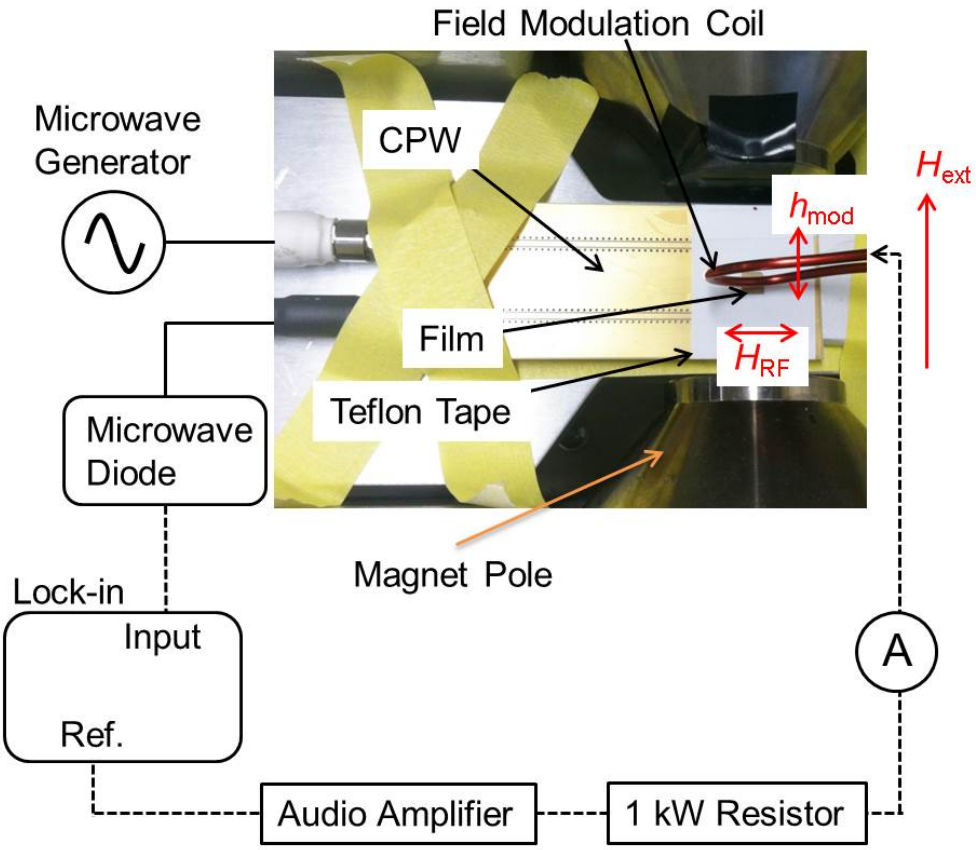

Figure 2.2: **Schematic of CPW based ferromagnetic resonance (FMR) setup.** A magnetic film is placed onto the CPW separated by a single layer of Teflon tape. The CPW board is designed to have a "U" shaped transmission line, and two SMA connectors are connected to microwave generator and microwave diode. Microwave current is sent to one of the RF connector which generates a driving microwave magnetic field, H_{RF}, in the direction perpendicular to signal line axis. The signal line is aligned collinearly with the static external magnetic field H_{ext} which is directed in-plane of the film and makes H_{RF} transverse direction to the external field. A transmitted microwave current through the CPW that arrives at microwave diode gets converted into DC voltage and measured by a lock-in amplifier. The lock-in amplifier is referenced to the modulation frequency of AC current in a field modulation coil. The modulation coil is suspended above the film, and the AC current passing through the coil generates an AC Oersted field, h_{mod}. In the schematics, the straight and dotted lines represent microwave and DC cables, respectively.

The transmission line (GSG coplanar layer) of CPW employed in this work is designed as "U" shape geometry, and a complete CPW unit has two 2.92mm connectors (Southwest, End launch connectors model 1092-03A-6) manually installed. The CPW unit is placed in between the pole gap of an electromagnet (GMW, Model 5403), which provides in-plane external magnetic field. Alignment of the field direction as collinear to the straight section of the transmission line where a sample will be mounted is necessary, see a picture in Fig. 2.2 taken from above of the setup. I wrapped the CPW with a single layer of thread seal tape (also known Teflon tape) of approximately 90 μm thickness, which electrically isolates the sample from CPW conductors. The Teflon tape is slightly stretched to avoid any wrinkles and secured by scotch tape at the back or at near the edge of the CPW. Two 2.92mm connectors are connected to a microwave generator and a microwave diode detector (Keysight, formerly Agilent, Model 8474B, 0.01 - 18 GHz) by RF cables, which is represented as straight lines in Fig. 2.2. The order of this equipment to the connectors does not matter because CPW is symmetrical and the same model 2.92mm connectors are manufactured identically.

Microwave (RF) signal is sent to the CPW from the microwave generator and propagates through the CPW with the generation of microwave magnetic field H_{RF}, see Fig 2.1(b). When the magnetic film is subjected to H_{RF}, the precession of magnetization is excited by absorbing microwave power and decreases the transmitted microwave signal. The transmitted signal arriving at the input of the microwave diode is converted to DC voltage at the output. The DC voltage of microwave diode output is in general sensitive to input microwave power and frequency that nonlinear background signals can arise in addition to any parasitic signals that both are independent of magnetic properties of the film. To increase the signal-to-noise ratio (SNR), suppression of any unwanted nonmagnetic signals is critical. The suppression of nonmagnetic signal is achieved by employing field modulation scheme [44] using a field modulation coil suspended above the magnetic film and CPW as shown in Fig. 2.2.

The field modulation coil is made by bending copper wires in small loops. It delivers mod-

ulation field h_{mod} of few Oersted around the loop by AC current flowing through the coil, typically 1 -4 $\mathrm{A_{rms}}$ modulated at 300 - 2000 Hz in our setup. Above the film, the coil is oriented to make the modulation field collinear with the external magnetic field. The AC current is injected by the audio amplifier (Behringer, Model Europower EP4000). The input AC voltage to the audio amplifier is controlled by the reference output of the lock-in amplifier and output AC current from the amplifier is monitored by an ammeter. A 1 kW (4.7 Ω) resistor (TE Connectivity, Model CJT10004R7JJ) is connected in series between the output of the audio amplifier and the modulation coil to match the load impedance and take the most of the joule heating to avoid overheating of the modulation coil. The 1 kW resistor gets quite warm typically around 3.5 $\mathrm{A_{rms}}$ and any objects nearby the resistor should be avoided all times.

Setup for Angular Dependent FMR Measurements

For identification of several contributions in the magnetic anisotropy and magnetic damping, angular dependent FMR measurement is required as a function of an angle ϕ between external field and in-plane crystallographic direction of the film. At each different angles, the film should be placed ideally at the same location on the CPW and between the electromagnet pole gap. While engineering a mechanical and ideally automated apparatus to place the thin film, usually deposited on a small and thin substrate, onto the CPW is an interesting challenge, it can become expensive and perhaps cumbersome to make. Instead, I achieved this by attaching the film to a transparency paper printed with a polar graph. The angular dependent measurements are carried out by rotating the transparency paper together with film as a whole unit using a tweezer until the angle, and the ideal position of the film is achieved.

The image in Fig. 2.3(a) shows LSMO film facing up on a polar graph that has labels in every 10 degrees. The back of STO substrate, having LSMO film at its front, is attached to a polar

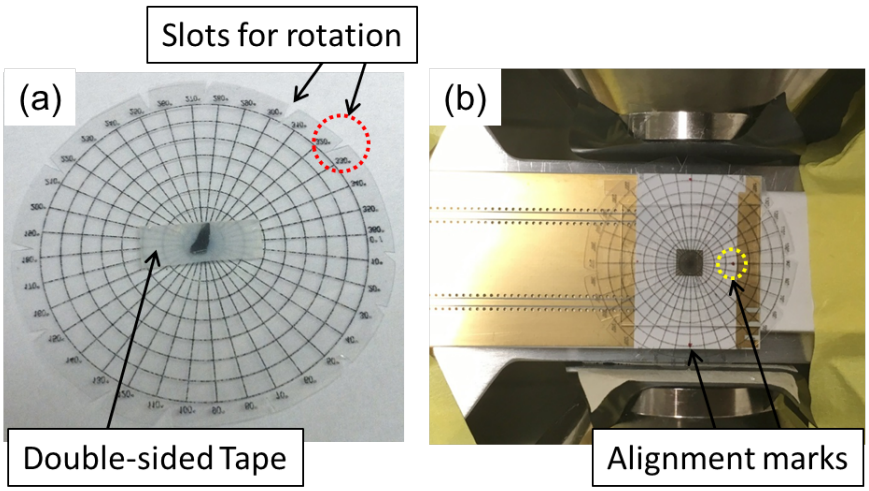

Figure 2.3: **Setup for angular dependent FMR measurements.** (a) The back of LSMO/STO sample is attached to a transparency paper printed with a polar graph via double-sided tape. The image shows LSMO film facing up. The transparency paper is cut into a small circle with "V" shaped slots around its circumference. (b) The polar graph with the sample attached is placed onto the CPW with film facing down. Four small red dots are previously marked on the Teflon tape are used as alignment marks. As the polar graph is rotated or moved by tweezers using the slots as anchoring, the polar graph, and the film as one unit typically moves away from a center position. The film is brought back to the center position for each target angle using the alignment marks and lines in the polar graph as a guide to the eye. A thin glass slide is diced into a small piece and added to the back of the polar graph transparency paper via double-sided tape as a weight.

graph printed on a transparency paper via double-sided tape. Afterward, the transparency paper is cut into a small circle enough to fit between the pole gap, and multiple numbers of "V" shaped slots are created around the circumference edge. Figure 2.3(b) shows a final installment of the polar graph with the film onto the CPW with the LSMO film facing down. The four small red dots are previously marked on the Teflon tape as alignment marks. By inserting the tweezer tip into the "V" slots and the film is rotated to a target angle. As the polar graph is rotated, the polar graph and the film as one unit typically moves away from the ideal center position. The film can be brought back to the center position using the alignment marks and lines in the polar graph as a guide to the eye. The validity of this method is checked by measuring FMR resonance at a random angle, subsequently messing up the angles and the position of the film and then remeasuring the resonance at the same angle. A precise rotation of film can be done by at least 5° resolution within ±2° error.

2.1.2 Measurements of Inverse Spin Hall Effect and Experimental Setup

The second method of measuring spin pumping is an electrical detection of the spin current by inverse spin Hall effect (ISHE), a process that converts injected spin current into charge current. ISHE is a reciprocal process of SHE

Figure 2.4 shows a setup for *in situ* measurements of ISHE signal and FMR. A CPW unit similar to the CPW used in the FMR measurement is modified by adding trenches in the ground planes. The trenches are created by machining at vertical mills without any fluids. The end mills with small diameters determined the trench width and pre-cleaned with acetone and isopropyl alcohol (IPA) to avoid any oil contamination on the CPW. Although machining CPW is easy, some care is given for securing the CPW as it is thin and could be bendable. The area inside trenches defines a conductor pad, and the pad is physically

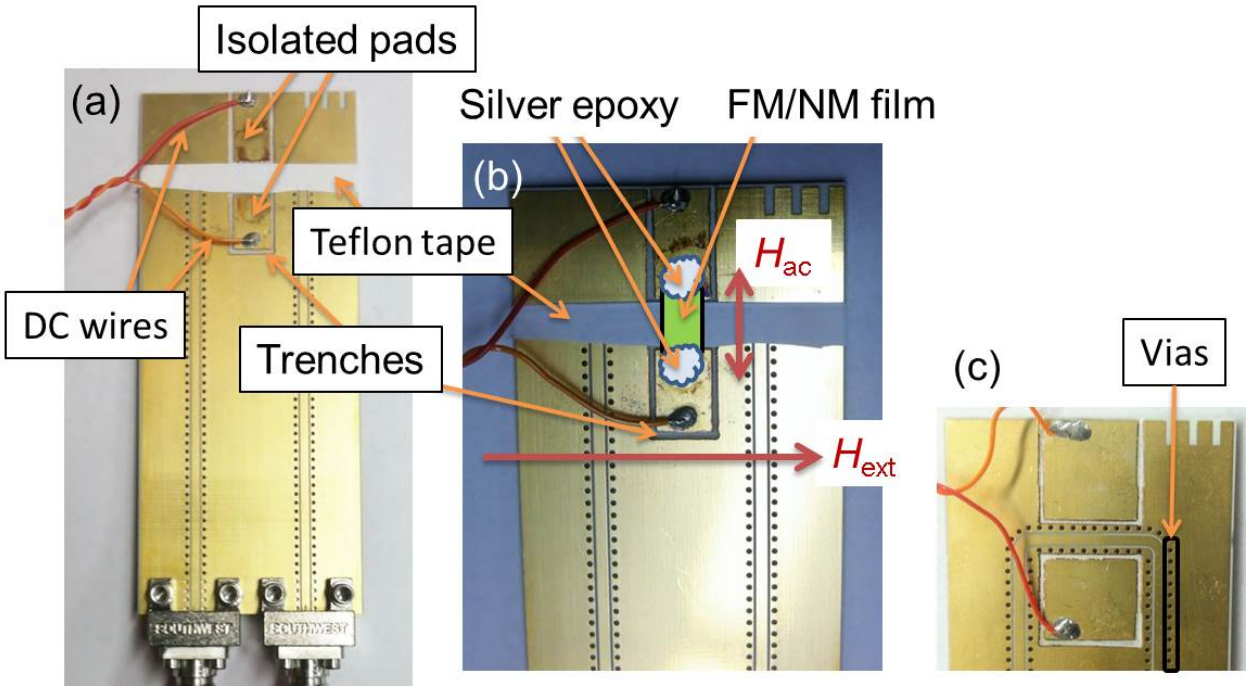

Figure 2.4: **Modified CPW for *in situ* FMR and ISHE measurements.** (a) The CPW board with machined out trenches define electrically isolated pads. The soldered DC wires on each pad are connected to a lock-in amplifier or a voltmeter. Teflon tapes are cut into small width to cover up only the signal line and vias of the CPW. (b) An FM/NM film, presented by a green cartoon rectangle, is placed face down onto the CPW and the Teflon tape isolates the signal line. The film is attached to the pads by silver epoxy, represented as light blue cartoon picture, which provides electrical connections. The external magnetic field is directed collinear to the signal line and transverse to the driving microwave magnetic field H_{RF} to perform spin pumping, and the maximum ISHE signal is induced in the direction perpendicular to the external magnetic field. (c) A close-up picture is showing a different CPW modified for the ISHE measurement. The picture shows machined out trenches as close as possible to Vias. The large-sized isolated pads in this CPW are made to accommodate films having large lateral dimensions.

and electrically isolated from the ground plane of the CPW. Next, DC wires are soldered onto the pads for an easy and secure connection from these pads to the lock-in amplifier or a voltmeter. The Pt/LSMO bilayer film is placed face downward onto the Teflon tape which isolates the film from the signal line of CPW. The film is secured by applying silver epoxy onto the edges of film that extends to each isolated pads and letting it completely dry, see Fig. 2.4(b). The dried silver epoxy also provides a robust electrical connection from the edge of bilayer film to the pad. The silver epoxy is stored in a cold fridge and pre-warm up, approximately 5 min outside, helps to apply it in uniform density.

As FMR absorption is excited predominantly in the area of the film just above the signal line, the ISHE signal is generated in Pt layer between the edges of the signal line. Ideally, electrical contacts from the pads to the bilayer should be made as close as to the edges of the signal line otherwise loss of ISHE signal occurs by shunting through additional conducting areas beyond where the ISHE signal is generated. A practical solution is to create the trenches as close as possible to vias without damaging them, see Fig. 2.4(c). Otherwise, the transmission quality of CPW can be modified.

2.2 Spin-torque Ferromagnetic Resonance (ST-FMR)

Ferromagnetic resonance (FMR) is an important technique for studying both static and dynamical properties of a ferromagnet. However, the sensitivity of conventional FMR techniques is not enough to measure an individual ferromagnet as the size approaches to sub-100-nm-scale [3]. MTJ devices of high interest are in such nanoscale dimension because potential applications for non-volatile memory and signal-processing will be more impactful when high density can be achieved. One way to overcome the lacking sensitivity is to measure an array of many identical nanomagnets to increase the total magnetic volume, but this comes at the expense of measuring an average effect from all nanomagnets in the matrix rather than from

an individual nanomagnet. Spin-torque ferromagnetic resonance (ST-FMR) is a recently developed technique that can detect the precession of magnetization in an individual MTJ even below sub-100 nm size [3, 47].

The ST-FMR exploits the spin torque physics that spin-polarized current can transfer its spin angular momentum to the magnetization of traversing ferromagnetic medium and changes the magnetization direction towards the spin moment, see Section 1.5. By applying microwave (RF) voltage across the MTJ electrodes, RF current can tunnel through the MTJ with its polarization direction oscillating in time at microwave frequency. Therefore, the oscillating polarization of tunneling RF current, I(t) $=I_{\rm rf}\cos(2\pi f_0 t)$, can replace the role of RF magnetic field in conventional FMR technique for inducing magnetization dynamics in FM layers of the MTJ. Based on Ref. [3], the precessing magnetization of MTJ induces time-varying resistance oscillation $R_{\rm MTJ}(t) = R_0 + \sum_n \Delta R_{nf_0}(t)$ via tunneling magnetoresistance, see Section 1.1.

The voltage across the MTJ electrodes $V_{\rm MTJ}(t) = I(t)R_{\rm MTJ}(t)$ contains a mixing term between $I(t)$ and $\Delta R_{f_0}(t)$ and results a time-indpendent DC voltage contribution $V_{\rm mix}$, so called rectified voltage or mixing voltage. At $f_{\rm drive} = f_0$, the magnitude of the rectified voltage is described by [3]:

$$|V_{\rm mix}| = \frac{1}{2} I_{\rm rf} \left|\Delta R_{f_0}\right| \cos\delta_{f_0}, \tag{2.1}$$

where δ_{f_0} is the phase of $\Delta R_{f_0}(t)$ with respect to RF current $I(t)$. As the $f_{\rm drive}$ sweeps through f_0, the amplitude of resistance oscillation $|\Delta R_{f_0}|$ changes with respect to the change in the cone angle of magnetization. The cone angle maximizes at the FMR resonance frequency f_0 and decreases to zero otherwise. This results ST-FMR spectra described by sum of symmetric and antisymmetric Lorentzian [3, 44]. Therefore measurements of a spin-wave eigenmode's resonance frequencies, amplitude, and ST-FMR linewidth as a function of microwave power, DC current, and magnetic field can provide rich informations, e.g. exchange energy, magnetic damping, and spin-torques, that govern the dynamics in magnetic layers in MTJ confined in

nanoscale geometry.

In conclusion, ST-FMR technique can both excites and detects spin-wave eigenmode of magnetic layers an individual MTJ using one electrical experimental setup. The experimental implementation of ST-FMR exploits the fact that the rectified voltage of MTJ described in Eqn. (2.1) is time-independent DC voltage. Applying modulation of RF current I_{RF} or MTJ resistance oscillation $|\Delta R_{f_0}|$ at a modulation frequency f_{mod} results V_{mix} to be modulated at f_{mod}. Therefore, the lock-in amplifier measures only signal at the modulated V_{mix} and filters out any other components at different frequencies $f \neq f_{\mathrm{mod}}$. This effectively increases the signal-to-noise ratio (SNR) of V_{mix} measurement.

Amplitude-modulated ST-FMR. One of the first demonstration of ST-FMR technique utilized lock-in amplifier to increase SNR [3]. In this experiment, the amplitude of injected RF signal into MTJ is chopped at $f_{\mathrm{mod}} = 1.5\,\mathrm{kHz}$ [3]. The amplitude modulation leads to modulation of V_{mix} at the same modulation frequency via modulation of I_{rf}, and lock-in amplifier measures this signal by taking modulation frequency as its reference. This scheme refers to amplitude-modulated ST-FMR setup. Figure. 2.5 shows a circuit diagram of amplitude-modulated ST-FMR setup employed in this dissertation.

Despite all aforementioned capability of amplitude-modulated ST-FMR and its success for characterizing the spin wave eigenmodes in MTJ, this technique typically suffers from frequency-dependent background signals. This unwanted background arises from nonlinearities and impedance mismatches within the microwave circuit. For example, measurements of MTJ in highly symmetric geometry, e.g., collinear alignment of free and reference layer magnetizations, are especially challenging because of both the spin torque and the component of MTJ resistance oscillation $\Delta R_{f_0}(t)$ at the resonance frequency f_0 decreases. This leads to an overall weak rectified voltage in the presence of unwanted non-magnetic background signal. Furthermore, the presence of nonlinear background signal, in general, complicates fitting the spectra and makes the FMR linewidth evaluation quite time-consuming.

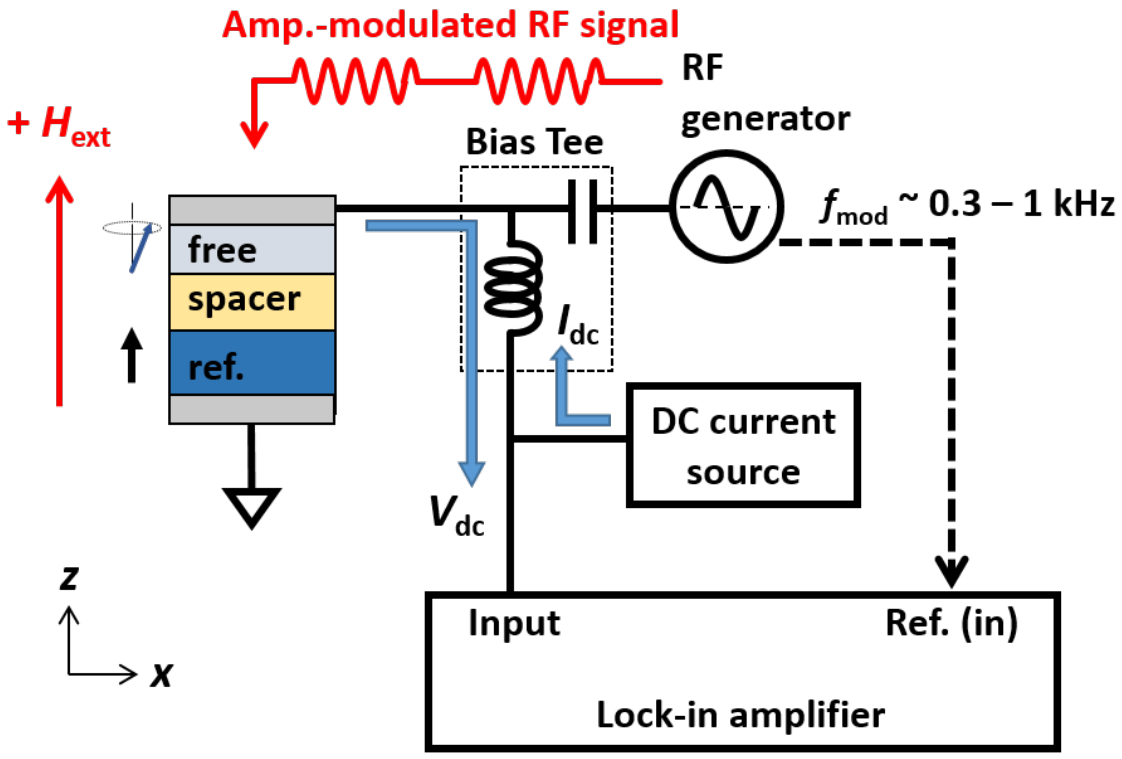

Figure 2.5: **Schematics of amplitude-modulated ST-FMR circuit.** The circuit consists of a microwave (RF) generator, a bias tee, a lock-in amplifier, and optionally a DC bias source for DC current or DC voltage to the MTJ. In this setup, RF current "chopped" at $f_{\mathrm{mod}} = 0.3 - 1\,\mathrm{kHz}$ is injected to MTJ via RF port of the bias tee. The spin-polarized RF current excites magnetization dynamics by spin torque and causes the resistance of MTJ to oscillate at the resonance frequency via tunneling magnetoresistance. The AC resistance of MTJ then mixes with the AC microwave current to produce a DC rectified voltage V_{mix}. The lock-in amplifier measures only the rectified voltage.

Field-modulated ST-FMR. Based on Ref. [44], lock-in amplifier measurement of the rectified voltage under modulated external magnetic field can solve the problem of the parasitic non-magnetic backgrounds. The modulation field can be applied to the sample by adding a suspended copper wire directly above the MTJ sample as shown in Fig. 2.6 and the picture shown in Fig. 2.7(c). The copper wire carries a kHz range sinusoidal current of a few Amperes which generates the modulation field with few Oersted in amplitude. Ideally, the direction of modulation field $H_{\mathrm{mod}} = |H_{\mathrm{mod}}(t)|$ from the copper wire is best to align along the external magnetic field at the sample location. This alignment maximizes the net modulation of the external field $H_{\mathrm{ext}}^{\mathrm{net}}(t) = H_{\mathrm{ext}} + H_{\mathrm{mod}}(t)$ that oscillates at the modulation frequency f_{mod}. A continuous microwave current is applied to the sample via a bias tee, and a lock-in amplifier measures the modulated V_{mix} caused by modulation of ΔR_{f_0} at the modulation frequency f_{mod}. This measurement scheme is called field-modulated ST-FMR technique. The major advantage of field-modulated ST-FMR is the filtering of non-magnetic background signal, which yields even more improved SNR to that of the amplitude modulation scheme [44]. Using the ultrahigh sensitive field-modulated ST-FMR setup outlined in Fig. 2.6, I measured spin-wave eigenmodes of free layer in an MTJ at the collinear alignment of free and reference layer magnetization, see Chapter 4.

2.2.1 Microwave Probe Station with Out-of-plane Magnetic Field

Figure 2.7 showed a full microwave probe station that I built from scratch and carried out ST-FMR measurements reported in this dissertation. The most distinguishing feature compared to two other probe stations in the lab is the capability of applying out-of-plane magnetic field while a microwave probe (GGB Industries, Inc., Model No. 40A, specifically manufactured with no magnetic material) is safely connected to MTJ sample. I achieved this by designing and constructing a sliding base board that moves the electromagnet (GMW Associates, Model No. 3470) back and forth in the lateral direction with respect to the stage, represented

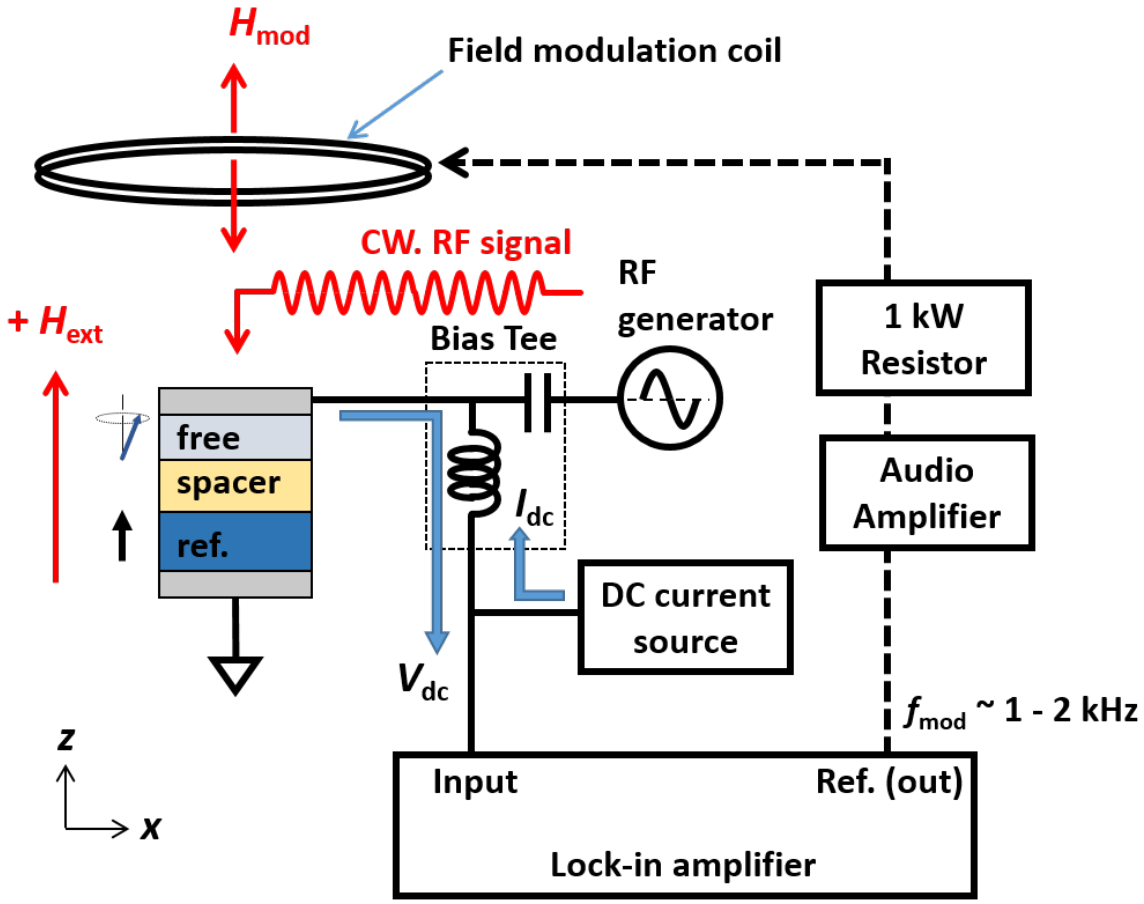

Figure 2.6: **Schematics of field-modulated ST-FMR circuit.** The core of setup is identical to the amplitude-modulated ST-FMR setup shown in Fig. 2.5. Only difference is a modulation coil which provides AC Oersted field H_{mod} oscillating at typical range $f_{\mathrm{mod}} = 1-2\,\mathrm{kHz}$. The AC Oersted field is generated by running AC current through the coil provided by an audio amplifier which is the voltage-to-current converter. In this setup, continuous (CW) RF current is injected into MTJ to excite the magnetization. The rectified voltage is then modulated by the modulation field H_{mod}. The lock-in amplifier detects the rectified voltage by locking in to the modulation frequency f_{mod} of the H_{mod}.

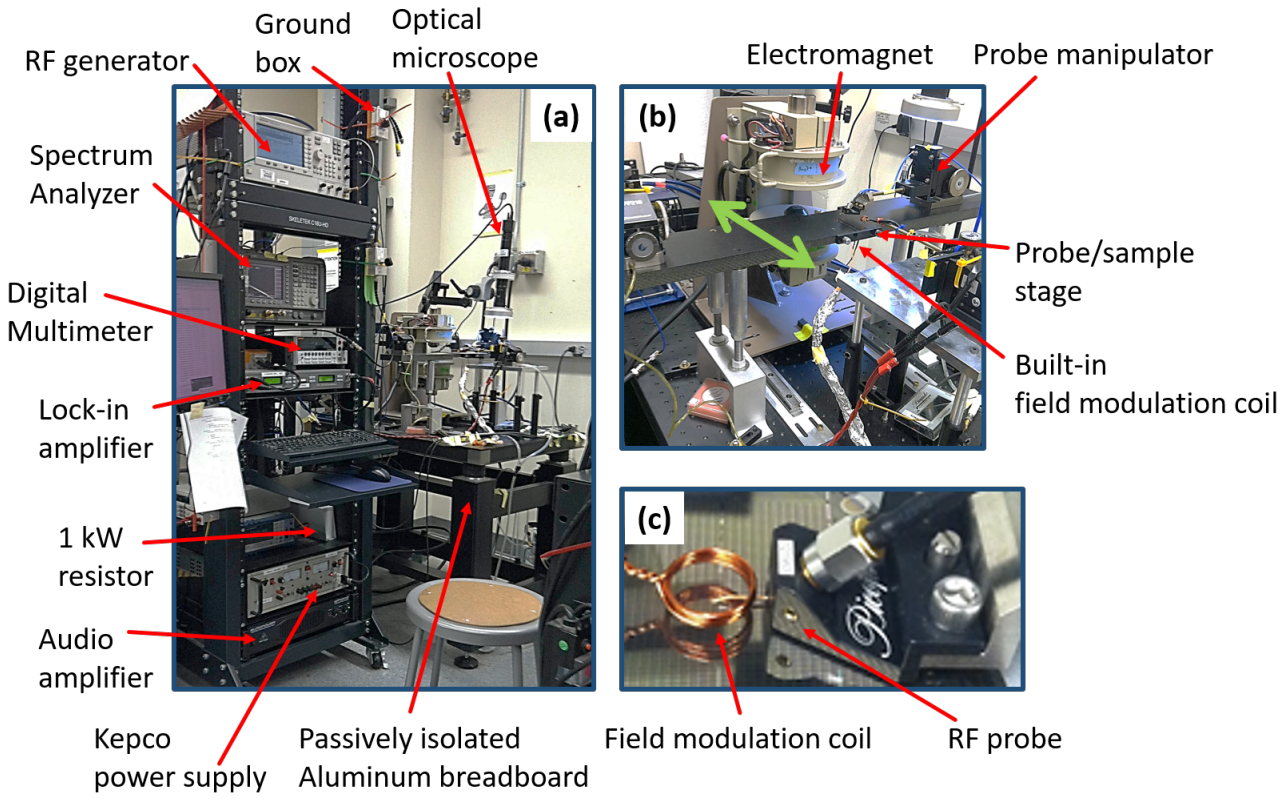

Figure 2.7: **Photograph of the out-of-plane (OOP) magnetic field station.** (a) Bird's eye view of the OOP station including a full electronic rack (Skeletek, Model No. C28U-4P-EX16) and passively isolated aluminum breadboard, which helps to isolate environmental vibration to probe stage. The heaviest equipment such as Kepco power supply and Audio amplifier sits at the bottom of the rack. Also, these are essential to the probe station in our lab and rarely removed. Make-before-switch ground box is homemade and employed in the DC lines of ST-FMR setup to protect damaging sensitive devices from ESD and voltage spikes during the loading of a device to the circuit or changing electronic equipment. (b) The GMW 3470 Electromagnet provides DC applied magnetic field H_{ext} at out-of-plane (vertical) direction concerning the plane of probe/sample stage. The magnet sits on the top of sliding rail, and it can be slid back and forth in the lateral direction, denoted by a green arrow, with respect to width of the probe/sample stage. (c) Close up view of RF probe touch down on the lead pattern of an MTJ device. A ring shaped of copper coils provides field modulation H_{mod}, in out-of-plane direction, parallel to the H_{ext}. The copper coil is suspended directly above MTJ under study.

by a green arrow in Fig. 2.7(b).

To start any measurements using a microwave probe in any probe stations, establishing highly stable contact between the microwave probe and the lead pattern of a device is very critical for acquiring quality data and for longevity of a device under the study. In this regards, connecting to lead pattern of the device all by wire bonding to a closely located CPW is might be better, if a specific device is identified for extensively long measurements to be made. However, the wire-bonding method would require several more preparation steps including designing of sample holders having one or more CPW and adding an extra length of wire-bond leads to extra RF power loss delivered to the sample, which could become a bottleneck for measurements requiring high RF power delivered to the sample. In contrast, probe characterization is more advantageous for quick screening of devices among many in an array, enables investigating multiple devices in a reasonable time frame, and high-quality microwave probe has minimal power loss in a broadband range. Typically performing enough measurements on each device are needed to identify it as good device. Afterwards, I was compelled to continue to carry out extra measurements one after another just using microwave probe because the experimental setup is already put in place. For this purpose, I contributed two improvements to the probe stations in the lab to increase the lifetime of samples by protecting the probe contact to the lead patterns.

First, building a probe station on top of a vibration-isolated optical table reduces any environmental vibrations that couple to the probe stage. I find that passive isolation mounts, which is air-pressured legs made of thick rubber (Thorlabs, Model No. PWA074), between the table frame (Thorlabs, Model No. PFR6090-7) and an aluminum breadboard (Thorlabs, Model No. PBG12106, 2' x 3' x 2.2") give enough isolations of MTJ.

For checking the stability of the microwave probe contact to the lead pattern, one method I find quite useful is monitoring the MTJ resistance vs time, in live plotting of data via Python script, while adding small disturbances to the setup, e.g., sliding the electromagnet

or gently tapping the table with finger tip. When a stable contact is made, the device resistance typically does not change outside of the usual range of resistance fluctuations when the small disturbances are introduced to the setup. The value of resistance variation δR depends on sample and the quality of probe contact to lead pattern and δR should be determined before deliberate disturbances are introduced to the setup, e.g., monitoring resistance vs time for enough period. One would also find overall drift of resistance when measured over an extended period. If weak contact is made, the MTJ resistance typically shows a sudden changes or jumps while the electromagnet is slid or tapping the table. In this case, I recommend establishing a new contact, inspect and cleaning the tip of microwave probe, see [24] for more details about probe handling and maintenance. Ideally, planarization of the microwave probe is recommended at the beginning of new setup. The planarization method consists of taking a flat substrate with pre-deposited gold pads, touch down the microwave probe on to the gold pad and carefully observe the grove made by sliding the microwave probe. The observation of uneven grove shape, or its shadow under the optical microscope, at each landing spot for ground "G" and signal "S" probe tip, indicates uneven level between the GSG probe tips. Therefore, by making a horizontal tilt of probe arm at the probe manipulator "planarizes" the level between GSG probe tips.

2.2.2 Calibration of External Magnetic Field and for Frequency Dependent Microwave Power

External magnetic field calibration. Having the most accurate strength of magnetic field is a must for any measurements involving magnetic field as one of the experimental knobs. At a fixed gap between the poles of an electromagnet, static magnetic field is generated by supplying constant DC current, via BOP Kepco power supply, which runs through coils of the electromagnet. Each Kepco power supplies and GMW electromagnets in our lab has its mating pair, which is based on the maximum output current of the power supply

and the maximum current the GMW electromagnet can take before overheating occurs. For example, GMW 3470 is paired with Kepco BOP 50-8M power supply. According to the GMW 3470 specification, the electromagnet coils can take up to a continuous 5.0 A, 44 V (220 Watt) when water cooling is used. The Kepco BOP models come in at 100, 200 and 400 Watt models and BOP 50-8M is the best available model that can supply up to 5.7 A at 50 V for the GMW 3470's coil resistance at 8.8 Ω.

The magnitude of DC current at the output of BOP Kepco power supplies in our lab are all control by input DC voltage (-10 V $< V_{\text{input}} <$ +10 V) applied to the control input connector, which located at the front panel of the power supply. The input DC voltage is usually provided by DAC output of a lock-in amplifier. Here, $V_{\text{input}} = 10$ V results the positive maximum available output current. Therefore, the maximum $V_{\text{input}}^{\text{max}} \leq 10$ V has to be carefully set to avoid overheating of the electromagnet.

The field calibration refers to calibration of the generated magnitude of magnetic field by an electromagnet (for a given gap between the pole pieces and at a desire location of between the gap) as a function of the input DC voltage V_{input} at the Kepco. The field calibration should be recalibrated every time the pole gap is changed, or measurement location between the pole gap is different than the existing calibration data.

The most updated field calibration method is carried out in the following steps.

1. Place the Hall sensor of 3-axis Hall probes (Lake Shore Cryotronics, Inc., Model No. 460) at the location where the magnetic field calibration needs to be made.
    - The 3-axis Hall probe outputs magnetic field readings at H_x, H_y, H_z, and H_{mag}, the total magnitude. The sign of magnetic field can be determined using the sign of either H_x or H_y by placing either sensor along the direction of magnetic field.
2. Make calibration data: record H_{mag} and the sign of H_{mag} as a function of V_{input} applied

to the Kepco.

- Due to hysteresis of electromagnet, both sweep direction of V_{input} should be recorded, e.g. V_{input} from $-V_{\text{input}}^{\text{max}}$ to $V_{\text{input}}^{\text{max}}$ and vice versa.
- The maximum voltage $V_{\text{max}} \leq 10\,\text{V}$, where $10\,\text{V}$ is the maximum input voltage at the control connector of Kepco power supply. Practically, $V_{\text{input}}^{\text{max}}$ depends on the electromagnet, its cooling method in use, and the paired Kepco power supply. To prevent an excessive heating, each GMW electromagnet has built-in thermoelectric switch which senses the temperature of the electromagnet coil and automatically turns off the Kepco power supply via wire bundles connecting between the electromagnet and the back of Kepco power supply. The wire bundles are manufactured by GMW and for each type of the GMW electromagnet and its paired Kepco power supply units.

3. Fit the field calibration data.

- Fitting to higher-order polynomial is fast, easy to apply and interpret method but it could lose accuracy of field near the $V_{\text{input}}^{\text{max}}$ where H vs V_{input} can become quite nonlinear depending on the electromagnet. I find that employing interpolation function can improve the accuracy even near the V_{max}.

Power calibration and Method of Reducing RF standing waves. Whenever a connection is made to assemble RF circuit, e.g., ST-FMR setup, the connection reflects propagating RF electromagnetic wave. This creates a standing electromagnetic waves between two connection points. In ST-FMR setup, the standing electromagnetic waves manifest as oscillating background as a function of RF frequency. The frequency between the two peaks of the standing wave is governed by the length of reflection points by

$$v = \Delta f \lambda, \tag{2.2}$$

where v is velocity of electromagnetic wave in a microwave cable, e.g. $v = 0.7c$, where c is speed of light. Δf is the average separation between electromagnetic standing waves in the RF circuit, and wavelength $\lambda = 2L$. Analyzing Eqn. (2.2) gives the length L of section, between the most dominant reflection of electromagnetic waves, in the RF circuit where the dominant standing wave occurs.

For reducing the standing wave background, try increasing the length of RF cable at the section or added microwave attenuator. An idea behind here is to effectively increase the attenuation reflected signal so that less reflection to occur, although this sacrifices available maximum RF power that the RF generator can inject to the sample due to the overall increase of attenuation.

Next, step for reducing the standing wave background in ST-FMR spectra is performing power calibration of RF circuit. The effective RF power arriving at any point in the RF circuit is measured using a power sensor (e.g. Agilent, E4413A CW Power Sensor, 50 MHz - 26.5 GHz, 100 pW - 100 nW) attached to a power meter (Agilent, Model No. E4418B EPM Series Power Meter). The power sensor is connected directly to the location RF circuit where the power calibration is to perform. For example, in typical ST-FMR setup, I perform the power calibration at the location just before connecting to the microwave probe. A general procedure for making the power calibration is first to record the raw RF power level (called Zeroth-order correction) arriving at the location that the calibration is carried out. Then adjust the power level of RF generator until the target RF power is reached by compensating the overall net power loss based on the zeroth-order correction. Record the new arriving power (called 1st-order correction). Although one can add more corrections to get better-calibrated signal, I find that the improvement gain of Power calibration quickly decreases beyond the 2nd-order correction and not worth the time. In my experience, power calibration up to 2nd-order correction yield the noise in the calibrated RF power $\delta P \simeq \pm 0.05$ dBm for Agilent RF generators (Agilent, Model No. E8275D), which the lowest noise RF generators available in our lab.

2.3 Extraction of Magnetic Anisotropy from FMR Dispersion

In FMR or ST-FMR, the magnetization of the ferromagnet is resonantly excited by microwave magnetic field at driving frequency f_{drive}. In this work, the FMR spectrum is taken in the field-domain that the magnitude of magnetic field is swept at a constant drive frequency f_{drive}. As the magnitude of magnetic field H is swept, the corresponding resonance frequency f_{r} changes. The resonance condition occurs when the drive frequency f_{drive} coincides with the resonance frequency f_{r} and the microwave power is absorbed by the sample. The resonance signal $V(H)$ is in general described by the sum of symmetric and antisymmetric Lorentzian $L_s(H) = [1 + ((H - H_{\mathrm{r}})/\Delta H)^2]^{-1}$ and $L_a(H) = [(H - H_{\mathrm{r}})/\Delta H][1 + ((H - H_{\mathrm{r}})/\Delta H)^2]^{-1}$, respectively [44, 48]:

$$V(H) = S\ L_s(H) + A\ L_a(H), \tag{2.3}$$

where H denotes the magnitude of the external magnetic field, ΔH is the FMR linewidth (half-width at half-maximum), S and A are the amplitude of symmetric and antisymmetric Lorentzian, respectively. The antisymmetric Lorentzian $L_a(H)$ arises when a nonzero phase difference between the microwave electric and magnetic field occurs due to the losses of the microwave propagating inside the CPW and the ferromagnetic material [48].

In this work, I measured FMR absorption in the field domain under the field modulation scheme. When the modulation field h_{mod} is small compared to the FMR linewidth ΔH, the voltage signal measured by the lock-in amplifier is proportional to the first derivative of the $V(H)$ with respect to the modulated external magnetic field [44]:

$$V_{\mathrm{mod}}(H) \propto S\ \frac{dL_s(H)}{dH} + A\ \frac{L_a(H)}{dH}, \tag{2.4}$$

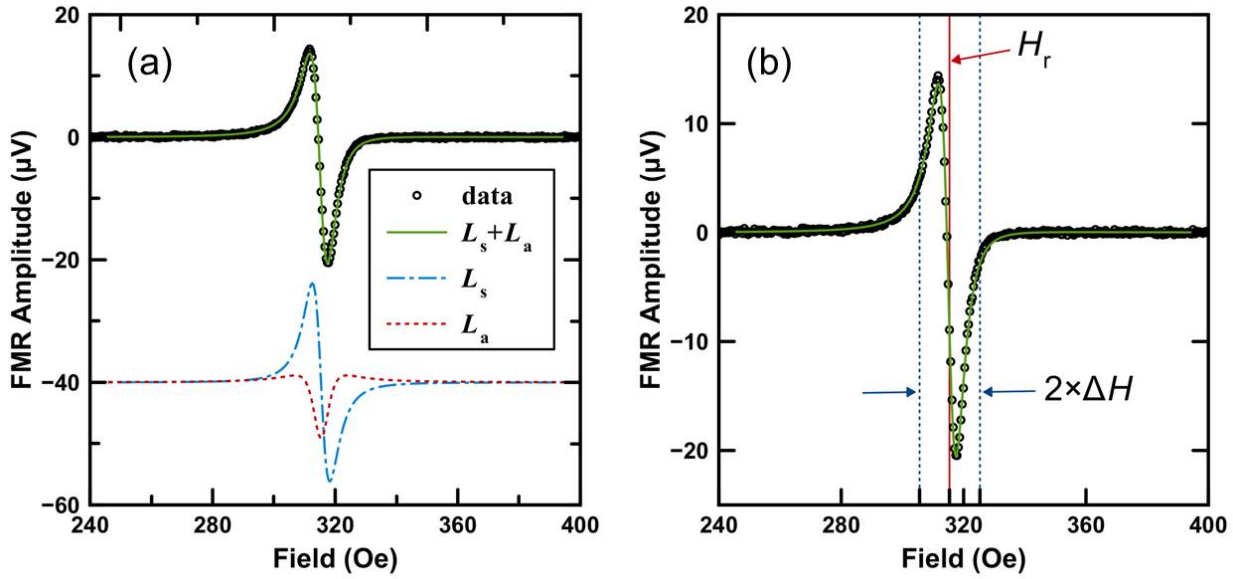

Figure 2.8: **Example of field-modulated FMR spectrum of LSMO(30 nm) measured at 4 GHz frequency in the field domain.** (a) The data, black open circles, shows a single absorption profile and well fitted, green straight line, to the Eqn. (2.4). The symmetric Lorentzian L_s (blue, dotted-dash line) and antisymmetric L_a (red, dotted line) are shown with offset for clarity. (b) The resonance field $H_r = 315.4$ Oe and FMR linewidth $\Delta H = 4.9$ Oe are extracted from the fit.

Figure 2.8 shows a typical field-modulated FMR spectrum of LSMO thin film on STO(001) substrate. The data, black open circles, is well fitted (green straight line) to the Eqn. (2.4) by a single FMR absorption profile. The symmetric and antisymmetric components of Lorentzian from the fit are shown in Fig. 2.8(a) with the offset for clarity. I note that in the field-modulated FMR spectrum, the symmetric (antisymmetric) Lorentzian appears as antisymmetric (symmetric) profile with respect to the resonance field H_r, respectively. The resonance field H_r and half width at half maximum FMR linewidth ΔH are extracted from the fit as shown in Fig. 2.8(b). The relationship between microwave frequency and resonance field called FMR dispersion gives information about static magnetic properties, e.g. the spectroscopic splitting factor g and magnetic anisotropy fields, latter may depend on the magnetization orientation with respect to the crystallographic direction. The linewidth ΔH is directly related to the magnetic damping.

Resonance Condition. Under resonant excitation, the torque generated by the microwave field balances the damping term and the remaining equation of motion is that of Eqn. (1.11) without the second term, forcing a precession at the resonance frequency of the system. The resonance condition is formulated by the Smit and Beljers in 1955, also by Suhl at the same time [5, 14]:

$$\left(\frac{2\pi f}{\gamma}\right)^2 = \frac{1}{M^2 \sin^2\theta}\left[\frac{\partial^2 F}{\partial\theta^2}\frac{\partial^2 F}{\partial\phi^2} - \left(\frac{\partial^2 F}{\partial\theta\partial\phi}\right)^2\right], \tag{2.5}$$

where f is the resonance frequency, $\gamma = g\mu_B/\hbar$ is the gyromagnetic ratio, g is the spectroscopic splitting factor [14], and μ_B is the Bohr magneton. The partial derivatives in Eqn. (2.5) are evaluated at the equilibrium angles θ_{eq} and ϕ_{eq}, which are obtained from minimizing the total free energy density F of the system, see Ref. [5] for more details.

Simulation of FMR Dispersion. From the FMR experiment, the resonance field H_r at different microwave frequency f (f vs H data or FMR dispersion) are collected and compared to the Eqn. (2.5) to determine magnetic anisotropies in the system. In this work, calculation of the resonance frequency is carried out by writing a Python script as a function of the magnetic field and in-plane angle of the field ϕ referenced to the crystal axis [100]. The initial value of fitting parameters g, H_1, H_{mc}, H_{uni} and ϕ_{uni} are first assigned and carried out the calculation to simulate FMR dispersion; I refer it as simulation dispersion. Subsequently, the simulation dispersion is compared to the experimental FMR dispersion, and the value of fitting parameters are adjusted until the best simulation result to the data is achieved. To increase the accuracy, a set of FMR dispersion data is taken at different angles, e.g., $\phi = 0, 40, 90^\circ$ in this work, and all compared simultaneously to a set of simulation dispersions at the same angles, generated while using the identical value of the fitting parameters. Furthermore, angular dependent FMR data are collected at few different microwave frequencies. Following the procedure outlined for the simulation of FMR dispersion, the angular dependent FMR can be simulated and compared to the data for fine-tuning of fitting parameters.

2.4 FMR Linewidth and Magnetic Damping Contributions

The finite value in FMR linewidth ΔH results from magnetic damping and magnetic inhomogeneities in the magnetic system [34]. Although phenomenological Gilbert damping exists in any magnetic system that is characterized by Gilbert damping constant α_0, additional magnetic relaxation mechanisms can coexist in the system of interest. For example, spin pumping in a ferromagnet/nonmagnetic metal bilayer system (see section 1.7.2) and two-magnon scattering in magnetic thin films are the additional contributions of magnetic damping studied in this dissertation. In general, the FMR linewidth is described by

$$\Delta H = \Delta H_{\text{inh}} + \frac{2\pi f \alpha_0}{\gamma \Psi} + \sum_k \Delta H_k, \tag{2.6}$$

where k is an index label for additional contributions in the magnetic damping, e.g., $k =$ sp, 2m, etc., to be added as these are identified to exist in the system with significant contributions. The first term represents the line broadening due to inhomogeneity of the sample and has two components: a constant term and a mosaicity term of the form $\propto \partial H_{\text{r}}/\partial \phi_H$ [34, 49]. The second term describes Gilbert damping which is proportional to the Gilbert constant α_0. In this dissertation, both α and α_0 are used interchangeably to denote the Gilbert constant. A correction factor $\Psi = \cos(\phi - \phi_H)$ accounts the field dragging effect that occurs when the magnetization is misaligned with respect the external field [49].

If spin pumping contribution is important and requires to extract away to get the intrinsic Gilbert damping constant α_0 of an isolated ferromagnet, $\Delta H_{\text{sp}} = 2\pi f \alpha_{\text{SP}}/(\gamma\Psi)$ is added to Eqn. (2.6), see Section 1.7.2. If two-magnon scattering becomes significant in the system, $\Delta H_{\text{2m}} = (\gamma\Psi)^{-1} \sum_j \Gamma^{ij}_{\text{2m}}$ is added. The two-magnetic scattering can have multiple contributions of having different symmetry axis of scattering and $\Gamma^{ij}_{\text{2m}} = \Gamma^j_i \xi^j_i(\phi)\zeta(f)$, where i and j

are indices labeling the symmetry of the two-magnon scattering channel and the axis of the maximum scattering rate for this channel, respectively. The corresponding scattering rates are Γ_i^j. As described in Refs. [8, 34, 33, 50], $\xi_2^j(\phi) = \cos^4(\phi - \phi_{2,j}^{\max})$ for the two-fold symmetry channel and $\xi_4^j(\phi) = \cos^2(2(\phi - \phi_{4,j}^{\max}))$ for the four-fold symmetry channel, where $\phi_{i,j}^{\max}$ is the angle of the maximum scattering rate. The frequency dependence $\zeta(f)$ of the two-magnon scattering is described in Ref. [33].

Notes on Evaluation of FMR Linewidth

1. In ST-FMR spectra of an MTJ, multiple spin-wave eigenmodes could be measured. For evaluation of magnetic damping in MTJ, the ST-FMR linewidth evaluation is carried out using the lowest frequency mode of MTJ because it usually has the best signal-to-noise ratio at given RF power compared to higher-order modes. Although a full analysis of the spatial profile of spin wave modes in MTJ, via micromagnetic simulation, is desirable, the lowest frequency mode of MTJ is often quasi-uniform mode where the relative phase and amplitude are spatially near uniform [44]. The quasi-uniform mode is a close analog to the uniform mode excited by FMR in a thin film and, therefore, the damping equation derived from LLG equation, Eqn. (2.6), the most applicable to the lowest frequency mode of the MTJ.

2. Field dragging effect occur whenever the equilibrium direction of magnetization is misaligned with the external magnetic field H_{ext} and due to magnetic anisotropy field present in the system. This effect vanished for easy and hard axis in the saturated regime, for which H_{ext} and M_{eq} are in parallel: $\phi = \phi_H$ and results $\Psi = 1$. Making good alignment at the hard axis of an MTJ takes time-consuming calibration. Also, even in easy axis configuration of MTJ, small curvature in the MTJ resistance vs field can be observed especially near the switching field of the MTJ. For MTJs with the reference layer is strongly fixed, and in the direction of applied field, any change in MTJ

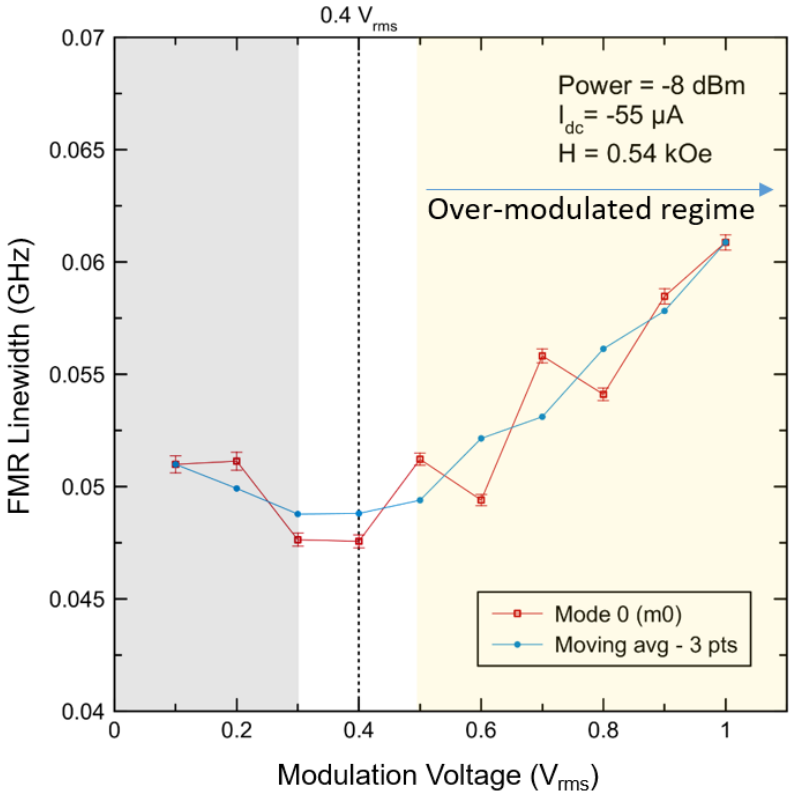

Figure 2.9: **Example of over-modulation effect in FMR linewidth from field-modulated ST-FMR measurements.** In this measurement setup, the magnetic field and DC bias are chosen to result in the lowest FMR linewidth of the measured MTJ. Red circles are the measured data, and it has small fluctuations between data points (approx. 30-50 MHz). Blue circles are result of taking 3 points moving average of the data. The FMR linewidth is minimum at the modulation voltage V_{mod} at $0.4\,V_{\text{rms}}$. For $V_{\text{mod}} \geq 0.6\,V_{\text{rms}}$, over-modulation occurs and broadening of the measured FMR linewidth is observed.

resistance implies a finite distance between free layer magnetization and the external field. Therefore field dragging can cause the FMR linewidth to increase as the field approaches the switching field and this range of field should be avoided in the damping evaluation.

3. Using too large step size Hstep can cause bad measurement of FMR absorption profile and lowers the accuracy of the FMR linewidth evaluation. A rule of thumb is to use $H_{\text{step}} \leq \frac{1}{10}(2 \times \Delta H)$, where ΔH is the FMR linewidth measured at half width at half maximum (HWHM) and $(2 \times \Delta H)$ is the full width at half maximum (FWHM).

4. When using the FMR or ST-FMR measurement setup that employs field-modulation scheme, over-modulation can cause the measured FMR linewidth ΔH to broaden when modulation field $H_{\mathrm{mod}} > \Delta H$. In ST-FMR setup, the reference output of the lock-in amplifier supplied modulation voltage V_{mod} at $0.4 - 1.2\,\mathrm{V_{rms}}$ and feed into the audio amplifier (Europwer, Model No. EP4000) that converts the input AC voltage into AC current. The AC current is then sent to the modulation coil that generates AC modulation field of typically a few Oersted [44], depending on the height displacement of the copper coil with respect to the MTJ device under the study. The modulation voltage is proportional to the generated modulation field H_{mod} by the coil. When the H_{mod} exceeds the FMR linewidth, an over-modulation effect occurs and increases the FMR linewidth. This effect is the most significant at small linewidth, which corresponds to low resonance frequency region according to Gilbert damping. Figure 2.9 shows the FMR linewidth taken at a fixed magnetic field as a function of the modulation voltage. Over-modulation effect is observed when the $\mathrm{V_{mod}} \geq 0.6\,\mathrm{V_{rms}}$ where the measured FMR linewidth starts to increase. The small broadening that occurs $\mathrm{V_{mod}} < 0.3\,\mathrm{V_{rms}}$ is usually observed in our setup, and its origin is not well understood. In conclusion, the intrinsic FMR linewidth is measured using $\mathrm{V_{mod}} = 0.4\,\mathrm{V_{rms}}$ in this setup and over-modulation effect in the damping analysis will be negligible at this value.

Chapter 3

Magnetic anisotropy, Damping, and Spin transport in Pt/LSMO Bilayers

The contents of this chapter are adapted from work originally published as *AIP Advances*, 6, 055212 (2016).

3.1 Introduction

Spin transport across an interface between nonmagnetic metal (NM) and ferromagnet (FM) by spin Hall effect (SHE) [25] and spin pumping [35, 36, 37] is central to manipulation of magnetization dynamics driven by pure spin currents. To date, significant focus has been set on FM/NM heterostructures comprising 3d materials [26, 30, 51, 52] with a recent extension to yttrium iron garnet (YIG) [53, 54, 55]. While these systems provided great insights about underlying physics of SHE and the spin pumping [30, 55], transition metal ferromagnets exhibit high saturation magnetization and large magnetic damping that result in high critical current densities in SHE-based magnetic memories [26] and spin torque oscillators [27, 56].

For enriching these applications, identification of new material platforms for the efficient generation, transmission, and conversion of spin currents will be greatly beneficial.

In this context, perovskite manganite $La_{0.7}Sr_{0.3}MnO_3$ (LSMO) is an attractive ferromagnet because it has low saturation magnetization, and expected to show low magnetic damping owing to its half-metallic nature [57]. In this chapter, I present ferromagnetic resonance measurements of magnetic anisotropy and damping in epitaxial LSMO films grown on $SrTiO_3$ (001) (STO) substrates with and without Pt cap. I observe low magnetic damping and efficient interfacial spin transport in this system, which makes Pt/LSM bilayer a promising candidate for spintronic devices utilizing pure spin currents.

3.2 $La_{0.7}Sr_{0.3}MnO_3$ (LSMO)

The crystal structure of a perovskite manganite $La_{0.7}Sr_{0.3}MnO_3$ (LSMO) is shown in Fig. 3.1. From the generic form ABO_3 of a perovskite structure, lanthanum (La) or substitutionally doped (30%) strontium (Sr) atoms occupies the "A" sites and form a cubic unit cell. Manganese (Mn) atoms occupy at the "B" site surrounded by oxygen atoms and form a MnO_6 octahedron [58]. This system exhibits rich interactions between the charge, spin, orbital, and lattice degrees of freedom leading to complex electronic and magnetic phase diagrams, e.g. a doping-dependent metal-insulator transition, paramagnetism, ferromagnetism, and antiferromagnetism [58].

In the emerging field of spintronics, LSMO is perhaps best known for its half-metallic band structure having 100% spin polarization at the Fermi surface, for more details see Ref. [58] and the references therein. The half-metallicity makes LSMO an attractive candidate as spin-filtering material in magnetic tunnel junctions (MTJs) for generation of spin-polarized currents. For example, tunneling magnetoresistance ratio of 1800% at 4 K is demonstrated in

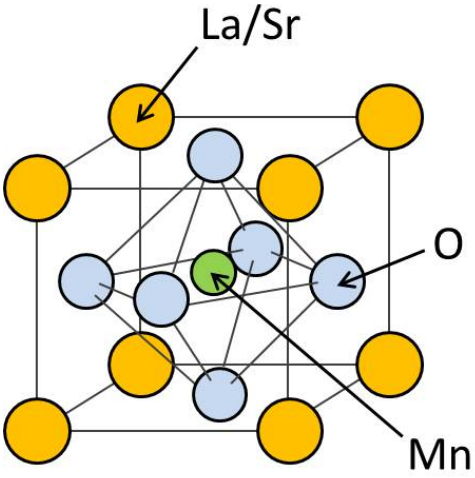

Figure 3.1: Crystal structure of $La_{0.7}Sr_{0.3}MnO_3$ (LSMO) is perovskite-based structure having a general form ABO_3. In LSMO, lanthanum (La) or substitutionally doped (30%) strontium (Sr) atoms occupies the "A" site and the manganese (Mn) atoms occupies the "B" sites surrounded by oxygen atoms forming a MnO_6 octahedron.

Ref. [59] due to spin polarization of at least 95% in LSMO electrodes. In addition, LSMO has high Curie temperature (T_C) above room temperature and low saturation magnetization [60]. In fact, the half-metallic nature is expected to result in low magnetic damping [57, 61]. All these properties are favorable for reducing critical current density in spin torque oscillators having LSMO as the active layer, in which the manipulation of magnetization dynamics occur. Lastly, this oxide system can be grown epitaxially with atomically sharp interfaces [62, 63], holding a great potential as a tunable platform to enable interfacial engineering [64].

Growth of LSMO Thin Films. The LSMO films and the X-ray diffraction (XRD) characterizations in this work are provided by the H. Y. Hwang group at Stanford University. LSMO thin films were grown on TiO_2-terminated $SrTiO_3(001)$ (STO) substrates by pulsed laser deposition (PLD) as described in Ref. [60]. Enhanced metallicity in the thin limit (≥ 7 unit cells) with high Curie temperature $T_C \approx 360$ K are exhibited in the films grown under these conditions [60]. During growth, the thickness of LSMO film was monitored by *in situ* reflection high-energy electron diffraction (RHEED) and all LSMO films with

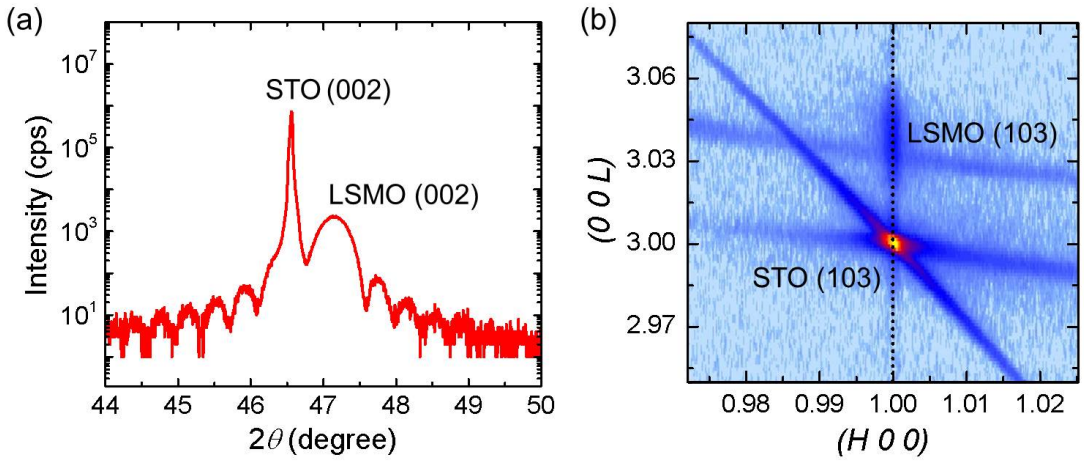

Figure 3.2: **X-ray diffraction of epitaxial LSMO(25 nm) on STO (001) substrate.** (a) θ-2θ scan near the (002) peak. (b) Reciprocal space map near the (103) peak.

various thicknesses appear in this dissertation was grown under the same conditions. The XRD structural characterization of the LSMO(25 nm) thin film is shown in Fig. 3.2(a). The θ-2θ scan around the STO (002) peak shows finite thickness fringe patterns of a uniform, highly crystalline, epitaxial LSMO film. Figure. 3.2(b) shows the reciprocal space map of the (103) peak which confirms the fully strained LSMO thin films to the substrate and epitaxially grown along the (001) orientation. Pt layer was deposited *ex situ* using an e-beam evaporator for Pt/LSMO bilayer films.

3.3 Results and Discussions

Ferromagnetic Resonance of LSMO Thin Films. I employ coplanar waveguide (CPW) based broadband ferromagnetic resonance (FMR) with magnetic field modulation to measure magnetic properties of LSMO films and Pt/LSMO bilayers. All measurements are performed at room temperature. A typical FMR spectrum shown in Fig. 3.3 is well fit by a single absorption profile described by the field derivative of a sum of symmetric and antisymmetric Lorentzians [44]. Previously, LSMO thin films typically shown to exhibit a strong satellite

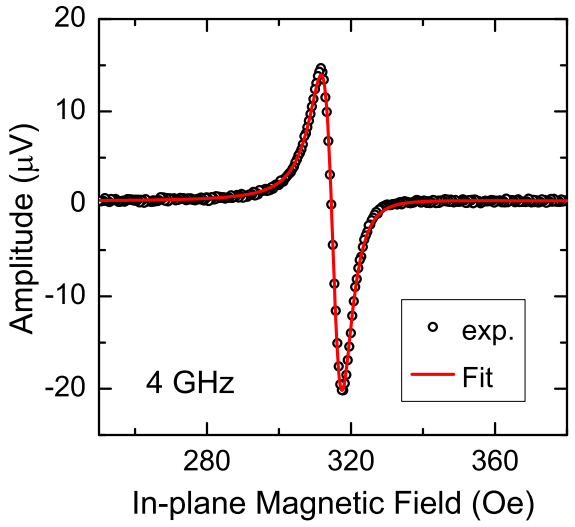

Figure 3.3: A typical field-modulated FMR spectrum of LSMO(30 nm) measured by a sweeping magnetic field at a constant 4 GHz. FMR spectrum is well fitted to a single FMR absorption profile described by Eqn. (2.4).

absorption peak [65]. This mode has a negligible amplitude in the samples, and I will focus discussions on the dominant FMR mode.

3.3.1 LSMO(30 nm) on STO(001)

Magnetic Anisotropy. First, I study the magnetic anisotropy of uncapped LSMO(30 nm) thin films. Figure 3.4(a) shows the resonance field as a function of in-plane magnetic field angle ϕ_H with respect to the [100] axis. The data shows a dominant uniaxial magnetic anisotropy (UMA) with its easy axis parallel to the [010] crystallographic axis at $\phi_H = 90°$. Frequency-dependent FMR measurements shown in Fig. 3.4(b) confirm the uniaxial character as the data taken at $\phi_H = 0°$ presents typical hard axis FMR dispersion with a curvature near saturation field $H_{\rm sat} \simeq 46$ Oe. Based on these observations, the total free energy density

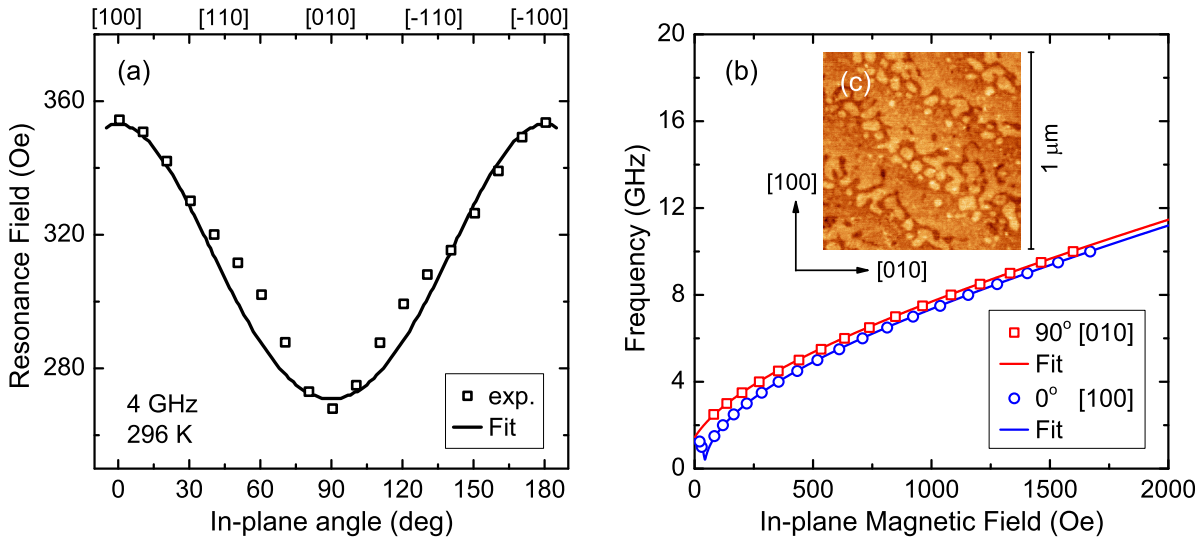

Figure 3.4: **LSMO(30 nm).** (a) FMR resonance field vs in-plane angle ϕ_H measured at 4 GHz. (b) Frequency vs resonance field for easy axis (squares) and hard axis (circles). (c) AFM topography of the LSMO surface. The AFM image shows terraces with step-edge orientation of 125° with respect to [100]. Data are taken at room temperature and all error bars are smaller than the symbol size.

[5] of magnetization is model by:

$$\begin{aligned} F_{\text{total}} = &-\vec{M}\cdot\vec{H} + \frac{1}{2}M_{\text{s}}H_1\cos^2\theta \\ &-\frac{1}{16}M_{\text{s}}H_{\text{mc}}(7+\cos\,4\phi)\sin^4\theta \\ &-\frac{1}{2}M_{\text{s}}H_{\text{uni}}\cos^2(\phi-\phi_{\text{uni}})\,\sin^2\theta, \end{aligned} \tag{3.1}$$

where θ and ϕ are the polar and azimuthal angles of the magnetization $\vec{M}$ measured from [001] and [100], respectively, and $\vec{H}$ is the external magnetic field. The first term in Eq. (3.1) is the Zeeman energy. The second term is the effective out-of-plane magnetic anisotropy with $H_1 = 4\pi M_{\text{s}} - 2K_{\perp}/M_{\text{s}} - H_{\text{mc}}$, where $K_{\perp}$ is the perpendicular magnetic anisotropy (PMA). The third term describes the four-fold magnetocrystalline anisotropy (MCA) with effective field $H_{\text{mc}} = 2K_{\text{mc}}/M_{\text{s}}$. The last term is the in-plane UMA with anisotropy field H_{uni} and its easy axis at ϕ_{uni}.

The Smit and Beljers formalism [5, 14] is used to fit the FMR data:

$$\left(\frac{2\pi f}{\gamma}\right)^2 = \frac{1}{M_s^2 \sin^2\theta}\left[\frac{\partial^2 F}{\partial\theta^2}\frac{\partial^2 F}{\partial\phi^2} - \left(\frac{\partial^2 F}{\partial\theta\partial\phi}\right)^2\right], \tag{3.2}$$

where f is the resonance frequency, $\gamma = g\mu_B/\hbar$ is the gyromagnetic ratio with spectroscopic splitting factor g and μ_B is the Bohr magneton. Eqn. (3.2) is evaluated at the equilibrium angles θ_{eq} and ϕ_{eq} obtained from minimization of the free energy density in Eqn. (3.1).

I employ Eqn. (3.2) to simultaneously fit the frequency- and angle-dependent FMR data in Fig. 3.4(a,b) with g, H_1, H_{mc}, H_{uni} and ϕ_{uni} as fitting parameters, see section 2.3 for details. The small differences between the experimental data and the fit in Fig. 3.4(a) cannot be reduced even by introducing the second-order MCA term (not shown here). The best fit returns $g = 1.975$ and $H_1 = 6380\,\text{Oe}$, which are similar to the values reported in Ref. [66] and Refs. [67, 68], respectively. At this room temperature measurement, MCA field is found to be negligibly small ($|H_{mc}| < 1\,\text{Oe}$) despite the epitaxial nature of our LSMO films. The in-plane magnetic anisotropy is dominated by the UMA term with $H_{uni} = 42\,\text{Oe}$ and $\phi_{uni} = 90°$ given by the best fit. With room-temperature value of $M_s \approx 265\,\text{emu/cm}^3$ [60] and the negligibly small MCA field H_{mc}, our epitaxial LSMO films on STO(001) exhibit negative PMA ($K \approx -4.0\times10^5\,\text{erg/cm}^3$) comparable to previous reports [67, 68]. The negative PMA results in-plane preference of magnetization and positively adds to the shape anisotropy, see section 1.2.

The UMA was previously observed in LSMO films grown on STO(001) and its easy axis was found to be parallel to the atomic terrace edges of the miscut substrate [69, 70]. Figure 3.4(c) shows atomic force microscope (AFM) topography of the same film investigated by FMR. The AFM image shows step-and-terrace features with 0.39 nm step height consistent with single LSMO unit cell [60], and approximately 250 nm terrace width stemming from a slight miscut of the STO substrate. The step edges of the terraces are oriented at 125° with respect

to [100] and this orientation is not correlated with either the symmetry axes of the crystal or the measured uniaxial magnetic anisotropy. Therefore the origin of uniaxial magnetic anisotropy is not related to the substrate miscut and its origin remains unclear.

Magnetic Damping. I analyze the FMR linewidth data to quantify magnetic damping of our LSMO films. The linewidth is found to be strongly angular dependent in the film plane with a four-fold and a two-fold components as shown in Fig. 3.5(a). Such anisotropic linewidth has been experimentally observed in other epitaxial film systems and explained in terms of two-magnon scattering that follows the in-plane symmetry of defects in the film [8, 34, 33, 50]. In particular, the four-fold contribution in cubic (001)-films arises from crystalline defects and typically presents maxima along <100> axes [34]. The two-fold contribution arises from defects with uniaxial, stripe-like symmetry and presents maxima at directions perpendicular to the uniaxial symmetry axis [8].

Based on Refs. [8, 34], the FMR linewidth ΔH (half width at half maximum) can be formulated by following ansatz:

$$\Delta H = \Delta H_{\mathrm{LF}} + \Delta H_{\mathrm{inh}} + \frac{2\pi f \alpha}{\gamma \Psi} + \frac{\sum_j \Gamma_{2\mathrm{m}}^{ij}}{\gamma \Psi} \tag{3.3}$$

The first term describes the low-frequency contribution that arises from inhomogeneous microwave field of the CPW. It has the form $\Delta H_{\mathrm{LF}} \propto f^{-\rho}$ [71, 72]. The second term represents the line broadening due to inhomogeneity of the sample and has two components: a constant term and a mosaicity term of the form $\propto \partial H_{\mathrm{r}}/\partial \phi_H$ [34, 49]. The third term describes Gilbert-type damping which is proportional to the Gilbert constant α. It includes a correction factor $\Psi = \cos(\phi - \phi_H)$ accounting for the field dragging effect [49]. The last term reflects the two-magnon scattering with $\Gamma_{2\mathrm{m}}^{ij} = \Gamma_i^j \xi_i^j(\phi)\zeta(f)$, where i and j are indices labeling the symmetry of the two-magnon scattering channel and the axis of the maximum scattering rate for this channel, respectively. The corresponding scattering rates are Γ_i^j. As

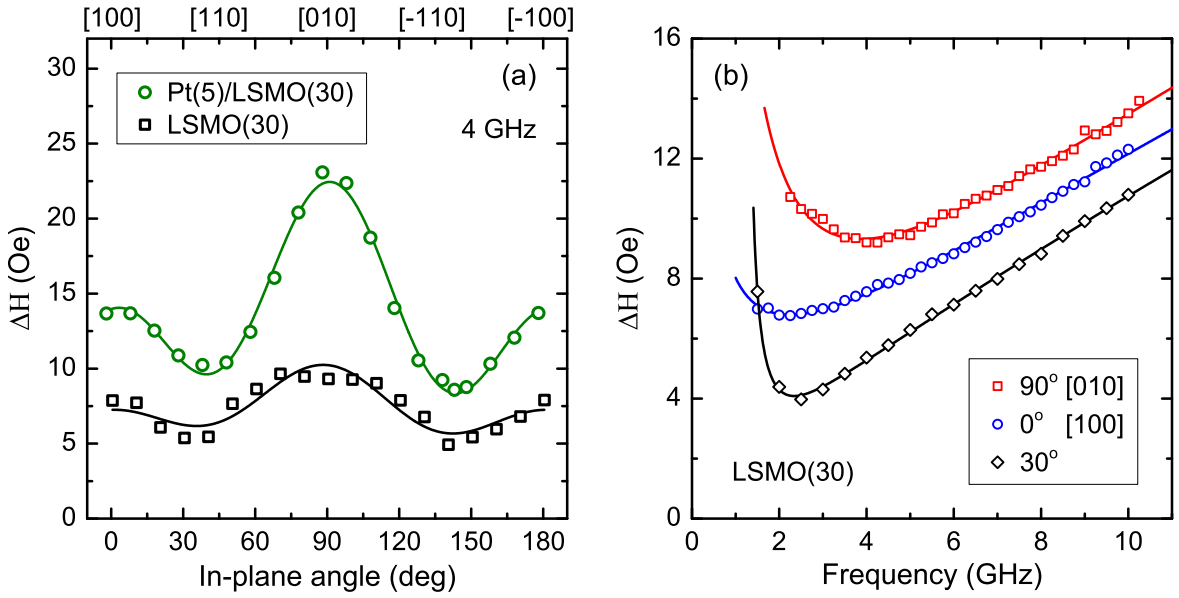

Figure 3.5: (a) FMR linewidth (ΔH) as a function of in-plane magnetic field angle ϕ_H for LSMO (squares) and Pt/LSMO (circles) films at 4 GHz. (b) Frequency-dependent FMR linewidth for the LSMO film at three values of ϕ_H. The lines show the best fit.

described in Refs. [8, 34, 33, 50], $\xi_2^j(\phi) = \cos^4(\phi - \phi_{2,j}^{\max})$ for the two-fold symmetry channel and $\xi_4^j(\phi) = \cos^2(2(\phi - \phi_{4,j}^{\max}))$ for the four-fold symmetry channel, where $\phi_{i,j}^{\max}$ is the angle of the maximum scattering rate. The frequency dependence $\zeta(f)$ of the two-magnon scattering is described in Ref. [33]. Due to the distinctive angular- and frequency-dependence of each term in Eqn. (3.3), I can unambiguously fit the data in Fig. 3.5 and extract all damping parameters.

From the fit shown in Fig. 3.5(a), the rates of two-magnon scattering with four-fold and two-fold contributions are $\Gamma_4^{\langle 100\rangle} = 2.4(3) \times 10^8$ Hz, $\Gamma_4^{\langle 110\rangle} = 0.9(3) \times 10^8$ Hz, and $\Gamma_2^{[010]} = 2.5(4) \times 10^8$ Hz, respectively. The four-fold two-magnon scattering shows maxima along $\langle 100\rangle$, as expected for the (001) film [34]. The two-fold term $\Gamma_2^{[010]}$ presents maximum at [010]. This direction does not correspond to either the hard axis of the UMA in contrast to the expected behavior [8] or to the terrace orientation observed in AFM topography. In fact, the stripe-like terraces of the LSMO film generate a weak additional two-fold two-magnon scattering channel with $\Gamma_2^{\perp\text{step}} = 0.4(4) \times 10^8$ Hz at $\phi_{2,\perp\text{step}}^{\max} = 35°$ which is the perpendicular

to the step-edge orientation ($\phi = 125°$) as expected [8].

The best fit gives the Gilbert constant $\alpha_{\mathrm{LSMO}} = 1.9(1) \times 10^{-3}$. This value is low among reported values of LSMO films on STO(001) [65, 73]. Also, this value is comparable to the lowest values reported for metallic ferromagnetic films: $\alpha = 2.3 \times 10^{-3}$ in epitaxial $Fe_{1-x}Si_x$ [74], 2.1×10^{-3} in epitaxial Fe-V alloy [75], and 1.0×10^{-3} in Co_2FeAl [76]. The inhomogeneous line broadening is found to be small for our LSMO films $\Delta H_{\mathrm{inh}} = 1.3\,\mathrm{Oe}$, with a negligible mosaicity contribution $\leq 0.7\,\mathrm{Oe}$.

3.3.2 Pt(5 nm)/LSMO(30 nm) on STO(001)

Magnetic Anisotropy and Damping. Next, I study the effect of adding a Pt capping layer to LSMO films. The best fit to the resonance field data of Pt(5 nm)/LSMO(30 nm) film returns $g = 1.975$, $H_1 = 6410\,\mathrm{Oe}$, and $|H_{\mathrm{mc}}| < 3\,\mathrm{Oe}$. These values are very similar to those of the bare LSMO film. The UMA field $H_{\mathrm{uni}} = 36\,\mathrm{Oe}$ decreases by 14% while retaining its easy axis along [010]. The FMR linewidth analysis shows that the two-magnon scattering rates are significantly increased compared to the bare LSMO film without change of their symmetry: $\Gamma_2^{[010]} = 7.3(2) \times 10^8\,\mathrm{Hz}$, and $\Gamma_4^{\langle 100\rangle} = 5.7(1) \times 10^8\,\mathrm{Hz}$. The two-fold two-magnon term due to terrace step-edges is $\Gamma_2^{\perp\mathrm{step}} = 1.1(2) \times 10^8\,\mathrm{Hz}$, and the four-fold two-magnon due to 45°-rotated crystalline defects is $\Gamma_4^{\langle 110\rangle} = 0.4(1) \times 10^8\,\mathrm{Hz}$. These findings suggest a modification of the LSMO surface due to Pt deposition and impact the two-fold and four-fold two-magnon scattering.

The FMR linewidth of the Pt/LSMO film versus frequency exhibits multiple peaks, as shown in Fig. 3.6(a), that are are absent for the bare LSMO film in Fig. 3.5(b). Near the frequency values marked as A and B in Fig. 3.6(a), the FMR absorption profile is significantly distorted as shown in Fig. 3.6(b,c). Previously, a similar effect was reported for permalloy (Py) films with a periodic array of stripe-like defects. For Py, the peaks in the linewidth were found

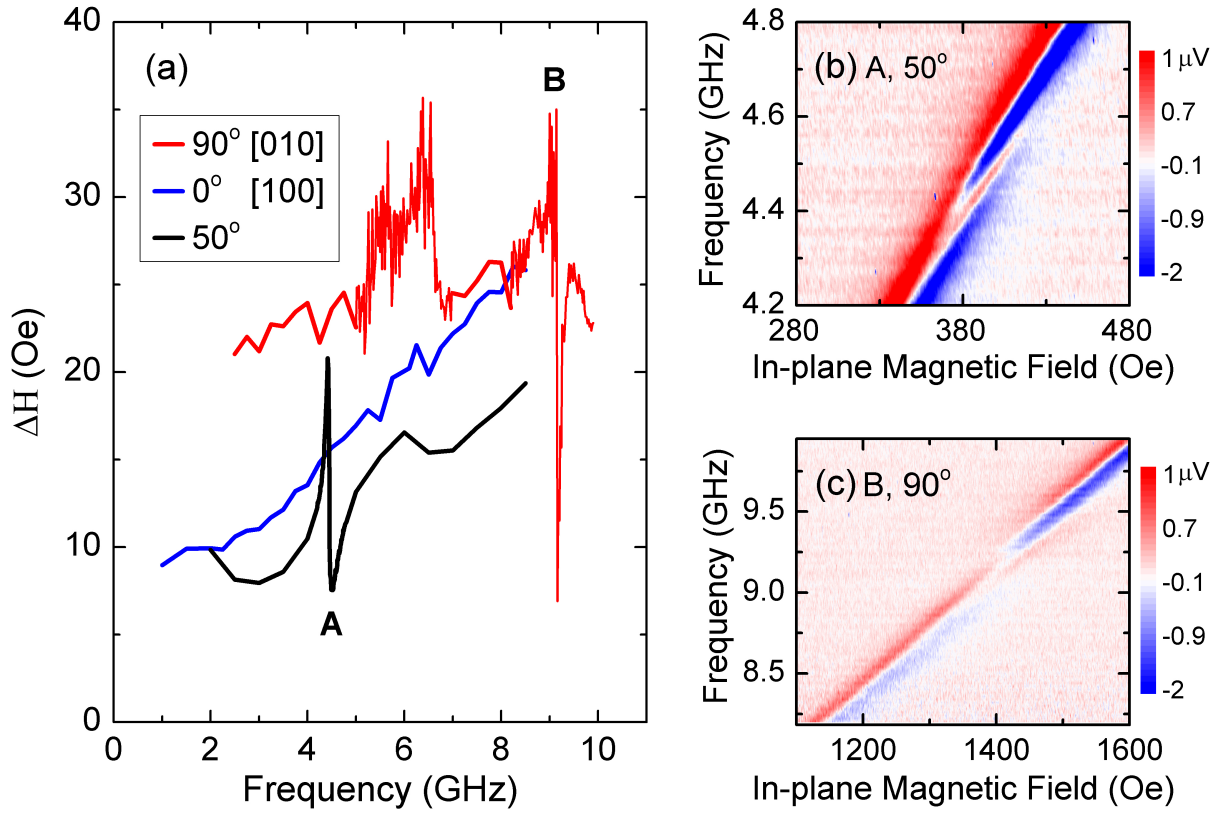

Figure 3.6: **Pt(5 nm)/LSMO(30 nm) bilayer.** (a) Frequency-dependent FMR linewidth for three values of ϕ_H. Multiple peaks seen in the FMR linewidth as a function of frequency are due to distortions of the FMR absorption profile evident in (b) and (c): color plots of the measured FMR signal versus frequency and magnetic field near frequencies marked A and B in (a).

to disappear when the film was magnetized parallel to the stripe-like defects [74, 77]. The absence of the peaks in our linewidth data for magnetization along the [100] axis in Fig. 3.6(a) suggests that the Pt/LSMO bilayer films develop stripe-like magnetic defects oriented along this axis.

3.3.3 Spin Pumping

Another important effect of the Pt layer is the increase of the Gilbert damping constant due to spin pumping, a process in which spin angular momentum is dynamically injected

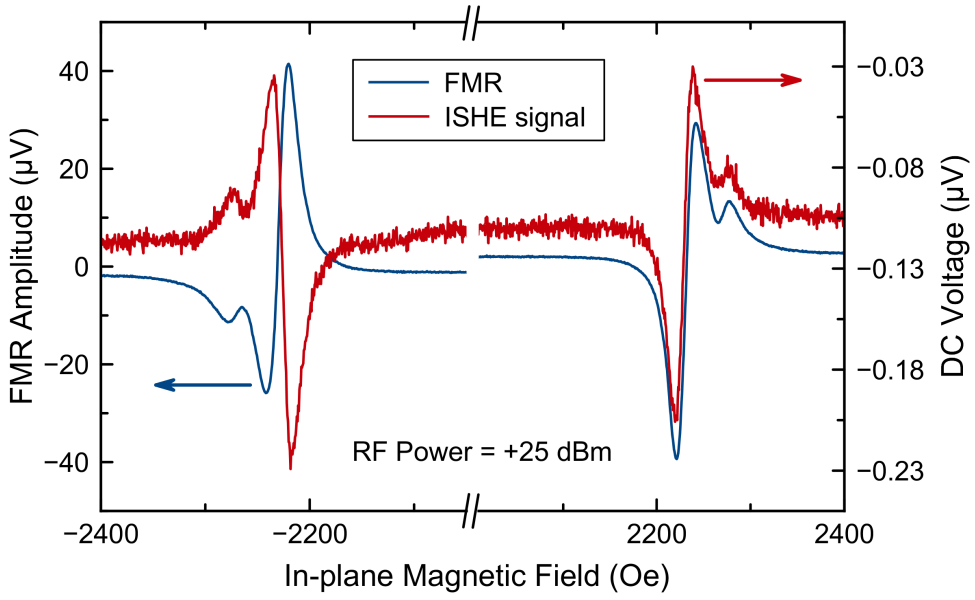

Figure 3.7: Field-modulated ISHE signal (red) and the corresponding FMR signal (blue) of Pt(9 nm)/LSMO(20 nm) film measured at 12 GHz and +25 dBm RF power applied to the CPW.

from the LSMO into the adjacent Pt layer [35, 37]. I fit the frequency- and angle-dependent linewidth data for the Pt/LSMO bilayer to quantify the Gilbert constant. In this fitting procedure, I omit the linewidth data in the frequency intervals that exhibit peaks (such as frequencies marked as A and B in Fig. 3.6). The estimated the Gilbert constant is $\alpha_{\mathrm{Pt/LSMO}} \approx 2.9(5) \times 10^{-3}$, which is $\sim 50\%$ higher than the value of the bare LSMO film but still lower than a typical Py film system.

The effective interfacial spin mixing conductance $g_{\mathrm{eff}}^{\uparrow\downarrow}$ can be determined [31, 35, 36, 39] from:

$$g_{\mathrm{eff}}^{\uparrow\downarrow} = \frac{4\pi M_{\mathrm{s}}\, t_{\mathrm{LSMO}}}{g\mu_{\mathrm{B}}}(\alpha_{\mathrm{Pt/LSMO}} - \alpha_{\mathrm{LSMO}}) \tag{3.4}$$

For the 30 nm thick film, $t_{\mathrm{LSMO}} = 30 \times 10^{-7}$ cm with $M_{\mathrm{s}} \approx 265\,\mathrm{emu/cm^3}$, I estimate $g_{\mathrm{eff}}^{\uparrow\downarrow} \approx 0.55 \times 10^{15}\,\mathrm{cm^{-2}}$. This number is comparable to the mixing conductance of Pt/Py films ($2.1 \times 10^{15}\,\mathrm{cm^{-2}}$) [31, 39] that reflects significant spin transport across the Pt/LSMO interface despite of the *ex situ* deposition of Pt.

For direct confirmation of the spin pumping process, I measure direct voltage induced in the Pt film via the inverse spin Hall effect (ISHE) [38]. I measure the ISHE voltage in Pt/LSMO bilayer in the direction perpendicular to the bias magnetic field at the drive frequency of 12 GHz, see section 2.1.2 for more details. As shown in Fig. 3.7, the ISHE voltage lineshape closely tracks that of the absorptive FMR signal and changes sign upon reversal of the magnetic field polarity, as expected for an ISHE signal.

3.4 Conclusion

In conclusion, I measured room-temperature magnetic anisotropy and damping in epitaxial LSMO films and Pt/LSMO bilayers grown on STO(001) substrates. I find significant uniaxial magnetic anisotropy, weak magnetocrystalline anisotropy, and strong negative perpendicular magnetic anisotropy that remain unaffected by the Pt cap. The easy axis of the dominant uniaxial magnetic anisotropy is parallel to the [010] crystallographic axis. Both LSMO and Pt/LSMO systems exhibit significant anisotropic magnetic damping with four-fold and two-fold symmetry components which are attributed to arise from two-magnon scattering. The four-fold component is aligned with the in-plane principal crystallographic axes and can be attributed to two-magnon scattering on crystalline defects. The symmetry axis of the two-fold two-magnon is parallel to the [010] crystallographic axis, and its origin remains unexplained. I find that a Pt capping layer enhances the anisotropic two-magnon scattering and increases Gilbert damping in Pt/LSMO system. I attribute the Gilbert damping enhancement to spin current flow across the Pt/LSMO interface induced by spin pumping. The relatively high spin mixing conductance and the very low Gilbert damping (comparable with the best-reported values of other metallic ferromagnets) are found, which make Pt/LSMO an attractive system for spintronic applications such as spin Hall memories [26] and oscillators [27, 54, 56, 78, 79]. Lastly, these results indicate that LSMO is a promising building block

for all-oxide perovskite-based spintronics devices.

Chapter 4

Giant Resonant Nonlinear Damping in Nanomagnets

The theoretical content of this chapter are adapted from work of my collaborators: Igor Barsukov, Alejandro A. Jara, Rodrigo E. Arias, and Boris A. Ivanov.

4.1 Introduction

Magnetic damping is a key parameter determining the speed and energy efficiency of magnetic nanodevices such as spin torque memory and oscillators. Here we show that nonlinear damping due to resonant three-magnon scattering gives rise to unusual magneto-dynamic phenomena in nanoscale ferromagnets. First, a spin wave mode resonance can exhibit a minimum at the resonance frequency instead of the maximum observed in the linear regime. Second, spin torque normally acting as antidamping can strongly enhance the damping of a spin wave undergoing resonant three-magnon scattering. We present a theory that explains these counterintuitive phenomena. Our work advances understanding of magnetic dynamics

in nanoscale ferromagnets and spin torque devices.

Nonlinear interactions among spin wave eigenmodes of a ferromagnet give rise to a number of spectacular magneto-dynamic phenomena such as Suhl instability of the uniform precession of magnetization [80, 81], spin wave self-focusing [82] and magnetic soliton formation [83, 84]. In bulk ferromagnets, nonlinear interactions generally couple each spin wave eigenmode to a continuum of other modes via energy- and momentum-conserving multi-magnon scattering [80]. This kinematically allowed scattering limits the amplitude of spin wave modes achievable in bulk ferromagnets to relatively small values. In nanoscale ferromagnets, geometric confinement discretizes the spin wave spectrum and thereby eliminates the kinematically allowed multi-magnon scattering. This suppression of nonlinear scattering enables persistent excitation of spin waves with very large amplitudes [85] as observed in nanomagnet-based spin torque oscillators [78, 86]. However, tunability of the spin wave spectrum by external magnetic field can be used to restore the energy-conserving scattering at a particular (resonant) field value [87].

Here we show that the effect of multi-magnon scattering on magnetization dynamics in nanomagnets is qualitatively different from that in bulk ferromagnets and requires a new theoretical framework for its description. We observe that spectral lineshape of a spin wave resonance undergoing three-magnon scattering can exhibit a minimum at the resonance frequency in sharp contrast to the amplitude maximum seen in the linear resonance regime. This unusual behavior arises because the damping parameter of a spin wave ceases to be frequency-independent and itself becomes a resonant function of the excitation frequency. We also demonstrate that such resonant nonlinear damping dramatically alters the response of a nanomagnet to spin torque. While commonly spin current polarized opposite to the direction of magnetization acts as negative damping [78], such current can increase the damping of a spin wave mode undergoing nonlinear resonant scattering. This counterintuitive effect is expected to have significant impact on the operation of spin torque based memory [26],

oscillators [56, 78, 88, 89, 90, 91] and microwave detectors [92, 93, 94].

4.2 MTJ Devices and Experimental Setup

We study nonlinear spin wave dynamics in nanoscale elliptical magnetic tunnel junctions (MTJs) that consist of a CoFeB free layer (FL), an MgO tunnel barrier, and a synthetic antiferromagnet (SAF) pinned layer (see Ref. [44] for the MTJ structure and fabrication details). Spectral properties of the FL spin wave modes are studied in a variety of MTJs with both in-plane and perpendicular-to-plane equilibrium orientations of the FL and SAF magnetization. We observe strong resonant nonlinear damping in both the in-plane and the perpendicular MTJs, which points to universality of the effect.

We employ spin-torque ferromagnetic resonance (ST-FMR) to measure magnetic damping of the FL spin wave modes. In this technique, a microwave drive current $I_{\rm ac}\cos(2\pi ft)$ applied to the MTJ excites oscillations of magnetization at the drive frequency f. The resulting resistance oscillations $R_{\rm ac}\cos(2\pi ft+\phi)$ of the MTJ at the drive frequency mix with the drive current and generate a direct voltage $V_{\rm mix}$. Peaks in ST-FMR spectra $V_{\rm mix}(f)$ arise from resonant excitation of spin wave eigenmodes of the MTJ [3, 32, 39, 47, 95, 96, 97]. To improve signal-to-noise ratio, the magnitude of external magnetic field H applied parallel to the free layer magnetization is modulated, and a field-derivative signal $\tilde{V}_{\rm mix}(f) = {\rm d}V_{\rm mix}(f)/{\rm d}H$ is measured via the lock-in detection technique [44]. $V_{\rm mix}(f)$ can then be obtained via numerical integration of $\tilde{V}_{\rm mix}(f)$ with respect to H.

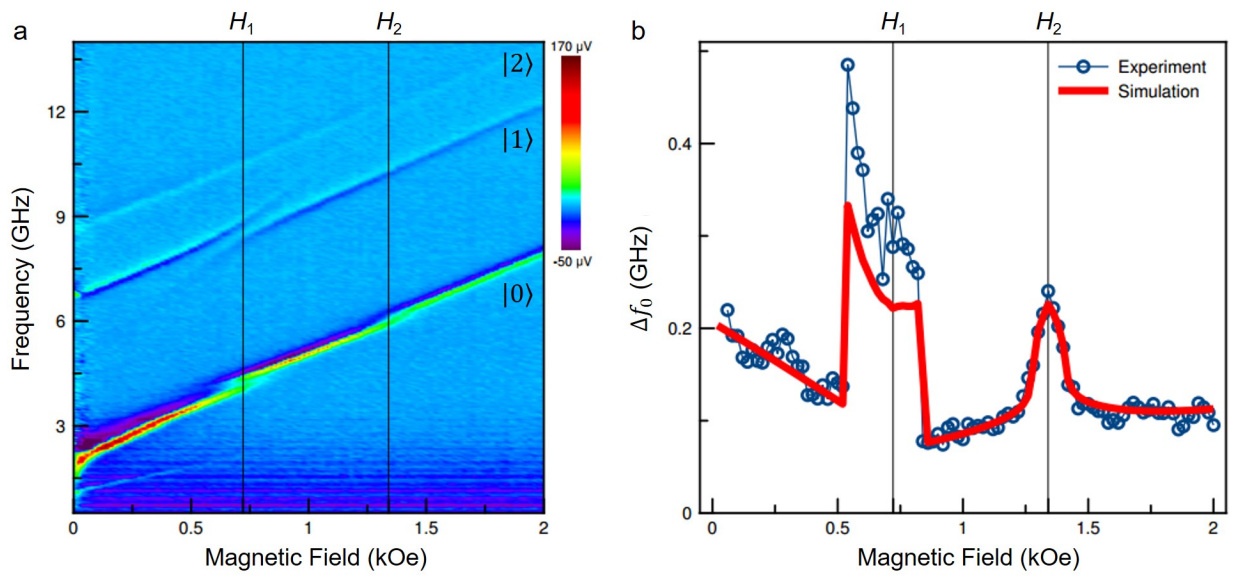

Figure 4.1: **Spin wave spectra in a nanoscale MTJ.** (a) Normalized ST-FMR spectra $\tilde{V}_{\rm mix}(f)/\tilde{V}_{\rm mix}^{\rm max}$ of spin wave eigenmodes in a perpendicular MTJ device (Sample 1) measured as a function of out-of-plane magnetic field. Resonance peaks arising from three low frequency modes of the MTJ free layer $|0\rangle$, $|1\rangle$, and $|2\rangle$ are observed. (b) Spectral linewidth of the quasi-uniform $|0\rangle$ spin wave mode as a function of out-of-plane magnetic field. Strong linewidth enhancement is observed in the resonant three-magnon regime at H_1 and H_2.

4.3 Spin wave Spectroscopy

Figure 4.1(a) shows ST-FMR spectra $\tilde{V}_{\rm mix}(f)$ measured as a function of out-of-plane magnetic field H for a $52\,\text{nm} \times 62\,\text{nm}$ perpendicular MTJ device (Sample 1). Three spin wave eigenmodes with nearly linear frequency-field relation $f_n(H)$ are clearly visible in the spectra. Micromagnetic simulations, not shown here, reveal that these modes are three lowest frequency spin wave eigenmodes of the FL. The lowest frequency (quasi-uniform) mode $|0\rangle$ is nodeless and has spatially uniform phase. Each of the two higher-order modes $|n\rangle$ $(n = 1, 2)$ has a single node at the FL center that is either perpendicular $(n = 1)$ or parallel $(n = 2)$ to the ellipse long axis.

The spectral linewidth of the resonances in Fig. 4.1(a) can be used for evaluation of the mode damping. The quasi-uniform mode resonance visibly broadens at two magnetic field values:

$H_1 = 0.74\,\mathrm{kOe}$ ($4\,\mathrm{GHz}$) and $H_2 = 1.34\,\mathrm{kOe}$ ($6\,\mathrm{GHz}$). Near H_1, the mode $|1\rangle$ resonance broadens and exhibits splitting, same behavior is observed for the mode $|2\rangle$ at H_2. At these fields, the higher-order mode frequency is twice that of the quasi-uniform mode $f_n = 2f_0$. This shows that three-magnon confluence [87, 98, 99, 100, 101] is the mechanism of the damping increase: two magnons of the quasi-uniform mode $|0\rangle$ merge into a single magnon of the higher-order mode $|n\rangle$.

The most striking feature of the quasi-uniform mode resonance near H_1 is its split-peak shape with a local minimum at the resonance frequency. Such a lineshape cannot be fit by the standard Lorentzian curve with symmetric and antisymmetric components [44]. We therefore use a double-peak fitting function to quantify the effective linewidth Δf_0 of the resonance profile, see below. For applied fields sufficiently far from H_1, the ST-FMR curve recovers its single-peak shape and Δf_0 is determined as half width of the standard Lorentzian fitting function [44]. Figure 4.1(b) shows Δf_0 as a function of H and demonstrates a large increase of the linewidth near the fields of the resonant three-magnon regime H_1 and H_2. The stepwise increase of Δf_0 near H_1 is a result of the ST-FMR curve transition between the split-peak and single-peak shapes. For fields near H_2, the resonance profile broadens but never develops a split-peak lineshape. As a result, $\Delta f_0(H)$ is a smooth function in the vicinity of H_2.

Linewidth evaluation. In order to quantify the linewidth of the unusual split-peak spin wave resonance profile of experimental data, we introduce a fitting function that is a sum of two Lorentzian curves with different central frequencies separated by δf. The half width of the resonance profile Δf_0 is then defined as the average of the half widths of the two Lorentzians plus $\delta f/2$. In the case of fold-over, the linewidth is determined as a half-width at the half-maximum of the resonance profile for the calculated spectra using a solutions of maximal mode amplitude.

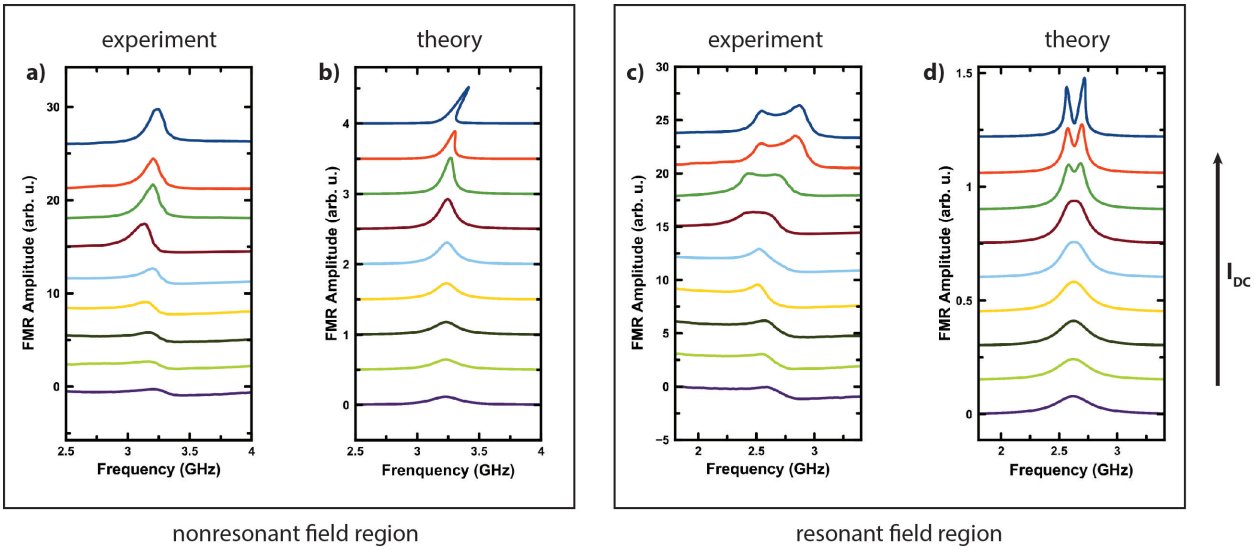

Figure 4.2: **Effect of spin torque on spin wave resonance lineshape.** (a, b) Spin wave resonance lineshapes off the resonant three-magnon regime at $H > H_1$. (c, d) Spin wave resonance lineshapes in the resonant three-magnon regime at $H = H_1$ for different values of direct bias current $I_{\rm dc}$. **a, c** measured ST-FMR spectra (Sample 2); **b, d** numerical solutions of Eqn. (4.3) and (4.4).

4.4 Effect of Spin torque

In MTJs, direct bias current $I_{\rm dc}$ applied across the junction exerts spin torque on the FL magnetization, acting as antidamping for $I_{\rm dc} > 0$ and as positive damping for $I_{\rm dc} < 0$ [3, 102]. The antidamping spin torque increases the amplitude of the FL spin wave modes [3, 103] and decreases their spectral linewidth [104]. Therefore, we can employ spin torque from $I_{\rm dc}$ to control the amplitude of spin wave eignmodes excited in ST-FMR measurements, and thereby study the crossover between linear and non-linear regimes of spin wave resonance.

Figure 4.2 shows the dependence of ST-FMR resonance curve of the $|0\rangle$ mode on $I_{\rm dc}$ for a $50\,\text{nm} \times 110\,\text{nm}$ elliptical in-plane MTJ (Sample 2). For in-plane magnetic field values far from the three-magnon resonance fields H_n, the amplitude of ST-FMR resonance curve $V_{\rm mix}(f)$ shown in Fig. 4.2(a) monotonically increases with increasing antidamping spin torque, as expected. At $H = H_1$, the antidamping spin torque has a radically different and rather surprising effect on the resonance curve. As illustrated in Fig. 4.2(c), increasing

antidamping spin torque first broadens the resonance at $H = H_1$ and then transforms a single-peak resonance lineshape into a split-peak lineshape with a local minimum at the resonance frequency f_0. The data in Fig. 4.2 demonstrate that the unusual split-peak lineshape of the resonance is only observed when (i) the three-magnon scattering of the quasi-uniform mode is allowed by the conservation of energy and (ii) the amplitude of the mode is sufficiently high. This proves that the observed effect is resonant and nonlinear in nature.

Figure. 4.1(c) reveals that antidamping spin torque can increase the spectral linewidth and the effective damping of the quasi-uniform spin mode if the mode undergoes resonant three-magnon scattering. Figure 4.3 further illustrates this counter-intuitive effect of spin-torque on the spectral linewidth. It shows the linewidth of the quasi-uniform mode of a 50 nm $\times$110 nm in-plane elliptical MTJ (Sample 3) measured as a function of bias current. In Fig. 4.3, blue symbols show the linewidth measured at an in-plane magnetic field sufficiently far from the three-magnon resonance fields H_n. At this field, the expected quasi-linear dependence of the linewidth on $I_{\rm dc}$ is observed for currents well below the critical current $I_{\rm c}$ for the excitation of auto-oscillatory magnetic dynamics. Near $I_{\rm c}$, the linewidth increases due to a combination of the fold-over effect [105, 106, 107] and thermally activated switching between the large- and small-amplitude oscillatory states of the fold-over regime [3]. The red symbols in Fig. 4.3 show the linewidth measured in the resonant three-magnon regime at $H = H_1$. In contrast to the non-resonant regime, the linewidth increases with increasing $|I_{\rm dc}|$ for both current polarities. Furthermore, the maximum linewidth is observed for the antidamping current polarity.

4.5 Theoretical Model

Nonlinear interactions among spin waves in a bulk ferromagnet with a continuous spin wave spectrum can lead to broadening of the spin wave resonances [80, 108, 109, 110]. For example,

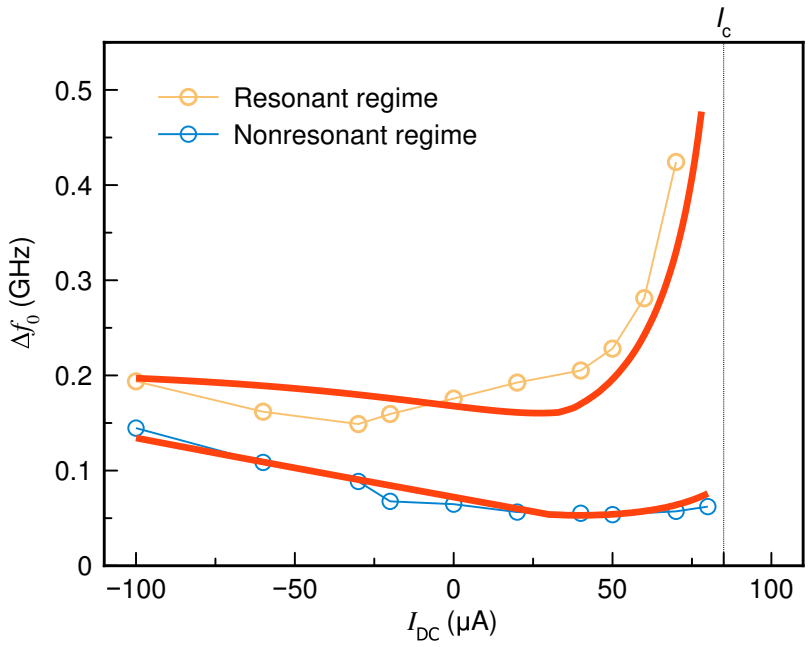

Figure 4.3: **Effect of spin torque on linewidth.** Linewidth of the quasi-uniform spin wave mode (Δf_0) as a function of the applied direct bias current (Sample 3): (i) in the non-resonant regime $H \neq H_1$ and (ii) in the resonant three-magnon regime $H = H_1$. Lines are numerical fits using Eqn. (4.3) and (4.4).

three- and four-magnon scattering of the uniform mode of precession into a continuum of degenerate spin wave eigenmodes gives rise to nonlinear enhancement of the uniform mode damping. However, these processes lead to a simple line broadening and cannot explain the observed split-peak lineshape of the resonance. Therefore, the description of nonlinear spin wave resonance in the nanoscale ferromagnet geometry requires a new theoretical framework. To derive the theory of resonant nonlinear damping in a nanomagnet, we start with a model Hamiltonian that explicitly takes into account resonant nonlinear scattering between the quasi-uniform mode and a higher-order spin wave mode (in reduced units with $\hbar \equiv 1$):

$$\begin{aligned} \mathcal{H} = \omega_0 a^\dagger a + \omega_n b^\dagger b + \frac{\Psi_0}{2} a^\dagger a^\dagger a a + \frac{\Psi_n}{2} b^\dagger b^\dagger b b \\ + (\psi_n a a b^\dagger + \psi_n^* a^\dagger a^\dagger b) \\ + \zeta \left\{ \exp(-i\,\omega t) a^\dagger + \exp(i\,\omega t) a \right\} \end{aligned} \tag{4.1}$$

where $a^\dagger$, a and $b^\dagger$, b are the magnon creation and annihilation operators for the quasi-uniform mode $|0\rangle$ with frequency ω_0 and for the higher-order spin-wave mode $|n\rangle$ mode with frequency ω_n, respectively. The nonlinear mode coupling term proportional to the coupling strength parameter ψ_n describes the annihilation of two $|0\rangle$ magnons and creation of one $|n\rangle$ magnon, as well as the inverse process. The Hamiltonian is written in the resonant approximation, where small non-resonant terms such as aab, $aaa^\dagger$ are neglected. The terms proportional to Ψ_0 and Ψ_n describe the intrinsic nonlinear frequency shifts [111] of the modes $|0\rangle$ and $|n\rangle$. The last term describes the excitation of the quasi-uniform mode by an external ac drive with the amplitude ζ and frequency ω.

We further define a dissipation function $\mathcal{Q}$, where α_0 and α_n are the intrinsic linear damping parameters of the modes $|0\rangle$ and $|n\rangle$ [112, 113, 114]:

$$\mathcal{Q} = \frac{\mathrm{d}a^\dagger}{\mathrm{d}t}\frac{\mathrm{d}a}{\mathrm{d}t}(\alpha_0 + \eta_0 a^\dagger a) + \frac{\mathrm{d}b^\dagger}{\mathrm{d}t}\frac{\mathrm{d}b}{\mathrm{d}t}(\alpha_n + \eta_n b^\dagger b) \tag{4.2}$$

For generality, Eqn. (4.2) includes intrinsic nonlinear damping [115] of the modes $|0\rangle$ and $|n\rangle$ described by the nonlinearity parameters η_0 and η_n. However, our analysis below reveals that the split-peak resonance lineshape is predicted by our theory even if η_0 and η_n are set equal to zero.

Equations describing the nonlinear dynamics of the two coupled spin wave modes of the system follow from Eqn. (4.1) and Eqn. (4.2):

$$i\frac{\mathrm{d}a}{\mathrm{d}t} = \frac{\partial\mathcal{H}}{\partial a^\dagger} + \frac{\partial\mathcal{Q}}{\partial(\mathrm{d}a^\dagger/\mathrm{d}t)} \tag{4.3}$$

$$i\frac{\mathrm{d}b}{\mathrm{d}t} = \frac{\partial\mathcal{H}}{\partial b^\dagger} + \frac{\partial\mathcal{Q}}{\partial(\mathrm{d}b^\dagger/\mathrm{d}t)} \tag{4.4}$$

These equations have a periodic solution $a = \bar{a}\exp(i\,\omega t)$ and $b = \bar{b}\exp(i\,2\omega t)$, where $\bar{a}$, $\bar{b}$

are the complex spin wave mode amplitudes. For such a periodic solution, Eqn. (4.3) and (4.4) are reduced to a set of two nonlinear algebraic equations for absolute values of the spin wave mode amplitudes $|\bar{a}|$ and $|\bar{b}|$, which can be solved numerically. Since the ST-FMR signal is proportional to $|\bar{a}|$ [44], the calculated $|\bar{a}|(\omega)$ function can be directly compared to the measured ST-FMR resonance lineshape.

We employ the numerical solution of Eqn. (4.3) and (4.4) to fit the field dependence of the quasi-uniform mode linewidth in Fig. 4.1(b). In this fitting procedure, the resonance lineshape $|\bar{a}|(\omega)$ is calculated from Eqn. (4.3) and (4.4), and its spectral linewidth $\Delta\omega_0$ is found numerically. The resonance frequencies ω_0 and ω_n are directly determined from the ST-FMR data in Fig. 4.1(a). The intrinsic damping parameters α_0 and α_n near H_1 and H_2 are found from linear interpolations of the ST-FMR linewidths Δf_0 and Δf_n measured at fields far from H_1 and H_2. We find that $\Delta\omega_0$ weakly depends on the nonlinearity parameters Ψ and η, and thus these parameters are set to zero. We also find that the calculated linewidth $\Delta\omega_0$ depends on the product of the drive amplitude ζ and mode coupling strength ψ_n, but is nearly insensitive to the individual values of ζ and ψ_n as long as $\zeta \cdot \psi_n = \text{const}$. Therefore, we use $\zeta \cdot \psi_n$ as a single fitting parameter in this fitting procedure. Solid line in Fig. 4.1(b) shows the calculated field dependence of the quasi-uniform mode linewidth on magnetic field. The agreement of this single-parameter fit with the experiment is excellent.

Figures 4.2(b,d) illustrate that Eqn. (4.3) and (4.4) not only describe the field dependence of ST-FMR linewidth but also qualitatively reproduce the spectral lineshapes of the measured ST-FMR resonances as well as the effect of the antidamping spin torque on the lineshapes. Figure 4.2(b) shows the dependence of the calculated lineshape $|\bar{a}|(\omega)$ on antidamping spin torque for a magnetic field H far from the three-magnon resonance fields H_n. At this non-resonant field, increasing antidamping spin torque induces the fold-over of the resonance curve [105] without resonance peak splitting. The dependence of $|\bar{a}|(\omega)$ on antidamping spin torque for $H = H_1$ is shown in Fig. 4.2(d). At this field, the resonance peak in $|\bar{a}|(\omega)$

first broadens with increasing antidamping spin torque and then splits, which qualitatively reproduces the experimental ST-FMR data in Fig. 4.2(c). Our calculations reveal that while the nonlinearity parameters Ψ_0, η_0, Ψ_n and η_n have little effect on the linewidth $\Delta\omega_0$, they modify the lineshape of the resonance. Given that the nonlinearity parameter values are not well known for the systems studied here, we do not attempt to quantitatively fit the measured ST-FMR lineshapes using a five-parameter fit.

Equations (4.3) and (4.4) also quantitatively explain the observed dependence of the quasi-uniform mode linewidth $\Delta\omega_0$ on direct bias current $I_{\rm dc}$. Assuming antidamping spin torque linear in bias current [104, 116, 117]: $\alpha_0 \to \alpha_0(1 - I_{\rm dc}/I_{\rm c}^{|0\rangle})$, $\alpha_n \to \alpha_n(1 - I_{\rm dc}/I_{\rm c}^{|n\rangle})$, where $I_{\rm c}^{|n\rangle} > I_{\rm c}^{|0\rangle}$ are the critical currents, we fit the measured bias dependence of ST-FMR linewidth in Fig. 4.3 by numerically solving Eqn. (4.3) and (4.4). The solid lines in Fig. 4.3 are the best numerical fits, where $\zeta \cdot \psi_n$ and $I_{\rm c}$ are used as independent fitting parameters. The rest of the parameters in Eqn. (4.3) and (4.4) are directly determined from the experiment following the procedure used for fitting the data in Fig. 4.1(b). Theoretical curves in Fig. 4.3 capture the main feature of the data at the three-magnon resonance field H_1 – increase of the linewidth with increasing antidamping spin torque.

4.6 Discussions

Further insight into the mechanisms of the nonlinear spin wave resonance peak splitting and broadening by antidamping spin torque can be gained by neglecting the intrinsic nonlinearities Ψ_n and η_n of the higher-order mode $|n\rangle$. Setting $\Psi_n = 0$ and $\eta_n = 0$ in Eqn. (4.3) and (4.4) allows us to reduce the equation of motion for the quasi-uniform mode amplitude $|\bar{a}|$ to the standard equation for a single-mode damped driven oscillator where a constant damping parameter α_0 is replaced by an effective frequency-dependent nonlinear damping parameter

α_0^{eff}:

$$\alpha_0^{\text{eff}} = \alpha_0 + \left[\eta_0 + \frac{4\alpha_n\psi_n^2}{(2\omega-\omega_n)^2 + 4\alpha_n^2\omega^2}\right]|\bar{a}|^2 \tag{4.5}$$

and the resonance frequency is replaced by an effective resonance frequency:

$$\omega_0^{\text{eff}} = \omega_0 + \left[\Psi_0 + \frac{2|\psi_n|^2(2\omega-\omega_n)}{(2\omega-\omega_n)^2 + 4\alpha_n^2\omega^2}\right]|\bar{a}|^2 \tag{4.6}$$

Equation (4.5) clearly shows that the damping parameter of the quasi-uniform mode itself becomes a resonant function of the drive frequency with a maximum at half the frequency of the higher order mode ($\omega = \omega_n/2$). The amplitude and the width of this resonance in $\alpha_0^{\text{eff}}(\omega)$ are determined by the damping parameter α_n of the higher-order mode $|n\rangle$. If α_n is sufficiently small, the quasi-uniform mode damping is strongly enhanced at $\omega = \omega_n/2$, which leads to a decrease of the quasi-uniform mode amplitude at this drive frequency. If the drive frequency is shifted away from $\omega_n/2$ to either higher or lower values, the damping decreases, which can result in an increase of the quasi-uniform mode amplitude $|\bar{a}|$. Therefore, the amplitude of the quasi-uniform mode $|\bar{a}|(\omega)$ can exhibit a local minimum at $\omega = \omega_n/2$. Due to its nonlinear origin, the tendency to form a local minimum in $|\bar{a}|(\omega)$ at $\omega_n/2$ is enhanced with increasing $|\bar{a}|$. Since $|\bar{a}|$ is large near the resonance frequency ω_0, tuning ω_0 to be equal to $\omega_n/2$ greatly amplifies the effect of local minimum formation in $|\bar{a}|(\omega)$. This qualitative argument based on Eqn. (4.5) explains the data in Fig. 4.2 – the split-peak nonlinear resonance of the quasi-uniform mode is only observed when external magnetic field tunes the spin wave eigenmode frequencies to the three-magnon resonance condition $2\omega_0 = \omega_n$. Whether the unusual split-peak resonance with a local minimum of amplitude at the resonance frequency is realized in a given nanomagnet depends on the numerical values of the intrinsic damping parameters of the modes involved in the three-magnon process and the magnitude of coupling between the modes ψ_n. It is clear from Eqn. (4.5) that small values of the damping parameters and large three-magnon coupling constant ψ_n favor the the split-peak resonance formation.

Equation (4.6) reveals that the nonlinear frequency shift of the quasi-uniform mode is also a resonant function of the drive frequency. In contrast to the nonlinear damping resonance described by Eqn. (4.5), the frequency shift resonance is an anti-symmetric function of $\omega - \omega_n/2$. The nonlinear shift is negative for $\omega < \omega_n/2$ and thus causes a fold-over towards lower frequencies while it is positive for $\omega > \omega_n/2$ causing fold-over towards higher frequencies. At the center of the resonance profile, the three-magnon process induces no frequency shift. This double-sided fold-over also contributes to the formation of the split-peak lineshape of the resonance shown in Figs. 4.2(c,d) and to the linewidth broadening. As with the nonlinear damping resonance, the anti-symmetric nonlinear frequency shift and the double-sided fold-over become greatly amplified when the spin wave mode frequencies are tuned to the three-magnon resonance $2\omega_0 = \omega_n$. In the nonresonant regime $2\omega_0 > \omega_n$, Eqn. 4.6 explains the blue frequency shift observed in Fig. 4.2(b).

Equations (4.5) and (4.6) also shed light on the origin of the quasi-uniform mode line broadening by the antidamping spin torque. The antidamping spin torque increases the quasi-uniform mode amplitude $|\bar{a}|$ via transfer of angular momentum from spin current to the mode [118]. Since the nonlinear damping and the nonlinear frequency shift are both proportional to $|\bar{a}|^2$ and both contribute to the line broadening, the antidamping spin torque can give rise to the line broadening. Equation (4.5) reveals two competing effects of the antidamping spin torque on the quasi-uniform mode damping parameter α_0^{eff}: spin torque from I_{dc} decreases the linear component of the damping parameter $\alpha_0 \rightarrow \alpha_0(1 - I_{\text{dc}}/I_{\text{c}}^{|0\rangle})$ and increases the nonlinear component via increasing $|\bar{a}|$. Whether the antidamping spin torque decreases or increases the spectral linewidth of the mode depends on the system parameters. Our numerical solution of Eqn. (4.3) and (4.4) shown in Fig. 4.3 clearly demonstrates that the antidamping spin torque can strongly increase the linewidth of the quasi-uniform mode when the three-magnon resonance condition $2\omega_0 = \omega_n$ is satisfied.

The key requirement for observation of the resonant nonlinear damping is discreteness of the

magnon spectrum imposed by geometric confinement in the nanoscale ferromagnet geometry. The split-peak nonlinear resonance discovered in this work cannot be realized in bulk ferromagnets because the three-magnon resonance condition in bulk is not only valid at the uniform mode frequency ω_0 but also at other frequencies near ω_0. Owing to the magnon spectrum continuity in bulk, shifting the excitation frequency away from ω_0 does not destroy the three-magnon scattering of the uniform mode – it simply shifts it from one group of magnons to another [80, 98]. Therefore, the amplitude of the uniform mode does not increase when the drive frequency is shifted away from ω_0 and thus the split-peak resonance is not realized.

4.7 Conclusion

Our measurements demonstrate that magnetic damping of spin wave modes in a nanoscale ferromagnet has a strong nonlinear component of resonant character that appears at a discrete set of magnetic fields corresponding to resonant three-magnon scattering. This strong resonant nonlinearity can give rise to unusual spin wave resonance profile with a local minimum at the resonance frequency in sharp contrast to the properties of the linear and nonlinear spin wave resonances in bulk ferromagnets. The resonant nonlinearity has a profound effect on the response of the nanomagnet to spin torque. Antidamping spin torque that reduces the quasi-uniform spin wave mode damping at magnetic fields far from the resonant three-magnon regime, can strongly enhance the damping in the resonant regime. This inversion of the effect of spin torque on magnetization dynamics by the resonant nonlinearity is expected to have significant impact on the performance of nanoscale spin torque devices such as magnetic memory and spin torque oscillators.

Chapter 5

Parametric Resonance of Magnetization Excited by Electric Field

The contents of this chapter are adapted from work originally published as *Nano Lett.*, 17(1), 572-577 (2017). The theory of parametric resonance threshold is developed by our collaborators: Roman Verba, Vasil Tiberkevich, and Andrei N. Slavin.

5.1 Introduction

A prominent manifestation of the magneto-electric coupling in magnetic films and heterostructures is modification of magnetic anisotropy by electric field [9, 119, 120]. This recently discovered effect takes place at the interface between a ferromagnetic metal (e.g. Fe) and a nonmagnetic insulator (e.g. MgO) [9] and originates from different rates of filling of d-like electron bands in response to electric field applied perpendicular to the interface [12].

Since electrons in different bands contribute unequally to the uniaxial perpendicular magnetic anisotropy (PMA) at the interface, electric field can be used to modulate PMA. This voltage-controlled magnetic anisotropy (VCMA) is promising for energy-efficient manipulation of magnetization [121, 122, 123] because, unlike spin torque (ST), VCMA does not rely on high electric current density resulting in large Ohmic losses. In this work, I employ VCMA modulation at microwave frequencies in order to excite parametric resonance of magnetization in a nanomagnet [124, 125, 126].

Parametric excitation of magnetization has two important advantages over direct excitation by external magnetic field with a frequency at f_{SW}. First, parametric drive efficiently couples not only to the uniform precession of magnetization but also to spin wave eigenmodes [15]. This allows excitation of short wavelength spin waves by simply choosing the parametric drive frequency to be twice the desired spin wave frequency. Second, parametric pumping can be used for frequency-selective amplification of spin waves [16] and for phase error correction [17]. All these properties of parametric pumping form a highly desirable set of tools for the nascent field of nanomagnonics [18, 17]. However, parametric excitation of spin waves by microwave magnetic field in metallic ferromagnets is not energy-efficient because of the relatively high threshold fields (tens of Oe) [20]. Here we show that replacing magnetic field pumping by electric field (VCMA) pumping solves this problem and allows parametric excitation of magnetic oscillations in metallic ferromagnets by a low-power microwave drive.

5.2 MTJ Devices and Experimental Setup

We demonstrate parametric excitation of magnetization in $70\,\mathrm{nm}\times150\,\mathrm{nm}$ elliptical nanoscale magnetic tunnel junctions (MTJs) schematically shown in Fig. 5.1(a). The junctions are patterned from (bottom lead)/ Ta(5)/ PtMn(15)/ SAF/ MgO(0.83)/ $Co_{20}Fe_{60}B_{20}$(1.58)/ Ta(5)/ (cap) multilayers (thicknesses in nm) deposited by magnetron sputtering. Here SAF

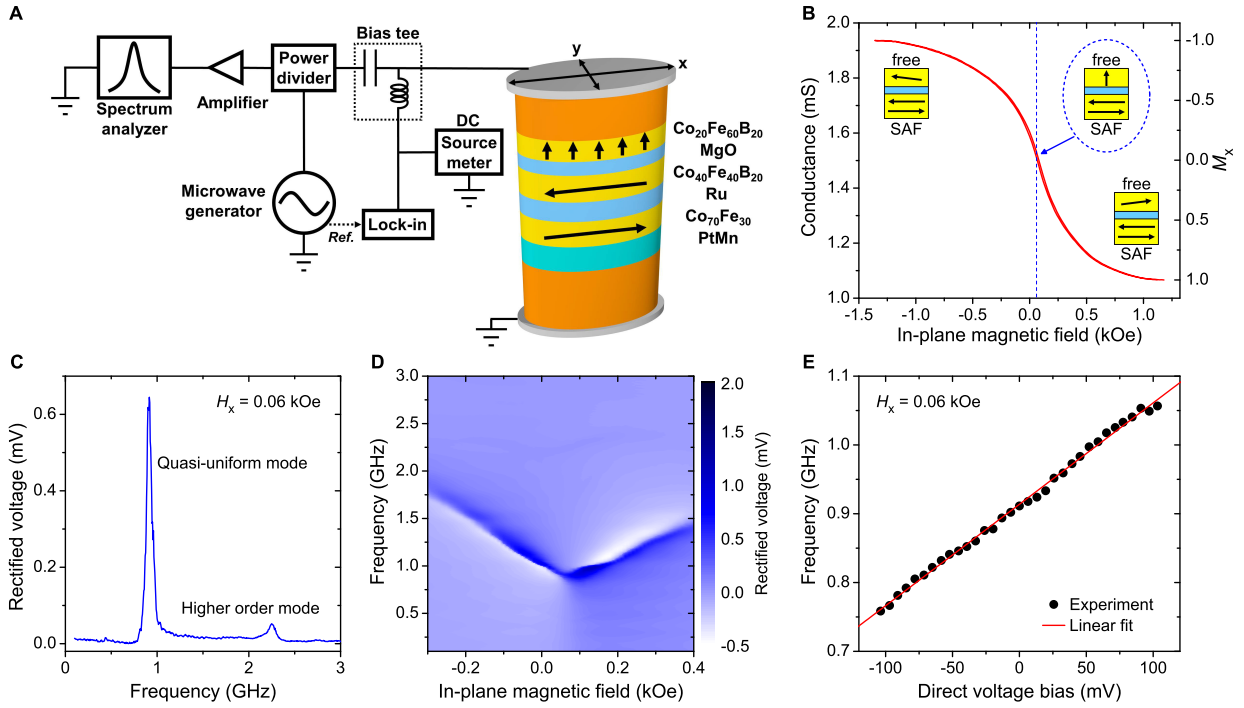

Figure 5.1: **Measurement setup and MTJ characterization.** (a) Schematic of experimental setup for DC and microwave characterization of MTJ. (b) MTJ conductance as a function of in-plane magnetic field H_{x} applied parallel to the MTJ long axis. (c) ST-FMR spectrum of the MTJ at $H_{\mathrm{x}} = 0.06\,\mathrm{kOe}$. (d) Dependence of ST-FMR spectra on H_{x}. (e) Quasi-uniform spin wave mode frequency versus direct voltage bias V_{dc} measured at $H_{\mathrm{x}} = 0.06\,\mathrm{kOe}$.

= $Co_{70}Fe_{30}$(2.3)/ Ru(0.85)/ $Co_{40}Fe_{40}B_{20}$(2.4) is the pinned synthetic antiferromagnet, which has magnetic moments lying in the plane of the sample. The equilibrium direction of the $Co_{20}Fe_{60}B_{20}$ free layer magnetization is normal to the sample plane due to interfacial PMA [92]. Prior to patterning, the multilayers are annealed for 2 hours at 300 °C in a 10 kOe in-plane magnetic field that sets the pinned layer exchange bias direction parallel to the MTJ long axis.

5.3 Characterization of MTJ Device

All measurements in this chapter are made in the setup schematically shown in Fig. 5.1(a) that allows application of DC and microwave voltages to the MTJ and measurement of DC and microwave signals generated by the MTJ. Fig. 5.1(b) shows conductance G of the MTJ measured as a function of in-plane magnetic field H_x applied parallel to the MTJ long axis. The shape of the $G(H_x)$ curve is congruent to the shape of the $M_x(H_x)$ hysteresis loop [92], where M_x is normalized projection of the free layer magnetization onto the applied field direction. The hysteresis loop and micromagnetic simulations confirm the out-of-plane easy axis of the free layer, not shown here. The center of the loop is shifted from zero field due to a residual 0.06 kOe stray field from the SAF.

We employ spin-torque ferromagnetic resonance (ST-FMR) to characterize the spectral properties of spin wave eigenmodes of the MTJ. In this technique, a small amplitude microwave drive current $GV_{ac}\sin(2\pi f_d t)$ applied to the MTJ excites oscillations of magnetization at the drive frequency f_d. The resulting resistance oscillations $R_{ac}\sin(2\pi f_d t+\phi)$ of the MTJ at the drive frequency lead to partial rectification of the microwave drive voltage V_{ac} and generate a direct voltage V_r. Peaks in ST-FMR spectra $V_r(f_d)$ arise from resonant excitation of spin wave eigenmodes of the MTJ [3, 47].

Gilbert damping. Figure 5.1(c) shows a ST-FMR spectrum of the MTJ measured at $H_x = 0.06\,\mathrm{kOe}$. Two spin wave eigenmodes are present in this spectrum with the lowest-frequency ($f_{SW} = 0.91\,\mathrm{GHz}$) mode being the quasi-uniform spin wave mode of the free layer [44]. The Gilbert damping of the free layer was estimated from the spectral linewidth of the quasi-uniform mode measured by ST-FMR technique at $H_x = 0.06\,\mathrm{kOe}$. Assuming uniaxial anisotropy, the Gilbert damping parameter is given by the ratio of half width at half maximum Δf of the ST-FMR resonance curve $V_r(f_d)$ to the quasi-uniform mode resonance frequency f_{SW} [15]:

$$\alpha = \frac{\Delta f}{f_{SW}}. \tag{5.1}$$

In Fig. 5.1(c), we find $\Delta f \approx 0.03\,\mathrm{GHz}$. By using this value of the linewidth and the measured resonance frequency $f_{SW} = 0.91\,\mathrm{GHz}$, we obtain an estimate of the free layer Gilbert damping constant $\alpha \approx 0.033$, which is typical for a CoFeB layer of this thickness [92]. Dependence of ST-FMR spectra on H_x is summarized in Fig. 5.1(d). The frequency of the quasi-uniform mode increases with increasing absolute value of the net in-plane field due to the second-order uniaxial PMA [92].

VCMA efficiency. Figure 5.1(e) shows dependence of the quasi-uniform spin wave mode frequency on direct voltage bias V_{dc} applied to the MTJ. The observed linear shift of the quasi-uniform mode resonance frequency f_{SW} with applied direct voltage V_{dc} shown in Fig. 5.1(e) arises exclusively from VCMA. The effective fields due to field-like and damping-like spin torque are perpendicular to the free layer magnetization for the perpendicular orientation of the free and the SAF magnetic moments employed in our experiment. Such perpendicular fields can only induce a quadratic shift of the quasi-uniform mode frequency. The frequency shift due to Ohmic heating is independent of the current polarity and thus is also quadratic in V_{dc} to leading order. Given the linear relation between the resonance frequency f_{SW} and the anisotropy field H_u for a uniaxial ferromagnet, the slope of the line

in Fig. 5.1(e) is

$$\frac{\gamma}{2\pi}\frac{dH_{\mathrm{u}}}{dV_{\mathrm{dc}}}, \tag{5.2}$$

where the gyromagnetic ratio γ is taken to be 176 GHz/T. The data in Fig. 5.1(e) gives VCMA efficiency $\frac{dH_{\mathrm{u}}}{dV_{\mathrm{dc}}} = 526\,\mathrm{Oe/V}$, which is typical for this material system [92].

5.4 Detection of Parametric Resonance by Microwave Emission Measurement

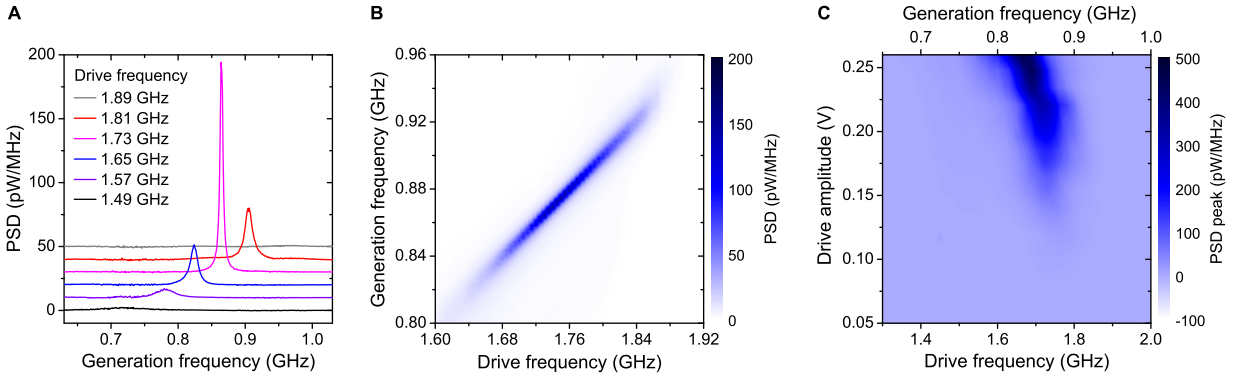

Figure 5.2: **Parametric resonance.** (a) Power spectral density (PSD) of the microwave signal emitted by the MTJ under VCMA parametric drive of $V_{\mathrm{ac}} = 0.185\,\mathrm{V}$. Curves are vertically offset for clarity and are listed in order of drive frequency. (b) Dependence of the parametrically generated emission spectra on the drive frequency for $V_{\mathrm{ac}} = 0.185\,\mathrm{V}$. (c) PSD peak plotted versus drive frequency and drive amplitude reveals typical Arnold tongue shape characteristic of parametric excitation.

We use the parallel pumping geometry to parametrically excite the free layer quasi-uniform mode [124], in which magnetization of the free layer is parallel to the oscillating PMA field H_{u}. We apply a constant 0.06 kOe in-plane magnetic field along the long axis of the ellipse to compensate the in-plane SAF stray field acting on the free layer so that its magnetization is aligned perpendicular to the sample plane. We then apply a parametric drive voltage V_{ac} to the MTJ and vary the drive frequency f_{d} about $2f_{\mathrm{SW}}$ (twice the quasi-uniform mode resonance frequency). The resulting modulation of PMA at the drive frequency due to

VCMA can parametrically excite magnetization oscillations at half the drive frequency [124], which gives rise to the MTJ resistance oscillations $R_{\rm ac}\cos(2\pi\frac{f_{\rm d}}{2}t+\phi)$. These resistance oscillations can be detected via their mixing with the microwave current $GV_{\rm ac}\cos(2\pi f_{\rm d}t)$ through the junction, which generates mixing voltage signals $V_{\rm mix}(t)$ at frequencies $f_{\rm d}/2$ and $3f_{\rm d}/2$:

$$V_{\rm mix}(t)=GV_{\rm ac}\cos(2\pi f_{\rm d}t)\cdot R_{\rm ac}\cos\left(2\pi\frac{f_{\rm d}}{2}t+\phi\right)= \\ \frac{1}{2}GV_{\rm ac}R_{\rm ac}\left[\cos\left(2\pi\frac{f_{\rm d}}{2}t-\phi\right)+\cos\left(2\pi\frac{3f_{\rm d}}{2}t+\phi\right)\right]. \tag{5.3}$$

As illustrated in Fig. 5.1(a), we amplify $V_{\rm mix}(t)$ and measure its spectrum with a microwave spectrum analyzer. Here we present power spectra of $V_{\rm mix}(t)$ measured near $f_{\rm d}/2$; similar spectra are observed near $3f_{\rm d}/2$. Figure 5.2(a) displays power spectral density (PSD) $P(f)$ of $V_{\rm mix}(t)$ measured at several fixed values of the drive frequency $f_{\rm d}$ near $2f_{\rm SW}$ and drive amplitude $V_{\rm ac}=0.185\,{\rm V}$. The maximum of each power spectrum is observed exactly at $f_{\rm d}/2$, clearly illustrating that magnetization dynamics of the free layer is excited parametrically at half the drive frequency. The linewidths of the measured spectral peaks are in the range of several MHz. This linewidth mostly arises from thermal fluctuations of the free layer magnetization (fluctuations of the phase ϕ in Eqn. 5.3). Figure 5.2(b) illustrates that parametric excitation of the quasi-uniform mode has well-pronounced resonant character: significant amplitude of the parametric oscillations is observed only in a narrow range of the drive frequencies near $2f_{\rm SW}$.

Figure 5.2(c) displays dependence of $P(f_{\rm d}/2)$ on the drive amplitude $V_{\rm ac}$ and drive frequency $f_{\rm d}$. This figure illustrates the parametric excitation efficiency and clearly demonstrates that the observed microwave emission from the sample has a threshold character in $V_{\rm ac}$. This threshold behavior is expected for parametric resonance that is excited when effective negative damping from the parametric drive exceeds the positive natural damping of the

excited mode [15]. Figure 5.2(c) also shows that the parametric resonance frequency $f_{\rm pr}$ (defined as $f_{\rm d}$ that gives maximum $P(f_{\rm d}/2)$ at a given value of $V_{\rm ac}$) shifts to lower values with increasing drive amplitude due to nonlinear frequency shift, as expected for a uniaxial ferromagnet [15]. The shape of the parametric instability region in Fig. 5.2(c) is a typical Arnold tongue of a nonlinear parametric oscillator [127].

5.4.1 Theory of Parametric Resonance Threshold

For the theoretical description of parametric resonance of the MTJ free layer we employ a single-mode approximation. We expand the free layer magnetization into static and dynamic parts: $\mathbf{M}(\mathbf{r},t) = M_{\rm s}(\boldsymbol{\mu} + c(t)\mathbf{m}(\mathbf{r}) + c^*(t)\mathbf{m}^*(\mathbf{r}))$, where $\boldsymbol{\mu}$ is the unit vector in the direction of the static magnetization, $\mathbf{m}(\mathbf{r})$ is the coordinate-dependent vector structure of the spin wave mode, and c is the dimensionless amplitude of this mode. Starting from the Landau-Lifshitz-Gilbert equation, the following nonlinear equation describing the dynamics can be derived [15, 124]:

$$\frac{\mathrm{d}c}{\mathrm{d}t} + i(\omega_{\rm SW} + \Psi|c|^2)c + \Gamma c = hV_{00}e^{i\omega_{\rm p}t}c^* + \eta(t), \tag{5.4}$$

where $\omega_{\rm SW} = 2\pi f_{\rm SW}$ is the spin wave mode angular frequency, Ψ is the nonlinear frequency shift of the mode, Γ is the damping rate of the mode, h is the effective pumping field amplitude, $\omega_{\rm p}$ is the pumping frequency, V_{00} is the efficiency of parametric interaction, and $\eta(t)$ describes thermal noise (see Ref. [128] for details). In these notations, the parametric resonance threshold field is $h_{\rm th} = \Gamma/|V_{00}|$, where $|V_{00}| = \frac{\gamma\mu_0}{2}\varepsilon$, γ is the gyromagnetic ratio taken to be 176 GHz/T, $\mu_0 = 4\pi \times 10^{-7}$ T·m/A is the permeability of vacuum, and the damping rate $\Gamma = 2\pi\Delta f = 2\pi \times 0.03$ GHz [15, 124]. Averaged ellipticity of the spin wave mode ε is given by [124]:

$$\varepsilon = \left| \frac{\langle \mathbf{m}^* \cdot \mathbf{m}^* \rangle_{\mathbf{r}}}{\langle \mathbf{m}^* \cdot (\boldsymbol{\mu} \times \mathbf{m}) \rangle_{\mathbf{r}}} \right|, \tag{5.5}$$

where $\langle ... \rangle_{\mathbf{r}}$ denotes a spatial average over the free layer volume.

We calculate the quasi-uniform mode ellipticity from the micromagnetic mode profile. This calculation gives $\varepsilon = 0.26$, which results in $h_{\rm th} = 6.5\,{\rm kA/m} = 82\,{\rm Oe}$. This gives the threshold voltage for excitation of parametric resonance $V_{\rm th} = h_{\rm th}\frac{dV_{\rm dc}}{dH_{\rm u}} = 0.156\,{\rm V}$. This micromagnetic value of $V_{\rm th}$ is significantly higher than that given by the macrospin approximation with $\varepsilon = \omega_{\rm M}|N_{\rm x} - N_{\rm y}|/(2\omega_{\rm SW})$, where $\omega_{\rm M} = \gamma\mu_0 M_{\rm s}$ (with $M_{\rm s} = 950\,{\rm kA/m}$), $N_{\rm x} = 0.014$ and $N_{\rm y} = 0.040$ are components of the free layer demagnetization tensor [129], and $\omega_{\rm SW} = 2\pi \times 0.91\,{\rm GHz}$ is the spin wave mode frequency. The higher value of ellipticity ($\varepsilon = 0.478$) in the macrospin approximation leads to a lower parametric threshold: $h_{\rm th} = 45\,{\rm Oe}$ and $V_{\rm th} = 0.085\,{\rm V}$. As expected, the experimentally measured value of the threshold voltage $V_{\rm th} = 0.136\,{\rm V}$ is much higher than that given by the macrospin approximation but it is similar to that appropriate for micromagnetic profile of the quasi-uniform mode. The 15% discrepancy between the measured and the theoretically predicted threshold could arise from deviation of the free layer shape from the ideal elliptical shape assumed in the simulations and from over-estimation of the damping parameter of the free layer.

Evaluation of the parametric resonance threshold from experiment

To determine the threshold voltage for parametric excitation $V_{\rm th}$ from the experimental data in Fig. 5.3, we fit these data to theoretical expressions of the oscillation power as a function of the drive amplitude $V_{\rm ac}$. These expressions are derived below for two limits: $V_{\rm ac} \ll V_{\rm th}$ and $V_{\rm ac} \gg V_{\rm th}$.

Below the threshold. Well below the threshold ($V_{\rm ac} \ll V_{\rm th}$), the nonlinear frequency shift in Eqn. (5.4) can be neglected and the parametric resonance frequency $f_{\rm pr}$ is equal to twice the spin wave mode frequency ($f_{\rm pr} = 2f_{\rm SW}$). In this limit, the reduced integrated power p of the spin wave mode is given by the expression below when the free layer is driven exactly

at the parametric resonance frequency $f_{\rm pr}$:

$$p = \left\langle |c|^2 \right\rangle = \frac{C_1}{\Gamma - |hV_{00}|} + \frac{C_1}{\Gamma + |hV_{00}|} = \frac{D}{(V_{\rm th} - V_{\rm ac})} + \frac{D}{(V_{\rm th} + V_{\rm ac})}, \tag{5.6}$$

where $\langle ... \rangle$ denotes a thermal average. In deriving this expression, we assumed white thermal noise: $\langle \eta(t)\eta(\tau) \rangle = C_2\delta(t-\tau)$ and $\langle \eta(t)\eta^*(\tau) \rangle = C_1\delta(t-\tau)$, where C_1, C_2 and $D = C_1 V_{\rm th}/\Gamma$ are constants. Here we also employed the linear relation between the effective (VCMA) pumping field amplitude h and the microwave voltage amplitude $V_{\rm ac}$, which is evident from Fig. 5.3(e).

By expanding the noise term into Fourier series, we obtain the following expression for reduced power spectral density $p(f)$ of the spin wave mode oscillations:

$$\begin{aligned} p(f) = \left\langle |c(f)|^2 \right\rangle &= \frac{C_2}{(\Gamma - |hV_{00}|)^2 + (2\pi(f - f_{\rm SW}))^2} \\ &+ \frac{C_2}{(\Gamma + |hV_{00}|)^2 + (2\pi(f - f_{\rm SW}))^2} \end{aligned} \tag{5.7}$$

$$\begin{aligned} &= \frac{A}{(V_{\rm th} - V_{\rm ac})^2 + (2\pi(f - f_{\rm SW})V_{\rm th}/\Gamma)^2} \\ &+ \frac{A}{(V_{\rm th} + V_{\rm ac})^2 + (2\pi(f - f_{\rm SW})V_{\rm th}/\Gamma)^2}, \end{aligned} \tag{5.8}$$

where $A = C_2 V_{\rm th}^2/\Gamma^2$ is a constant. Setting $f = f_{\rm SW}$ in Eqn. (5.8), we obtain an expression for the peak value of the reduced PSD that is observed at $f = f_{\rm SW} = f_{\rm pr}/2$:

$$p(f_{\rm pr}/2) = \left\langle |c(f_{\rm pr}/2)|^2 \right\rangle = \frac{A}{(V_{\rm th} - V_{\rm ac})^2} + \frac{A}{(V_{\rm th} + V_{\rm ac})^2}. \tag{5.9}$$

The second term in Eqn. (5.9) is much smaller than the first one for $V_{\rm ac}$ approaching $V_{\rm th}$ and it can be neglected in fitting the experimental data of Fig. 5.3:

$$p(f_{\rm pr}/2) = \left\langle |c(f_{\rm pr}/2)|^2 \right\rangle = \frac{A}{(V_{\rm th} - V_{\rm ac})^2}. \tag{5.10}$$

Above the threshold. Well above the threshold ($V_{\rm ac} \gg V_{\rm th}$), the integrated power of the parametrically excited quasi-uniform mode is nearly temperature independent and can be approximated by its zero-temperature value [115]. Neglecting the thermal noise term in Eqn. (5.4), we derive:

$$p = |c|^2 = \frac{1}{|\Psi|}\left(\sqrt{(hV_{00})^2 - (h_{\rm th}V_{00})^2} + 2\pi(f_{\rm pr}/2 - f_{\rm SW})\text{sign}(\Psi)\right). \tag{5.11}$$

We assume that the deviation of $f_{\rm pr}$ from $2f_{\rm SW}$ is small, so that the second term in the parentheses can be neglected compared to the first term. In this case, Eqn. (5.11) takes a simple form:

$$p = B\sqrt{V_{\rm ac}^2 - V_{\rm th}^2}, \tag{5.12}$$

where $B = \Gamma/(|\Psi|V_{\rm th})$ is a constant.

5.4.2 Experimental Determination of the Parametric Resonance Threshold

In order to quantitatively determine the threshold drive voltage $V_{\rm th}$ needed to excite parametric resonance of the quasi-uniform mode, we analyze reduced power of this mode p as a function of the drive amplitude $V_{\rm ac}$. By definition, $p = |c|^2$ where c is dimensionless amplitude of the quasi-uniform mode, which is proportional to the amplitude of the MTJ resistance oscillations, so that $p \sim (GR_{\rm ac})^2$. It is clear from Eqn. 5.3 that PSD of the reduced power $p(f)$ is proportional to $P(f)/V_{\rm ac}^2$ for any $V_{\rm ac}$. In Fig. 5.3, we plot its resonant value $P(f_{\rm pr}/2)/V_{\rm ac}^2$, which is proportional to $p(f_{\rm pr}/2)$, as a function of $V_{\rm ac}$.

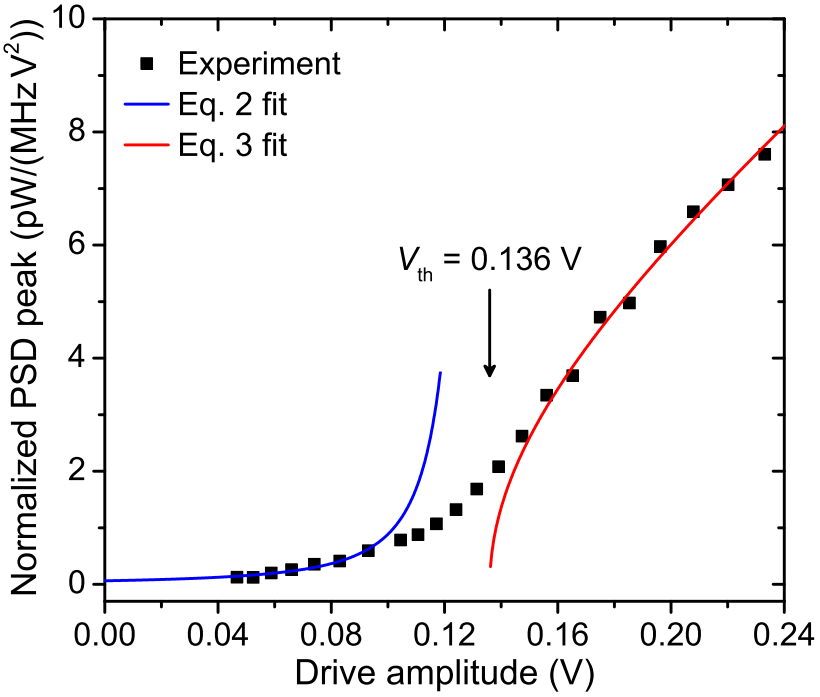

Figure 5.3: **Parametric resonance threshold.** Normalized peak amplitude of PSD, $P(f_{\rm pr}/2)/V_{\rm ac}^2$, measured at parametric resonance as a function of the parametric drive amplitude $V_{\rm ac}$. Best fits of Eqn. 5.13 and Eqn. 5.14 to the data (solid lines) give the parametric resonance threshold voltage $V_{\rm th} = 0.136\,{\rm V}$.

Analytical expressions for $p(f_{\rm pr}/2)$ can be derived in the limit of $V_{\rm ac} \ll V_{\rm th}$. In this limit, magnetization dynamics are small-amplitude thermal fluctuations amplified by the parametric drive, for which:

$$p(f_{\rm pr}/2) = \frac{A}{(V_{\rm th} - V_{\rm ac})^2}, \tag{5.13}$$

where A is a constant.

In the opposite limit of $V_{\rm ac} \gg V_{\rm th}$, thermal fluctuations can be neglected and the following analytical expression for the reduced power p can be derived:

$$p = B\sqrt{V_{\rm ac}^2 - V_{\rm th}^2}, \tag{5.14}$$

where B is a constant.

For our system, p in Eqn. 5.14 can be replaced by $p(f_{\rm pr}/2)$ because the measured spectral linewidth of $P(f)$ at $f_{\rm d} = f_{\rm pr}$ depends weakly on $V_{\rm ac}$ for $V_{\rm ac} > 0.16\,{\rm V}$. Therefore, we can fit the data in Fig. 5.3 using Eqn. 5.13 in the small amplitude limit and Eqn. 5.14 in the large amplitude limit. The best fit shown by the blue (small amplitude) and red (large amplitude) lines in Fig. 5.3 gives $V_{\rm th} = 0.136\,{\rm V}$. In this fitting procedure, A and B are free fitting parameters while $V_{\rm th}$ is treated as a common fitting parameter for both the small and large amplitude limits, see at the end of this section for the fitting procedure.

It is instructive to compare the measured $V_{\rm th}$ to its theoretically expected value for our MTJ geometry and the measured VCMA efficiency. The calculated threshold voltage in the macrospin approximation is $V_{\rm th} = 0.086\,{\rm V}$ while that given by micromagnetic simulations is $V_{\rm th} = 0.156\,{\rm V}$. The measured value is similar to the micromagnetic prediction, which lends support to VCMA origin of the observed parametric resonance.

In our experiment, spin-polarized tunneling current flows through the MTJ, which results in ST and Oersted field acting on the free layer. However, these types of drive play a negligible

role in exciting parametric resonance compared to the VCMA drive. The Oersted field has nearly circular symmetry and therefore it poorly couples to the quasi-uniform mode. The effective fields of both the field-like and damping-like ST lie in the sample plane, which corresponds to perpendicular pumping geometry. Parametric excitation of the quasi-uniform mode at $f_d = 2f_{\mathrm{SW}}$ is inefficient in this geometry [15].

Details of the fitting procedure. The fitting of the normalized peak power data shown in Fig. 5.3 to Eqn. (5.10) and Eqn. (5.12) was performed by the least squares method with A, B and V_{th} as fitting parameters. A range of data near the threshold voltage must be excluded in the fitting procedure because neither Eqn. (5.10) nor Eqn. (5.12) is valid at the threshold voltage. We chose the data range where $V_{\mathrm{ac}} < 0.1\,\mathrm{V}$ for the low-power fit and the data range where $V_{\mathrm{ac}} > 0.16\,\mathrm{V}$ for the high-power fit (the excluded data range is $0.1\,\mathrm{V}$ – $0.16\,\mathrm{V}$) because the best fit parameters do not change significantly upon further extension of the excluded data range. The threshold voltage given by this fitting procedure is $V_{\mathrm{th}} = 0.136\,\mathrm{V}$.

5.5 Parametric Resonance of Perpendicular MTJ via ST-FMR

Our experiment employs MTJ magnetic configuration with in-plane SAF and out-of-plane free layer that is convenient for unambiguous demonstration and quantitative analysis of parametric resonance excited by VCMA. However, we find that VCMA-driven parametric resonance can be observed in other types of MTJ configurations. Figure 5.4 shows out-of-plane magnetic field dependence of ST-FMR spectra measured for a $30\,\mathrm{nm} \times 95\,\mathrm{nm}$ MTJ with out-of-plane equilibrium configuration of both the free and SAF layers. Owing to the smaller amplitude of the rectified voltage in this collinear geometry, we employ ultra-sensitive ST-FMR with magnetic field modulation [44] rather than conventional ST-FMR

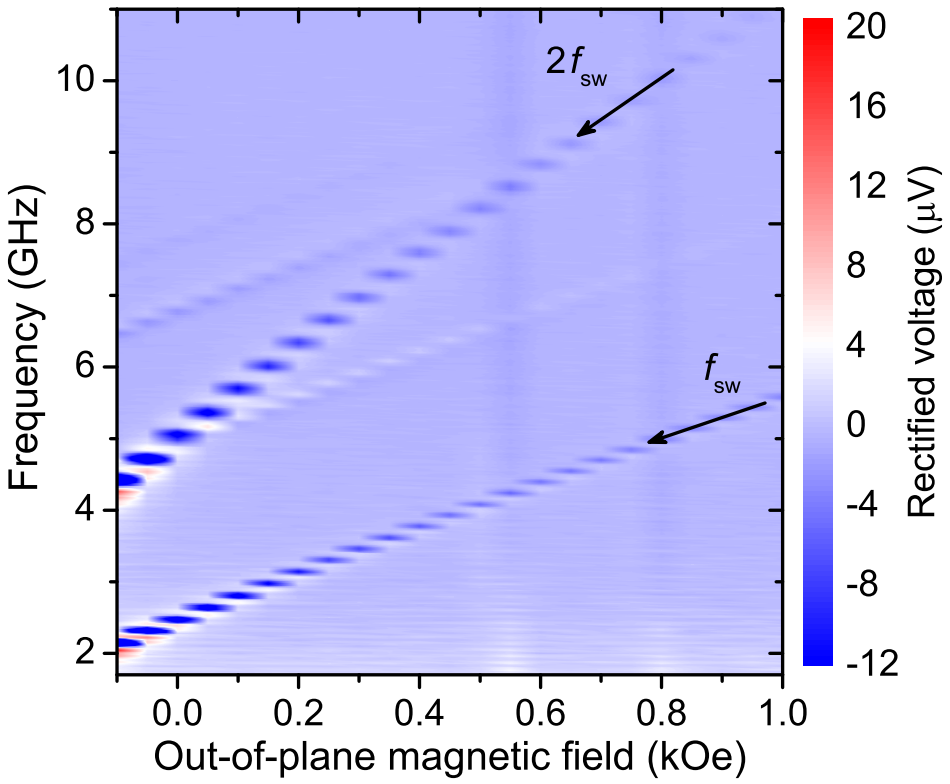

Figure 5.4: **Parametric resonance in ST-FMR.** ST-FMR spectra of an MTJ with out-of-plane SAF and free layers measured as a function of out-of-plane magnetic field. Resonance at twice the quasi-uniform mode frequency arises from parametric excitation of the quasi-uniform mode.

with amplitude modulation.

The ST-FMR spectra measured at a large value of the microwave drive voltage $V_{ac} = 0.4\,V$ reveal several spin wave eigenmodes of the free layer. Another prominent resonance is observed at twice the frequency of the lowest-frequency (quasi-uniform) spin wave eigenmode. In this collinear MTJ geometry, the microwave resistance oscillations of the device have a significant component at twice the excited spin wave mode frequency and mix with the parametric drive at twice the mode frequency to give rise to a rectified voltage peak at $2f_{SW}$ measured by ST-FMR. The amplitude of this additional resonance at $2f_{SW}$ relative to the amplitude of the resonance at f_{SW} increases with increasing V_{ac}, which is a signature of a thermally smeared threshold behavior similar to that in Fig. 5.3. The out-of-plane collinear geometry is commonly employed in spin torque magnetic memory (STT-MRAM), and parametric resonance signals in ST-FMR of STT-MRAM can potentially be used for characterization of the free layer properties such as magnetic damping.

5.6 Conclusion

In summary, our work shows that magneto-electric coupling can be used to excite parametric resonance of magnetization by electric field. We employ voltage-controlled magnetic anisotropy at the CoFeB/MgO interface to parametrically excite a spin wave mode in the free layer of a nanoscale magnetic tunnel junction. The threshold voltage for parametric excitation in this system is found to be well below 1 Volt, which is attractive for applications in energy-efficient spintronic and magnonic nanodevices such as spin wave logic [130]. This work opens a new energy-efficient route for excitation of magnetization dynamics in thin films of metallic ferromagnets and nanodevices based on magnetic multilayers.

Chapter 6

Conclusion and Future Work

In conclusion, the experimental results in Pt/LSMO bilayer system show relatively high spin mixing conductance and the very low Gilbert damping (comparable with the best reported values of other metallic ferromagnets). These results make Pt/LSMO an attractive system for making spin Hall nanowire oscillators [27, 54, 56, 78, 79] because both results indicate a possible reduction of critical current density J_{c0} for driving microwave emission. However, there exist several hampering factors for making nanowire oscillator based on Pt/LSMO. First, the significant negative PMA in LSMO films on STO substrate is expected to increase J_{c0} because the negative sign makes the magnetization to prefer to lie within the film plane and this adds an extra energy to overcome. A more problematic finding is that the surface of STO substrate is known to become conductive after the ion-milling operation due to the creation of oxygen vacancies and imperfections left on the surface. The conductive surface is a source of shunting pathway for RF current in the nanowire and results in smaller signal amplitude. In contrast, for example, $(LaAlO_3)_{0.3}(Sr_2TaAlO_6)_{0.7}$ (LSAT) substrate is known to remain electrically insulating even after the ion-milling operation. Therefore finding a good insulating substrate that maintains low magnetic damping of Pt/LSMO bilayer and positive PMA will be a key to realize its application for the spin Hall nanowire oscillator.

The work in nonlinear resonant three-magnon scattering will have a substantial impact on the performance evaluation of spin-torque magnetic memory (STT-MRAM) based on MTJs and spin-torque nano-oscillators. First, this effect has been observed in both types of MTJs, in-plane magnetized and perpendicularly magnetized, which points to the universality of the effect. The critical current density of all these devices relies on large-amplitude oscillations of magnetization driven by spin torque. Therefore, the limiting amplitude resulting from the resonant nonlinear damping is expected to have a detrimental effect on the device performance. Experimental study of spin-torque driven switching in the presence of extra damping by three-magnon scattering will be very interesting and will be a primary focus of future work.

Lastly, our demonstration of VCMA-driven parametric resonance of spin wave in nanomagnet leaves several excellent questions to study in future. First, the MTJ employed in this study has MgO thickness that allows the flow of tunneling current. Since VCMA effect does not rely on high current density but results from electric field effect, I expect parametric resonance will become an increasingly important method for generating spin-wave eigenmodes in pMTJs having thick MgO barrier, where spin torque effect will become increasingly small. Second, it will be interesting to observe parametric resonance of higher-order spin-wave mode, which I have tried hard without a success at room temperature measurements. One possible reason might be rooted to the spatially non-uniform amplitude of higher-order spin-wave eigenmodes. If the non-uniformity in the spatial profile decreases the overall ellipticity of magnetization precession, it can potentially increase the threshold of parametric excitation for these modes. Perhaps, reducing the measurement temperature can result in a better chance to observe the parametric resonance signal of higher-order modes because smearing of the threshold, due to thermal fluctuations, will be reduced.

This work also leads to several exciting directions for the nanomagnonics research. The sub-1 V threshold voltage for parametric excitation found in this study is quite attractive

for applications in magnonic nanodevices such as spin wave logic [130]. The propagating spin wave is the information carrier in these applications. It will be fascinating to observe parametric pumping of propagating spin wave driven by VCMA because this will open a new platform for experimenting the effect of VCMA on controlling the spin wave propagation. Finally, I expect VCMA-driven parametric resonance will come increasingly important technique for fundamental research and for practical applications as the material system having higher VCMA efficiency to be discovered in future.

Bibliography

[1] R. C. O'Handley. *Modern magnetic materials*. John Wiley and Sons, Inc., 2000.

[2] J.-G. Zhu and C. Park. Magnetic tunnel junctions. *Materials Today*, 9(11):36–45, nov 2006.

[3] J. C. Sankey, P. M. Braganca, A. G. F. Garcia, I. N. Krivorotov, R. A. Buhrman, and D. C. Ralph. Spin-transfer-driven ferromagnetic resonance of individual nanomagnets. *Physical Review Letters*, 96(22):227601, jun 2006.

[4] J. M. D. Coey. *Magnetism and magnetic materials*. Cambridge University Press, 2009.

[5] M. Farle. Ferromagnetic resonance of ultrathin metallic layers. *Reports on Progress in Physics*, 61(7):755–826, jul 1998.

[6] A. Aharoni. Demagnetizing factors for rectangular ferromagnetic prisms. *Journal of Applied Physics*, 83(6):3432–3434, mar 1998.

[7] M. T. Johnson, P. J. H. Bloemen, F. J. A. den Broeder, and J. J. de Vries. Magnetic anisotropy in metallic multilayers. *Reports on Progress in Physics*, 59(11):1409–1458, nov 1996.

[8] I. Barsukov, P. Landeros, R. Meckenstock, J. Lindner, D. Spoddig, Z.-A. Li, B. Krumme, H. Wende, D. L. Mills, and M. Farle. Tuning magnetic relaxation by oblique deposition. *Physical Review B*, 85(1):014420, jan 2012.

[9] T. Maruyama, Y. Shiota, T. Nozaki, K. Ohta, N. Toda, M. Mizuguchi, A. A. Tulapurkar, T. Shinjo, M. Shiraishi, S. Mizukami, Y. Ando, and Y. Suzuki. Large voltage-induced magnetic anisotropy change in a few atomic layers of iron. *Nature Nanotechnology*, 4(3):158–161, mar 2009.

[10] M. Endo, S. Kanai, S. Ikeda, F. Matsukura, and H. Ohno. Electric-field effects on thickness dependent magnetic anisotropy of sputtered MgO/Co40Fe40B20/Ta structures. *Applied Physics Letters*, 96(21):10–13, 2010.

[11] C. G. Duan, J. P. Velev, R. F. Sabirianov, Z. Zhu, J. Chu, S. S. Jaswal, and E. Y. Tsymbal. Surface magnetoelectric effect in ferromagnetic metal films. *Physical Review Letters*, 101(13):1–4, 2008.

[12] M. K. Niranjan, C.-G. Duan, S. S. Jaswal, and E. Y. Tsymbal. Electric field effect on magnetization at the Fe/MgO(001) interface. *Applied Physics Letters*, 96(22):222504, may 2010.

[13] Y. Shiota, F. Bonell, S. Miwa, N. Mizuochi, T. Shinjo, and Y. Suzuki. Opposite signs of voltage-induced perpendicular magnetic anisotropy change in CoFeB/MgO junctions with different underlayers. *Applied Physics Letters*, 103(8):082410, aug 2013.

[14] S. V. Vonsovskii. *Ferromagnetic resonance*. Pergamon, Oxford, 1960.

[15] A. G. Gurevich and G. A. Melkov. *Magnetization Oscillations and Waves*. CRC, 1996.

[16] G. A. Melkov, Yu. V. Kobljanskyj, A. A. Serga, V. S. Tiberkevich, and A. N. Slavin. Reversal of momentum relaxation. *Physical Review Letters*, 86(21):4918–4921, may 2001.

[17] A. V. Chumak, V. I. Vasyuchka, A. A. Serga, M. P. Kostylev, V. S. Tiberkevich, and B. Hillebrands. Storage-recovery phenomenon in magnonic crystal. *Physical Review Letters*, 108(25):257207, jun 2012.

[18] V. V. Kruglyak, S. O. Demokritov, and D. Grundler. Magnonics. *Journal of Physics D: Applied Physics*, 43(26):264001, jul 2010.

[19] A. V. Chumak, V. I. Vasyuchka, A. A. Serga, and B. Hillebrands. Magnon spintronics. *Nature Physics*, 11(6):453–461, jun 2015.

[20] S. Urazhdin, V. Tiberkevich, and A. Slavin. Parametric excitation of a magnetic nanocontact by a microwave field. *Physical Review Letters*, 105(23):237204, dec 2010.

[21] J. C. Slonczewski. Current-driven excitation of magnetic multilayers. *Journal of Magnetism and Magnetic Materials*, 159(1-2):L1–L7, jun 1996.

[22] L. Berger. Emission of spin waves by a magnetic multilayer traversed by a current. *Physical Review B*, 54(13):9353–9358, oct 1996.

[23] D. C. Ralph and M. D. Stiles. Spin transfer torques. *Journal of Magnetism and Magnetic Materials*, 320(7):1190–1216, apr 2008.

[24] G. E. Rowlands. *Stochastic magnetization dynamics in patterned nanostructures*. Dissertation, University of California, Irvine, 2012.

[25] J. Sinova, S. O. Valenzuela, J. Wunderlich, C. H. Back, and T. Jungwirth. Spin Hall effects. *Reviews of Modern Physics*, 87(4):1213–1260, oct 2015.

[26] L. Liu, C.-F. Pai, Y. Li, H. W. Tseng, D. C. Ralph, and R. A. Buhrman. Spin-torque switching with the giant spin Hall effect of tantalum. *Science*, 336(6081):555–558, may 2012.

[27] Z. Duan, A. Smith, L. Yang, B. Youngblood, J. Lindner, V. E. Demidov, S. O. Demokritov, and I. N. Krivorotov. Nanowire spin torque oscillator driven by spin orbit torques. *Nature Communications*, 5:5616, dec 2014.

[28] M. I. Dyakonov and V. I. Perel. Current-induced spin orientation of electrons in semiconductors. *Physics Letters A*, 35(6):459–460, jul 1971.

[29] J. Hirsch. Spin Hall effect. *Physical Review Letters*, 83(9):1834–1837, aug 1999.

[30] A. Hoffmann. Spin Hall effects in metals. *IEEE Transactions on Magnetics*, 49(10):5172–5193, oct 2013.

[31] K. Ando, S. Takahashi, J. Ieda, Y. Kajiwara, H. Nakayama, T. Yoshino, K. Harii, Y. Fujikawa, M. Matsuo, S. Maekawa, and E. Saitoh. Inverse spin-Hall effect induced by spin pumping in metallic system. *Journal of Applied Physics*, 109(10):103913, 2011.

[32] M. Harder, Y. S. Gui, and C. M. Hu. Electrical detection of magnetization dynamics via spin rectification effects. *Physics Reports*, 661:1–59, 2016.

[33] R. Arias and D. L. Mills. Extrinsic contributions to the ferromagnetic resonance response of ultrathin films. *Physical Review B*, 60(10):7395–7409, sep 1999.

[34] Kh. Zakeri, J. Lindner, I. Barsukov, R. Meckenstock, M. Farle, U. von Hörsten, H. Wende, W. Keune, J. Rocker, S. S. Kalarickal, K. Lenz, W. Kuch, K. Baberschke, and Z. Frait. Spin dynamics in ferromagnets: Gilbert damping and two-magnon scattering. *Physical Review B*, 76(10):104416, sep 2007.

[35] Y. Tserkovnyak, A. Brataas, and G. E. W. Bauer. Enhanced Gilbert damping in thin ferromagnetic Films. *Physical Review Letters*, 88(11):117601, feb 2002.

[36] Y. Tserkovnyak, A. Brataas, and G. E. W. Bauer. Spin pumping and magnetization dynamics in metallic multilayers. *Physical Review B*, 66(22):224403, dec 2002.

[37] R. Urban, G. Woltersdorf, and B. Heinrich. Gilbert damping in single and multilayer ultrathin films: Role of interfaces in nonlocal spin dynamics. *Physical Review Letters*, 87(21):217204, nov 2001.

[38] E. Saitoh, M. Ueda, H. Miyajima, and G. Tatara. Conversion of spin current into charge current at room temperature: Inverse spin-Hall effect. *Applied Physics Letters*, 88(18):182509, 2006.

[39] O. Mosendz, J. E. Pearson, F. Y. Fradin, G. E. W. Bauer, S. D. Bader, and A. Hoffmann. Quantifying spin Hall angles from spin pumping: Experiments and theory. *Physical Review Letters*, 104(4):046601, jan 2010.

[40] M.-H. Nguyen, D. C. Ralph, and R.A. Buhrman. Spin torque study of the spin Hall conductivity and spin diffusion length in platinum thin films with varying resistivity. *Physical Review Letters*, 116(12):126601, mar 2016.

[41] S. Takahashi and S. Maekawa. Spin current, spin accumulation and spin Hall effect. *Science and Technology of Advanced Materials*, 9(1):014105, jan 2008.

[42] M. Weiler, J. M. Shaw, H. T. Nembach, and T. J. Silva. Phase-sensitive detection of spin pumping via the ac inverse spin Hall effect. *Physical Review Letters*, 113(15):157204, oct 2014.

[43] I. Harward, T. O'Keevan, A. Hutchison, V. Zagorodnii, and Z. Celinski. A broadband ferromagnetic resonance spectrometer to measure thin films up to 70 GHz. *Review of Scientific Instruments*, 82(9):095115, 2011.

[44] A. M. Gonçalves, I. Barsukov, Y.-J. Chen, L. Yang, J. A. Katine, and I. N. Krivorotov. Spin torque ferromagnetic resonance with magnetic field modulation. *Applied Physics Letters*, 103(17):172406, oct 2013.

[45] J. Coonrod and B. Rautio. Comparing microstrip and CPW performance. *Microwave Journal*, 55:74–80, 2012.

[46] B. Rosas. The design and test of broadband launches up to 50 GHz on thin and thick substrates. Technical Report, Southwest Microwave, Inc., 2011, available at http://mpd.southwestmicrowave.com/resources/.

[47] A. A. Tulapurkar, Y. Suzuki, A. Fukushima, H. Kubota, H. Maehara, K. Tsunekawa, D. D. Djayaprawira, N. Watanabe, and S. Yuasa. Spin-torque diode effect in magnetic tunnel junctions. *Nature*, 438(7066):339–342, nov 2005.

[48] M. Harder, Z. X. Cao, Y. S. Gui, X. L. Fan, and C.-M. Hu. Analysis of the line shape of electrically detected ferromagnetic resonance. *Physical Review B*, 84(5):054423, aug 2011.

[49] J. Lindner, I. Barsukov, C. Raeder, C. Hassel, O. Posth, R. Meckenstock, P. Landeros, and D. L. Mills. Two-magnon damping in thin films in case of canted magnetization: Theory versus experiment. *Physical Review B*, 80(22):224421, dec 2009.

[50] I. Barsukov, R. Meckenstock, J. Lindner, M. Moller, C. Hassel, O. Posth, M. Farle, and H. Wende. Tailoring spin relaxation in thin films by tuning extrinsic relaxation channels. *IEEE Transactions on Magnetics*, 46(6):2252–2255, jun 2010.

[51] L. Liu, T. Moriyama, D. C. Ralph, and R. A. Buhrman. Spin-torque ferromagnetic resonance induced by the spin Hall effect. *Physical Review Letters*, 106(3):036601, jan 2011.

[52] J.-C. Rojas-Sánchez, N. Reyren, P. Laczkowski, W. Savero, J.-P. Attané, C. Deranlot, M. Jamet, J.-M. George, L. Vila, and H. Jaffrès. Spin pumping and inverse spin Hall effect in platinum: The essential role of spin-memory loss at metallic interfaces. *Physical Review Letters*, 112(10):106602, mar 2014.

[53] B. Heinrich, C. Burrowes, E. Montoya, B. Kardasz, E. Girt, Y.-Y. Song, Y. Sun, and M. Wu. Spin pumping at the magnetic insulator (YIG)/normal metal (Au) interfaces. *Physical Review Letters*, 107(6):066604, aug 2011.

[54] M. Collet, X. de Milly, O. d'Allivy Kelly, V. V. Naletov, R. Bernard, P. Bortolotti, J. Ben Youssef, V. E. Demidov, S. O. Demokritov, J. L. Prieto, M. Muñoz, V. Cros, A. Anane, G. de Loubens, and O. Klein. Generation of coherent spin-wave modes in yttrium iron garnet microdiscs by spin-orbit torque. *Nature Communications*, 7:10377, jan 2016.

[55] H. L. Wang, C. H. Du, Y. Pu, R. Adur, P. C. Hammel, and F. Y. Yang. Scaling of Spin Hall Angle in 3d, 4d, and 5d Metals from $Y_3Fe_5O_{12}$/metal spin pumping. *Physical Review Letters*, 112(19):197201, may 2014.

[56] V. E. Demidov, S. Urazhdin, H. Ulrichs, V. Tiberkevich, A. Slavin, D. Baither, G. Schmitz, and S. O. Demokritov. Magnetic nano-oscillator driven by pure spin current. *Nature Materials*, 11(12):1028–1031, oct 2012.

[57] K. Gilmore, Y. U. Idzerda, and M. D. Stiles. Spin-orbit precession damping in transition metal ferromagnets (invited). *Journal of Applied Physics*, 103(7):07D303, 2008.

[58] S. Majumdar and S. van Dijken. Pulsed laser deposition of $La_{1-x}Sr_xMnO_3$: Thin-film properties and spintronic applications. *Journal of Physics D: Applied Physics*, 47(3):034010, 2014.

[59] M. Bowen, M. Bibes, A. Barthelemy, J. P. Contour, A. Anane, A. Lemaitre, and A Fert. Nearly total spin polarization in $La_{2/3}Sr_{1/3}MnO_3$ from tunneling experiments. *Applied Physics Letters*, 82(2):233–235, jan 2003.

[60] B. Kim, D. Kwon, J. H. Song, Y. Hikita, B. G. Kim, and H. Y. Hwang. Finite size effect and phase diagram of ultra-thin $La_{0.7}Sr_{0.3}MnO_3$. *Solid State Communications*, 150(13-14):598–601, apr 2010.

[61] C. Liu, C. K. A. Mewes, M. Chshiev, T. Mewes, and W. H. Butler. Origin of low Gilbert damping in half metals. *Applied Physics Letters*, 95(2):022509, 2009.

[62] J. H. Song, T. Susaki, and H. Y. Hwang. Enhanced thermodynamic stability of epitaxial oxide thin films. *Advanced Materials*, 20(13):2528–2532, jul 2008.

[63] L. F. Kourkoutis, J. H. Song, H. Y. Hwang, and D. A. Muller. Microscopic origins for stabilizing room-temperature ferromagnetism in ultrathin manganite layers. *Proceedings of the National Academy of Sciences*, 107(26):11682–11685, jun 2010.

[64] Y. Hikita, M. Nishikawa, T. Yajima, and H. Y. Hwang. Termination control of the interface dipole in $La_{0.7}Sr_{0.3}MnO_3$/Nb:$SrTiO_3$ (001) Schottky junctions. *Physical Review B*, 79(7):073101, feb 2009.

[65] G. Y. Luo, M. Belmeguenai, Y. Roussigné, C. R. Chang, J. G. Lin, and S. M. Chérif. Enhanced magnetic damping in La0.7Sr0.3MnO3 capped by normal metal layer. *AIP Advances*, 5(9):097148, sep 2015.

[66] V. A. Ivanshin, J. Deisenhofer, H.-A. Krug von Nidda, A. Loidl, A. A. Mukhin, A. M. Balbashov, and M. V. Eremin. ESR study in lightly doped $La_{1-x}Sr_xMnO_3$. *Physical Review B*, 61(9):6213–6219, mar 2000.

[67] Å. Monsen, J. E. Boschker, F. Macià, J. W. Wells, P. Nordblad, A. D. Kent, R. Mathieu, T. Tybell, and E. Wahlström. Thickness dependence of dynamic and static magnetic properties of pulsed laser deposited $La_{0.7}Sr_{0.3}MnO_3$ films on $SrTiO_3$(001). *Journal of Magnetism and Magnetic Materials*, 369:197–204, nov 2014.

[68] M. Belmeguenai, S. Mercone, C. Adamo, T. Chauveau, L.. Méchin, P. Monod, P. Moch, and D. G. Schlom. La0.7Sr0.3MnO3 thin films on SrTiO3 and CaTiO3 buffered Si substrates: structural, static, and dynamic magnetic properties. *Journal of Nanoparticle Research*, 13(11):5669–5675, nov 2011.

[69] M. Mathews, F. M. Postma, J. C. Lodder, R. Jansen, G. Rijnders, and D. H. A. Blank. Step-induced uniaxial magnetic anisotropy of $La_{0.67}Sr_{0.33}MnO_3$ thin films. *Applied Physics Letters*, 87(24):242507, 2005.

[70] P. Perna, C. Rodrigo, E. Jimenez, F. J. Teran, N. Mikuszeit, L. Mechin, J. Camarero, and R. Miranda. Tailoring magnetic anisotropy in epitaxial half metallic $La_{0.7}Sr_{0.3}MnO_3$ thin films. *Journal of Applied Physics*, 110(1):013919, 2011.

[71] G. Counil, J.-V. Kim, T. Devolder, C. Chappert, K. Shigeto, and Y. Otani. Spin wave contributions to the high-frequency magnetic response of thin films obtained with inductive methods. *Journal of Applied Physics*, 95(10):5646, 2004.

[72] H. T. Nembach, T. J. Silva, J. M. Shaw, M. L. Schneider, M. J. Carey, S. Maat, and J. R. Childress. Perpendicular ferromagnetic resonance measurements of damping and Landé g-factor in sputtered $(Co_2Mn)_{1-x}Ge_x$ thin films. *Physical Review B*, 84(5):054424, aug 2011.

[73] G. Y. Luo, C. R. Chang, and J. G. Lin. Thickness dependent spin pumping effects in $La_{0.7}Sr_{0.3}MnO_3$/platinum bilayer film. *IEEE Transactions on Magnetics*, 49(7):4371–4374, jul 2013.

[74] I. Barsukov, S. Mankovsky, A. Rubacheva, R. Meckenstock, D. Spoddig, J. Lindner, N. Melnichak, B. Krumme, S. I. Makarov, H. Wende, H. Ebert, and M. Farle. Magnetocrystalline anisotropy and Gilbert damping in iron-rich $Fe_{1-x}Si_x$ thin films. *Physical Review B*, 84(18):180405, nov 2011.

[75] C. Scheck, L. Cheng, I. Barsukov, Z. Frait, and W. E. Bailey. Low relaxation rate in epitaxial vanadium-doped ultrathin iron films. *Physical Review Letters*, 98(11):117601, mar 2007.

[76] S. Mizukami, D. Watanabe, M. Oogane, Y. Ando, Y. Miura, M. Shirai, and T. Miyazaki. Low damping constant for Co_3FeAl Heusler alloy films and its correlation with density of states. *Journal of Applied Physics*, 105(7):07D306, 2009.

[77] R. A. Gallardo, A. Banholzer, K. Wagner, M Körner, K. Lenz, M. Farle, J. Lindner, J. Fassbender, and P. Landeros. Splitting of spin-wave modes in thin films with arrays of periodic perturbations: theory and experiment. *New Journal of Physics*, 16(2):023015, feb 2014.

[78] S. I. Kiselev, J. C. Sankey, I. N. Krivorotov, N. C. Emley, R. J. Schoelkopf, R. A. Buhrman, and D. C. Ralph. Microwave oscillations of a nanomagnet driven by a spin-polarized current. *Nature*, 425(6956):380–383, sep 2003.

[79] L. Yang, R. Verba, V. Tiberkevich, T. Schneider, A. Smith, Z. Duan, B. Youngblood, K. Lenz, J. Lindner, A. N. Slavin, and I. N. Krivorotov. Reduction of phase noise in nanowire spin orbit torque oscillators. *Scientific Reports*, 5:16942, nov 2015.

[80] H. Suhl. The theory of ferromagnetic resonance at high signal powers. *Journal of Physics and Chemistry of Solids*, 1(4):209 – 227, 1957.

[81] H. G. Bauer, P. Majchrak, T. Kachel, C. H. Back, and G. Woltersdorf. Nonlinear spin-wave excitations at low magnetic bias fields. *Nature Communications*, 6:8274, 2015.

[82] M. Bauer, O. Büttner, S. O. Demokritov, B. Hillebrands, V. Grimalsky, Yu. Rapoport, and A. N. Slavin. Observation of spatiotemporal self-focusing of spin waves in magnetic films. *Phys. Rev. Lett.*, 81:3769–3772, Oct 1998.

[83] A. N. Slavin and I. V. Rojdestvenski. Bright and dark spin wave envelope solitons in magnetic films. *IEEE Transactions on Magnetics*, 30(1):37–45, Jan 1994.

[84] M. Wu, B. A. Kalinikos, and C. E. Patton. Self-generation of chaotic solitary spin wave pulses in magnetic film active feedback rings. *Physical Review Letters*, 95(23):237202, November 2005.

[85] M. D'Aquino, A. Quercia, V. Scalera, S. Perna, G. Bertotti, I. D. Mayergoyz, and C. Serpico. Analytical treatment of nonlinear ferromagnetic resonance in nanomagnets. *IEEE Transactions on Magnetics*, 9464(2):1–1, 2017.

[86] I. N. Krivorotov, N. C. Emley, R. A. Buhrman, and D. C. Ralph. Time-domain studies of very-large-angle magnetization dynamics excited by spin transfer torques. *Physical Review B*, 77(5):054440, 2008.

[87] C. T. Boone, J. A. Katine, J. R. Childress, V. Tiberkevich, A. Slavin, J. Zhu, X. Cheng, and I. N. Krivorotov. Resonant nonlinear damping of quantized spin waves in ferromagnetic nanowires: A spin torque ferromagnetic resonance study. *Phys. Rev. Lett.*, 103:167601, Oct 2009.

[88] W. H. Rippard, A. M. Deac, M. R. Pufall, J. M. Shaw, M. W. Keller, S. E. Russek, G. E. W. Bauer, and C. Serpico. Spin-transfer dynamics in spin valves with out-of-plane magnetized CoNi free layers. *Physical Review B*, 81(1):014426, jan 2010.

[89] D. Houssameddine, U. Ebels, B. Delat, B. Rodmacq, I. Firastrau, F. Ponthenier, M. Brunet, C. Thirion, J.-P. Michel, L. Prejbeanu-Buda, M.-C. Cyrille, O. Redon, and B. Dieny. Spin-torque oscillator using a perpendicular polarizer and a planar free layer. *Nature Materials*, 6(6):447–453, 2007.

[90] A. Houshang, E. Iacocca, P. Drrenfeld, S. R. Sani, J. kerman, and R. K. Dumas. Spin-wave-beam driven synchronization of nanocontact spin-torque oscillators. *Nature Nanotechnology*, 11(3):280–286, 2016.

[91] F. Macià, D. Backes, and A. D. Kent. Stable magnetic droplet solitons in spin-transfer nanocontacts. *Nature Nanotechnology*, 9(12):992–996, nov 2014.

[92] J. Zhu, J. A. Katine, G. E. Rowlands, Y.-J. Chen, J. G. Duan, Z.and Alzate, P. Upadhyaya, J. Langer, P. K. Amiri, K. L. Wang, and I. N. Krivorotov. Voltage-induced ferromagnetic resonance in magnetic tunnel junctions. *Physical Review Letters*, 108(19):197203, may 2012.

[93] S. Miwa, S. Ishibashi, H. Tomita, T. Nozaki, E. Tamura, K. Ando, N. Mizuochi, T. Saruya, H. Kubota, K. Yakushiji, T. Taniguchi, H. Imamura, A. Fukushima, S. Yuasa, and Y. Suzuki. Highly sensitive nanoscale spin-torque diode. *Nature Materials*, 13(1):50–56, 2014.

[94] B. Fang, M. Carpentieri, X. Hao, H. Jiang, J. A. Katine, I. N. Krivorotov, B. Ocker, J. Langer, K. L. Wang, B. Zhang, B. Azzerboni, P. K. Amiri, G. Finocchio, and Z. Zeng. Giant spin-torque diode sensitivity in the absence of bias magnetic field. *Nature Communications*, 7:11259, 2016.

[95] M. Shinozaki, E. Hirayama, S. Kanai, H. Sato, F. Matsukura, and H. Ohno. Damping constant in a free layer in nanoscale CoFeB/MgO magnetic tunnel junctions investigated by homodyne-detected ferromagnetic resonance. *Applied Physics Express*, 10(1):013001, 2017.

[96] C. J. Safranski, Y.-J. Chen, I. N. Krivorotov, and J. Z. Sun. Material parameters of perpendicularly magnetized tunnel junctions from spin torque ferromagnetic resonance techniques. *Applied Physics Letters*, 109(13):132408, 2016.

[97] C. Liu, Y. Boyko, C. C. Geppert, K. D. Christie, G. Stecklein, S. J. Patel, C. J. Palmstrm, and P. A. Crowell. Electrical detection of ferromagnetic resonance in ferromagnet/n-GaAs heterostructures by tunneling anisotropic magnetoresistance. *Applied Physics Letters*, 105(21):212401, 2014.

[98] C. L. Ordóñez Romero, B. A. Kalinikos, P. Krivosik, W. Tong, P. Kabos, and C. E. Patton. Three-magnon splitting and confluence processes for spin-wave excitations in yttrium iron garnet films: Wave vector selective brillouin light scattering measurements and analysis. *Phys. Rev. B*, 79:144428, Apr 2009.

[99] H. Schultheiss, X. Janssens, M. van Kampen, F. Ciubotaru, S. J. Hermsdoerfer, B. Obry, A. Laraoui, A. A. Serga, L. Lagae, A. N. Slavin, B. Leven, and B. Hillebrands. Direct current control of three magnon scattering processes in spin-valve nanocontacts. *Physical Review Letters*, 103(15):157202, 2009.

[100] H. Kurebayashi, O. Dzyapko, V. E. Demidov, D. Fang, A. J. Ferguson, and S. O. Demokritov. Controlled enhancement of spin-current emission by three-magnon splitting. *Nature Materials*, 10(9):660–664, 2011.

[101] R. N. Costa Filho, M. G. Cottam, and G. A. Farias. Microscopic theory of dipole-exchange spin waves in ferromagnetic films: Linear and nonlinear processes. *Phys. Rev. B*, 62:6545–6560, Sep 2000.

[102] A. M. Deac, A. Fukushima, H. Kubota, H. Maehara, Y. Suzuki, S. Yuasa, Y. Nagamine, K. Tsunekawa, D. D. Djayaprawira, and N. Watanabe. Bias-driven high-power microwave emission from MgO-based tunnel magnetoresistance devices. *Nature Physics*, 4(10):803–809, oct 2008.

[103] V. E. Demidov, S. Urazhdin, E. R J Edwards, M. D. Stiles, R. D. McMichael, and S. O. Demokritov. Control of magnetic fluctuations by spin current. *Physical Review Letters*, 107(10):107204, sep 2011.

[104] G. D. Fuchs, J. C. Sankey, V. S. Pribiag, L. Qian, P. M. Braganca, A. G. F. Garcia, E. M. Ryan, Z.-P. Li, O. Ozatay, D. C. Ralph, and R. A. Buhrman. Spin-torque ferromagnetic resonance measurements of damping in nanomagnets. *Applied Physics Letters*, 91(6):062507, aug 2007.

[105] G. A. Melkov, D. V. Slobodianiuk, V. S. Tiberkevich, G. de Loubens, O. Klein, and A. N. Slavin. Nonlinear ferromagnetic resonance in nanostructures having discrete spectrum of spin-wave modes. *IEEE Magnetics Letters*, 4:4000504–4000504, 2013.

[106] M. Helsen, A. Gangwar, J. De Clercq, A. Vansteenkiste, M. Weigand, C. H. Back, and B. Van Waeyenberge. Non-linear radial spinwave modes in thin magnetic disks. *Applied Physics Letters*, 106(3):032405, 2015.

[107] J. Podbielski, D. Heitmann, and D. Grundler. Microwave-assisted switching of microscopic rings: Correlation between nonlinear spin dynamics and critical microwave fields. *Physical Review Letters*, 99(20):207202, 2007.

[108] V. V. Naletov, G. de Loubens, V. Charbois, O. Klein, V. S. Tiberkevich, and A. N. Slavin. Ferromagnetic resonance spectroscopy of parametric magnons excited by a four-wave process. *Phys. Rev. B*, 75:140405, Apr 2007.

[109] Y. Khivintsev, B. Kuanr, T. J. Fal, M. Haftel, R. E. Camley, Z. Celinski, and D. L. Mills. Nonlinear ferromagnetic resonance in permalloy films: A nonmonotonic power-dependent frequency shift. *Physical Review B*, 81(5):054436, 2010.

[110] B. Rana, Y. Fukuma, K. Miura, H. Takahashi, and Y. Otani. Effect of excitation power on voltage induced local magnetization dynamics in an ultrathin CoFeB film. *Scientific Reports*, 7:2318, 2017.

[111] F. Guo, L. M. Belova, and R. D. McMichael. Nonlinear ferromagnetic resonance shift in submicron permalloy ellipses. *Phys. Rev. B*, 91:064426, Feb 2015.

[112] H. T. Nembach, J. M. Shaw, C. T. Boone, and T. J. Silva. Mode- and size-dependent landau-lifshitz damping in magnetic nanostructures: Evidence for nonlocal damping. *Physical Review Letters*, 110(11):117201, 2013.

[113] Y. Li and W.E. Bailey. Wave-number-dependent Gilbert damping in metallic ferromagnets. *Physical Review Letters*, 116(11):117602, 2016.

[114] K. Sekiguchi, K. Yamada, S.-M. Seo, K.-J. Lee, D. Chiba, and T. Kobayashi, K.and Ono. Time-domain measurement of current-induced spin wave dynamics. *Physical Review Letters*, 108(1):017203, jan 2012.

[115] A. Slavin and V. Tiberkevich. Nonlinear auto-oscillator theory of microwave generation by spin-polarized current. *IEEE Transactions on Magnetics*, 45(4):1875–1918, apr 2009.

[116] V. Lauer, D. A. Bozhko, T. Brcher, P. Pirro, V. I. Vasyuchka, A. A. Serga, M. B. Jungfleisch, M. Agrawal, Yu. V. Kobljanskyj, G. A. Melkov, C. Dubs, B. Hillebrands, and A. V. Chumak. Spin-transfer torque based damping control of parametrically excited spin waves in a magnetic insulator. *Applied Physics Letters*, 108(1):012402, 2016.

[117] C. Zhang, Y. Pu, S. A. Manuilov, S. P. White, M. R. Page, E. C. Blomberg, D. V. Pelekhov, and P. C. Hammel. Engineering the spectrum of dipole field-localized spin-wave modes to enable spin-torque antidamping. *Physical Review Applied*, 7(5):054019, 2017.

[118] S. M. Rezende, F. M. de Aguiar, and A. Azevedo. Magnon excitation by spin-polarized direct currents in magnetic nanostructures. *Physical Review B*, 73(9):094402, 2006.

[119] M. Weisheit, S. Fahler, A. Marty, Y. Souche, C. Poinsignon, and D. Givord. Electric field-induced modification of magnetism in thin-film ferromagnets. *Science*, 315(5810):349–351, jan 2007.

[120] D. Chiba, M. Sawicki, Y. Nishitani, Y. Nakatani, F. Matsukura, and H. Ohno. Magnetization vector manipulation by electric fields. *Nature*, 455(7212):515–518, sep 2008.

[121] Y. Shiota, T. Nozaki, F. Bonell, S. Murakami, T. Shinjo, and Y. Suzuki. Induction of coherent magnetization switching in a few atomic layers of FeCo using voltage pulses. *Nature Materials*, 11(1):39–43, nov 2011.

[122] W.-G. Wang, M. Li, S. Hageman, and C. L. Chien. Electric-field-assisted switching in magnetic tunnel junctions. *Nature Materials*, 11(1):64–68, nov 2011.

[123] A. J. Schellekens, A. van den Brink, J. H. Franken, H. J. M. Swagten, and B. Koopmans. Electric-field control of domain wall motion in perpendicularly magnetized materials. *Nature Communications*, 3(May):847, may 2012.

[124] R. Verba, V. Tiberkevich, I. Krivorotov, and A. Slavin. Parametric excitation of spin waves by voltage-controlled magnetic anisotropy. *Physical Review Applied*, 1(4):044006, may 2014.

[125] H. Kurebayashi, O. Dzyapko, V. E. Demidov, D. Fang, A. J. Ferguson, and S. O. Demokritov. Spin pumping by parametrically excited short-wavelength spin waves. *Applied Physics Letters*, 99(16):162502, oct 2011.

[126] S. A. Manuilov, C. H. Du, R. Adur, H. L. Wang, V. P. Bhallamudi, F. Y. Yang, and P. C. Hammel. Spin pumping from spinwaves in thin film YIG. *Applied Physics Letters*, 107(4):042405, jul 2015.

[127] P. Bortolotti, E. Grimaldi, A. Dussaux, J. Grollier, V. Cros, C. Serpico, K. Yakushiji, A. Fukushima, H. Kubota, R. Matsumoto, and S. Yuasa. Parametric excitation of magnetic vortex gyrations in spin-torque nano-oscillators. *Physical Review B*, 88(17):174417, nov 2013.

[128] R. Verba, V. Tiberkevich, K. Guslienko, G. Melkov, and A. Slavin. Theory of ground-state switching in an array of magnetic nanodots by application of a short external magnetic field pulse. *Physical Review B*, 87(13):134419, apr 2013.

[129] M. Beleggia, M. De Graef, Y. T. Millev, D. A. Goode, and G Rowlands. Demagnetization factors for elliptic cylinders. *Journal of Physics D: Applied Physics*, 38(18):3333–3342, sep 2005.

[130] A. Khitun, M. Bao, and K. L. Wang. Magnonic logic circuits. *Journal of Physics D: Applied Physics*, 43(26):264005, jul 2010.